

BULLETIN OF THE RESEARCH COUNCIL OF ISRAEL

Section G GEO-SCIENCES

Bull. Res. Council. of Israel. G. Geo-Sciences

Page

- 67 Design of some numerical general circulation experiments *Y. Mintz*
115 Studies on the effect of saline irrigation water on calcareous soils.
II. The behaviour of calcium carbonate *D. H. Yaalon*
123 Simulation, by dynamical model, of sand tract morphologies occurring
in Israel *M. Rim*
137 Tentative energy and water balances for the Dead Sea *J. Neumann*

LETTER TO THE EDITOR

- 164 A note on the revision of the stratigraphy of the southern Carmel
E. Kashai

BULLETIN OF THE RESEARCH COUNCIL OF ISRAEL

Section G GEO-SCIENCES

Bull. Res. Council of Israel. G. Geo-Sciences

Page

- 67 Design of some numerical general circulation experiments *Y. Mintz*
- 115 Studies on the effect of saline irrigation water on calcareous soils.
II. The behaviour of calcium carbonate *D. H. Yaalon*
- 123 Simulation, by dynamical model, of sand tract morphologies occurring
in Israel *M. Rim*
- 137 Tentative energy and water balances for the Dead Sea *J. Neumann*

LETTER TO THE EDITOR

- 164 A note on the revision of the stratigraphy of the southern Carmel
E. Kashai

**BULLETIN
OF THE RESEARCH COUNCIL
OF ISRAEL**

MIRIAM BALABAN

Editor

EDITORIAL BOARDS

**SECTION A
CHEMISTRY**

**SECTION F
MATHEMATICS AND PHYSICS**

F. D. BERGMANN
A. DVORETZKY
A. KATCHALSKY
J. NEUMANN
F. OLLENDORFF
G. RACAH
M. REINER

**SECTION B
ZOOLOGY**

**SECTION G
GEOLOGY**

S. ADLER
F. S. BODENHEIMER
M. EVENARI
N. LANDAU
L. PICARD

**SECTION C
TECHNOLOGY**

A. BANIEL
J. BRAVERMAN
A. DE LEEUW
M. LEWIN
F. OLLENDORFF
M. REINER
I. SPITZ
A. TALMI
E. GOLDBERG,
*Technion Publications Language
Editor*

**SECTION D
BOTANY**

M. EVENARI
N. FEINBRUN
H. OPPENHEIMER
T. RAYSS
I. REICHERT
M. ZOHARY

**SECTION E
EXPERIMENTAL MEDICINE**

S. ADLER
A. DE VRIES
A. FEIGENBAUM
J. GROSS
M. RACHMILEWITZ
B. ZONDEK

Orders in America should be addressed to Interscience Publishers Inc., New York, N. Y., and in England and Europe to Wm. Dawson & Sons, Ltd., Cannon House, Macklin Street, London, W. C. 2, directly or through booksellers.

Annual subscription per section (four issues): IL. 6,000 (\$ 6.00, £ 2.20) Single copy IL. 1,500 (\$ 1.50, 12s.)

Manuscripts should be addressed:
The Editor, The Weizmann
Science Press of Israel, P.O. B.
801, Jerusalem, 33 King George
Ave. Telephone 62844

NOTICE TO CONTRIBUTORS

Contributors to the *Bulletin of the Research Council of Israel* should conform to the following recommendations of the editors of this journal in preparing manuscripts for the press.

Contributions must be original and should not have been published previously. When a paper has been accepted for publication, the author(s) may not publish it elsewhere unless permission is received from the Editor of this journal.

Papers may be submitted in English and in French.

MANUSCRIPT

General

Papers should be written as concisely as possible, MSS should be typewritten on one side only and double-spaced, with side margins not less than 2.5 cm wide. Pages, including those containing illustrations, references or tables, should be numbered.

The Editor reserves the right to return a MS to the author for retyping or any alterations. Authors should retain copies of their MS.

Spelling

Spelling should be based on the Oxford Dictionary and should be consistent throughout the paper. Geographic and proper names in particular should be checked for approved forms of spelling or transliteration.

Indications

Greek letters should be indicated in a legend preceding the MS, as well as by a pencil note in the margin on first appearance in the text.

When there is any room for confusion of symbols, they should be carefully differentiated, e.g. the letter "l" and the figure "1"; "O" and "0".

Abbreviations

Titles of journals should be abbreviated according to the *World List of Scientific Periodicals*.

Abstract

Every paper must be accompanied by a brief but comprehensive abstract. Although the length of the abstract is left to the discretion of the author, 3% of the total length of the paper is suggested.

References

In Sections A and C, and in Letters to the Editor in all Sections, references are to be cited in the text by number, e.g., ... Taylor³ ... and are to be arranged in the order of appearance.

In Sections B, D, E, and G, the references are to be cited in the text by the author's name and date of publication in parentheses, e.g., ... (Taylor 1932).... If the author's name is already mentioned in the text, then the year only appears in the parenthesis, e.g., ... found by Taylor (1932).... The references in these Sections are to be arranged in alphabetical order.

In Section F, references are to be cited in the text by number in square brackets, e.g., ... Taylor [3]... and are to be arranged in alphabetical order.

The following form should be used:

3. TAYLOR, G. I., 1932, *Proc. roy. Soc.*, A138, 41.
- Book references should be prepared according to the following form:
4. JACKSON, F., 1930, *Thermodynamics*, 4th ed., Wiley, New York

TYPOGRAPHY

In all matters of typography the form adopted in this issue should be followed. Particular attention should be given to position (of symbols, headings, etc.) and type specification.

ILLUSTRATIONS

Illustrations should be sent in a state suitable for direct photographic reproduction. Line drawings should be drawn in large scale with India ink on white drawing paper, bristol board, tracing paper, blue linen, or blue-lined graph paper. If the lettering cannot be drawn neatly by the author, he should indicate it in pencil for the guidance of the draftsman. Possible photographic reduction should be carefully considered when lettering and in other details.

Half-tone photographs should be on glossy contrast paper.

Illustrations should be mounted on separate sheets of paper on which the caption and figure number is typed. Each drawing and photograph should be identified on the back with the author's name and figure number.

The place in which the figure is to appear should be indicated in the margin of the MS.

PROOFS

Authors making revisions in proofs will be required to bear the costs thereof. Proofs should be returned to the Editor within 24 hours, otherwise no responsibility is assumed for the corrections of the author.

REPRINTS

Reprints may be ordered at the time the proof is returned. A table designating the cost of reprints may be obtained on request.

DESIGN OF SOME NUMERICAL GENERAL CIRCULATION EXPERIMENTS

YALE MINTZ^{1,2,3}

The Hebrew University of Jerusalem

ABSTRACT

The equations of motion are developed for a two-parameter model of the atmosphere with the friction and heating terms retained. An empirical surface stress coefficient is found by the diagnostic use of the equations.

A heating function is specified in which the diabatic heating of the air depends on the earth-air temperature difference. It is shown that this heating function can be used in the equations to study the mean zonal and mean meridional circulations of the atmosphere on a land-covered planet and on an ocean-covered planet in which the initial ocean temperature is a function of latitude; and to study the complete general circulation of the atmosphere on an ocean-covered planet in which the initial ocean temperature is a function of latitude and longitude and on a planet covered partly by ocean and partly by land.

INTRODUCTION

The availability of high-speed large-capacity electronic digital computers makes it possible to study the general circulation of the atmosphere by numerical integration of the equations of motion.

In the first section of this paper the equations of motion are developed for a two-parameter model of the atmosphere with the friction and heating terms retained. In this development the character of the vertical wind shear is not assumed but is derived from the given static stability of the air. In addition, the orographic effect is not prescribed in the usual way, but at each level the forced vertical motion is set equal to the product of the horizontal velocity and the slope of an orographically determined stream-surface in the direction of the velocity.

¹ On leave of absence from the University of California, Los Angeles.

² U.C.L.A. Department of Meteorology, *Contributions to Meteorology*, No. 39.

³ The research reported in this paper was sponsored in part by the Geophysics Research Directorate of the Air Force Cambridge Research Center, *Air Research and Development Command, United States Air Force*, through the European Office, ARDC.

Received August 17, 1958.

In the second section the mean surface stress coefficient is found, in an empirical way, by using the equations of motion diagnostically. Integrated over a polar cap this is the method of the zonal momentum budget, and it gives a ratio of surface stress to surface wind of $0.32 \times 10^{-4} \text{ t m}^{-2} \text{ s}^{-1}$ ($0.32 \text{ dyne cm}^{-2}$ per m s^{-1} geostrophic surface wind).

In the third section it is shown that the complex processes of heat exchange that operate in the real atmosphere can be approximated, in a crude way, by a model in which the diabatic heating of the air depends only on the earth-air temperature difference. To test whether this simple model will capture the large-scale features of the heating and cooling of the real atmosphere, it is applied to the real atmosphere and, as far as the normal heating distribution is concerned, is found to give good results. The determination of the surface temperature of land having zero heat capacity and of ocean having infinite heat capacity is described. The importance of eventually adding a term that will correspond to the release of latent heat of condensation when the air ascends is also discussed.

In the fourth section the term "general circulation" is precisely defined and four experiments are proposed, depending on the nature of the underlying surface. In the first experiment the planet is entirely land-covered. In the second it is entirely ocean-covered, with the initial ocean temperature a function only of latitude. Because of zonal symmetry of the forced heating in these two experiments, they can predict mean zonal and mean meridional circulations but not the general circulation proper. Experiments of these two types have already been performed by N. A. Phillips, and the results of the first are summarized in this section.

In the third experiment that is proposed the planet is again entirely ocean-covered, but the initial ocean temperature is a function of longitude as well as latitude. This experiment should predict a time-averaged motion which is not zonally symmetrical and hence is a complete general circulation. An experiment of this kind is being programmed by Mr. Avraham Huss for the WEIZAC Computer at the Weizmann Institute of Science, Rehovot. Finally, an experiment is proposed in which the planet is partly land- and partly ocean-covered. This experiment will be carried out by the writer on the IBM 709 Computer at the University of California, Los Angeles.

The writer wishes to thank Professors J. Charney and N. A. Phillips for the opportunity to work with their meteorology group, first at the Institute for Advanced Study in Princeton and later at the Massachusetts Institute of Technology, where he was able to discuss and develop many of the ideas presented in this paper. He also wishes to thank Mr. Avraham Huss, his assistant in the Meteorology Department of the Hebrew University, for his help in the development of these ideas.

The writer thanks Prof. P. A. Sheppard for providing him with the data for Figure 5a, and the Director of the Meteorological Office, Great Britain, for permission to use his manuscript maps of 500-mb normal temperatures, compiled by the Upper Air Climatology Branch. To Mrs. Sarah Schlesinger he is grateful for making many

of the hand computations, and to Mr. Peter Grossman for preparing the illustrations for the printer.

I. THE DYNAMICAL EQUATIONS FOR LARGE-SCALE FLOW IN A TWO-PARAMETER MODEL OF THE ATMOSPHERE

For the study of the large-scale motion of the atmosphere we will use the vorticity equation in its approximate form, and in the x, y, p, t -coordinate system,

$$\frac{\partial \zeta}{\partial t} = -\mathbf{v} \cdot \nabla (\zeta + f) + f_m \frac{\partial \omega}{\partial p} - g \frac{\partial}{\partial p} (\mathbf{k} \cdot \nabla \times \boldsymbol{\tau}), \tag{1}$$

where ζ is the vertical component of the relative vorticity, \mathbf{v} is the non-divergent component of the horizontal velocity, f is the Coriolis parameter and f_m is the mean Coriolis parameter, ω is individual pressure change (the "vertical velocity" in x, y, p -space), g is acceleration of gravity, $\boldsymbol{\tau}$ is the horizontal component of the small-scale vertical eddy stress, p is pressure, ∇ is the horizontal del operator on an isobaric surface, and \mathbf{k} is unit vertical vector.

The non-divergent component of the horizontal velocity and the vertical component of the vorticity can be written as

$$\mathbf{v} = \mathbf{k} \times \nabla \psi, \tag{2}$$

and

$$\zeta = \mathbf{k} \cdot \nabla \times \mathbf{v} = \nabla^2 \psi, \tag{3}$$

where ψ is the stream function for the non-divergent horizontal velocity and ∇^2 is the isobaric Laplacian operator.

In the experiments described in this paper, we will use the quasi-geostrophic approximation,

$$\psi = \frac{g}{f_m} Z, \tag{4}$$

where Z is height and f_m is the mean Coriolis parameter.

The two parameters which will carry the history of the motion will be the stream functions for the non-divergent horizontal velocities at the 250- and 750-mb pressure levels. For convenience, we designate quantities measured at the 0-, 250-, 500-, 750-, and 1000-mb levels by the subscripts 0, 1, 2, 3 and 4, and quantities measured at the surface of the earth by the subscript s , as shown in Figure 1.

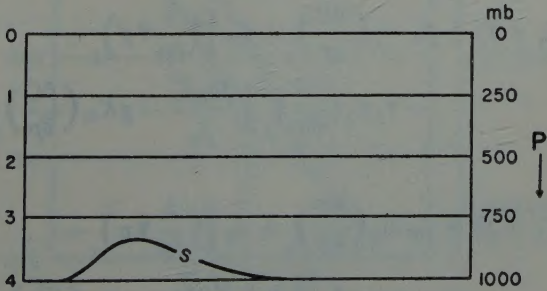


Figure 1
Pressure surfaces designated by the subscripts 0, 1, 2, 3, 4 and s .

With this notation we then have, from (1),

$$\frac{\partial \xi_1}{\partial t} = -\mathbf{v}_1 \cdot \nabla (\xi_1 + f) + f_m \left(\frac{\partial \omega}{\partial p} \right)_1 - g \left[\frac{\partial}{\partial p} (\mathbf{k} \cdot \nabla \times \boldsymbol{\tau}) \right]_1 \quad (5)$$

and

$$\frac{\partial \xi_3}{\partial t} = -\mathbf{v}_3 \cdot \nabla (\xi_3 + f) + f_m \left(\frac{\partial \omega}{\partial p} \right)_3 - g \left[\frac{\partial}{\partial p} (\mathbf{k} \cdot \nabla \times \boldsymbol{\tau}) \right]_3. \quad (6)$$

Given ψ_1 and ψ_3 (and hence $\mathbf{v}_1, \mathbf{v}_3, \xi_1$ and ξ_3) at any time t , and the boundary conditions, there are six unknowns in equations (5) and (6): $\partial\psi_1/\partial t$, $\partial\psi_3/\partial t$, $(\partial\omega/\partial p)_1$, $(\partial\omega/\partial p)_3$, $(\partial\boldsymbol{\tau}/\partial p)_1$ and $(\partial\boldsymbol{\tau}/\partial p)_3$.

We replace the last four of these unknowns with more tractable parameters by the approximations:

$$\omega = \omega_2 B(p) + \left[\mathbf{v} \frac{p}{\bar{p}_s} - \mathbf{v}_2 \frac{p_2}{\bar{p}_s} B(p) \right] \cdot \nabla_H \bar{p}_s. \quad (7)$$

where, given ω_2 , the first term on the right describes the distribution of ω with p that would occur if the ground beneath were level, and the second term gives the deviation from $\omega_2 B(p)$ due to the orographically forced vertical motion, $\mathbf{v} \cdot (p/\bar{p} \nabla_s)_{H\bar{p}_s} \cdot (p/\bar{p}_s) \nabla_H \bar{p}_s$ is the slope, in x, y, p -space, of an orographically determined stream surface which varies from $\nabla_H \bar{p}_s$ at the ground to zero at the top of the atmosphere. $B(p)$ is an arbitrary or empirically determined function of pressure, and $\nabla_H \bar{p}_s$ is the horizontal gradient of the time-averaged surface pressure;

$$\boldsymbol{\tau} = C(p) \boldsymbol{\tau}_s, \quad (8)$$

where $C(p)$ is an arbitrary or empirically determined function of pressure, and $\boldsymbol{\tau}_s$ is the surface stress

$$\boldsymbol{\tau}_s = K \mathbf{v}_s, \quad (9)$$

where K is the surface stress coefficient and \mathbf{v}_s is the geostrophic surface wind; and

$$K = K_m S(\gamma_{3-4}), \quad (10)$$

where K_m is the mean surface stress coefficient, and $S(\gamma_{3-4})$ is an arbitrary or empirically determined function of the static stability of the lowest layer of air.

Substituting from (7), (8), (9) and (10) into equations (5) and (6), we obtain

$$\begin{aligned} \frac{\partial \xi_1}{\partial t} = & -\mathbf{v}_1 \cdot \nabla (\xi_1 + f) + f_m \omega_2 \left(\frac{\partial B}{\partial p} \right)_1 + f_m \left[\left(\frac{\partial}{\partial p} \mathbf{v} p \right)_1 - \right. \\ & \left. - \mathbf{v}_2 p_2 \left(\frac{\partial B}{\partial p} \right)_1 \right] \cdot \frac{\nabla_H \bar{p}_s}{\bar{p}_s} - g K_m \left(\frac{\partial C}{\partial p} \right)_1 \mathbf{k} \cdot \nabla \times S \mathbf{v}_s, \quad (11) \end{aligned}$$

and

$$\begin{aligned} \frac{\partial \xi_3}{\partial t} = & -\mathbf{v}_3 \cdot \nabla (\xi_3 + f) + f_m \omega_2 \left(\frac{\partial B}{\partial p} \right)_3 + f_m \left[\left(\frac{\partial}{\partial p} \mathbf{v} p \right)_3 - \right. \\ & \left. - \mathbf{v}_2 p_2 \left(\frac{\partial B}{\partial p} \right)_3 \right] \cdot \frac{\nabla_H \bar{p}_s}{\bar{p}_s} - g K_m \left(\frac{\partial C}{\partial p} \right)_3 \mathbf{k} \cdot \nabla \times S \mathbf{v}_s. \quad (12) \end{aligned}$$

Given ψ_1 and ψ_3 , (11) and (12) are now two dynamical equations in the six unknowns: $\partial\psi_1/\partial t$, $\partial\psi_3/\partial t$, ω_2 , \mathbf{v}_2 , \mathbf{v}_s and S .

We now make use of the thermodynamic energy equation, in the form

$$\frac{\partial}{\partial t} \left(\frac{\partial z}{\partial p} \right) = - \mathbf{v} \cdot \nabla \frac{\partial z}{\partial p} + \Gamma \omega - \frac{R}{gc_p} \frac{h}{p}, \quad (13)$$

where

$$\Gamma = \frac{RT}{gp\Theta} = \frac{R}{g} \frac{p^{\kappa-1}}{p_4^{\kappa}} \frac{\partial \Theta}{\partial p}, \quad (14)$$

and h is the heat added to unit mass of air in unit time, T is temperature, Θ is potential temperature, R is the gas constant, c_p is specific heat at constant pressure, and $\kappa = R/c_p$ is Poisson's constant.

Taking the integral of (13) from p_1 to p_3 , with substitutions from (4), (7) and (14), we obtain

$$\begin{aligned} \frac{\partial}{\partial t} (\psi_3 - \psi_1) = & - \int_{p_1}^{p_3} \mathbf{v} \cdot \nabla \left(\frac{\partial \psi}{\partial p} \right) \delta p - \frac{R}{f_m c_p} \int_{p_1}^{p_3} \frac{h}{p} \delta p + \\ & + \frac{R}{f_m p_4^{\kappa}} \int_{p_1}^{p_3} \left\{ \omega_2 B(p) + [\mathbf{v} p - \mathbf{v}_2 p_2 B(p)] \cdot \frac{\nabla_H \bar{p}_s}{\bar{p}_s} \right\} \frac{\partial \Theta}{\partial p} p^{\kappa-1} \delta p. \end{aligned} \quad (15)$$

We now introduce the approximations:

$$h = F(p) Q, \quad (16)$$

where $Q(x, y, t)$ is the heat added to unit column of air in unit time, and $F(p)$ is an arbitrary or empirically determined function of pressure; and

$$-\frac{\partial \Theta}{\partial p} = \gamma(p), \quad \text{for } p_1 < p < p_3, \quad (17)$$

which states that *between the levels p_1 and p_3 the lapse rate of potential temperature, γ , is a function only of pressure*, as shown in Figure 2.

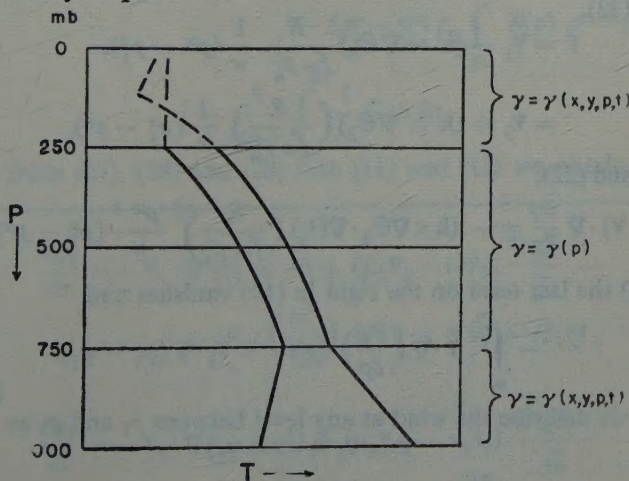


Figure 2
The distribution of γ .

The approximations (16) and (17) enable us to integrate all three terms on the right in equation (15).

We integrate the first term on the right in (15) by describing the wind at any level between p_1 and p_3 as

$$\mathbf{v} = \mathbf{v}_3 + (\mathbf{v} - \mathbf{v}_3), \quad (18)$$

so that

$$-\int_{p_1}^{p_3} \mathbf{v} \cdot \nabla \left(\frac{\partial \psi}{\partial p} \right) \delta p = -\mathbf{v}_3 \cdot \nabla (\psi_3 - \psi_1) + \int_{p_1}^{p_3} (\mathbf{v}_3 - \mathbf{v}) \cdot \nabla \left(\frac{\partial \psi}{\partial p} \right) \delta p. \quad (19)$$

Because ∇ is an isobaric operator,

$$\nabla \frac{\partial \psi}{\partial p} = \frac{g}{f_m} \nabla \frac{\partial z}{\partial p} = -\frac{1}{f_m} \nabla \alpha = -\frac{R}{f_m p} \nabla T = -\frac{R}{f_m} \frac{p^{\kappa-1}}{p_4^{\kappa}} \nabla \Theta. \quad (20)$$

Using (17),

$$\Theta = \Theta_3 + \int_p^{p_3} \gamma(p) \delta p,$$

or

$$\nabla \Theta = \nabla \Theta_3, \quad \text{for } p_1 < p < p_3, \quad (21)$$

and substituting into (20),

$$\nabla \frac{\partial \psi}{\partial p} = -\frac{R}{f_m} \frac{p^{\kappa-1}}{p_4^{\kappa}} \nabla \Theta_3, \quad \text{for } p_1 < p < p_3. \quad (22)$$

For the vertical shear of the wind we then have, from (2) and (22),

$$\frac{\partial \mathbf{v}}{\partial p} = \mathbf{k} \times \nabla \frac{\partial \psi}{\partial p} = -\frac{R}{f_m} \frac{p^{\kappa-1}}{p_4^{\kappa}} \mathbf{k} \times \nabla \Theta_3, \quad \text{for } p_1 < p < p_3. \quad (23)$$

In other words, the assumption that $\gamma = \gamma(p)$ between p_1 and p_3 necessarily implies that between these two levels the wind shear, $\partial \mathbf{v} / \partial p$, is constant in direction and that its magnitude is proportional to $p^{\kappa-1}$.

Integrating (23),

$$\begin{aligned} \mathbf{v} &= \mathbf{v}_1 - (\mathbf{k} \times \nabla \Theta_3) \frac{R}{f_m p_4^{\kappa}} \frac{1}{\kappa} (p^{\kappa} - p_1^{\kappa}), \\ &= \mathbf{v}_3 + (\mathbf{k} \times \nabla \Theta_3) \left(\frac{R}{f_m p_4^{\kappa}} \right) \frac{1}{\kappa} (p_3^{\kappa} - p^{\kappa}), \end{aligned} \quad (24)$$

and from (24) and (22),

$$(\mathbf{v}_3 - \mathbf{v}) \cdot \nabla \frac{\partial \psi}{\partial p} = -(\mathbf{k} \times \nabla \Theta_3 \cdot \nabla \Theta_3) \left(\frac{R}{f_m p_4^{\kappa}} \right)^2 \frac{p^{\kappa-1}}{\kappa} (p_3^{\kappa} - p^{\kappa}) = 0. \quad (25)$$

When $\gamma = \gamma(p)$ the last term on the right in (19) vanishes and

$$-\int_{p_1}^{p_3} \mathbf{v} \cdot \nabla \left(\frac{\partial \psi}{\partial p} \right) \delta p = -\mathbf{v}_3 \cdot \nabla (\psi_3 - \psi_1). \quad (26)$$

Similarly, if we describe the wind at any level between p_1 and p_3 as

$$\mathbf{v} = \mathbf{v}_1 + (\mathbf{v} - \mathbf{v}_1) \quad (18a)$$

we obtain

$$-\int_{p_1}^{p_3} \mathbf{v} \cdot \nabla \left(\frac{\partial \psi}{\partial p} \right) \delta p = -\mathbf{v}_1 \cdot \nabla (\psi_3 - \psi_1). \quad (26a)$$

From (24) we also obtain

$$\begin{aligned} \mathbf{v} &= \mathbf{v}_1 + (\mathbf{v}_1 - \mathbf{v}_3) \frac{p_1^* - p^*}{p_3^* - p_1^*}, \\ &= \mathbf{v}_3 + (\mathbf{v}_1 - \mathbf{v}_3) \frac{p_3^* - p^*}{p_3^* - p_1^*}, \end{aligned} \quad (27)$$

and

$$\begin{aligned} \mathbf{v}_2 &= \mathbf{v}_1 + (\mathbf{v}_1 - \mathbf{v}_3) \frac{p_1^* - p_2^*}{p_3^* - p_1^*} \\ &= \mathbf{v}_3 + (\mathbf{v}_1 - \mathbf{v}_3) \frac{p_3^* - p_2^*}{p_3^* - p_1^*}. \end{aligned} \quad (28)$$

Substituting now from (26), (27), (28), (17) and (16) into equation (15), we obtain

$$\frac{\partial}{\partial t}(\psi_1 - \psi_3) = -\mathbf{v}_{1,3} \cdot \nabla(\psi_1 - \psi_3) + G\omega_2 + IQ + (H_1\mathbf{v}_1 - H_3\mathbf{v}_3) \cdot \frac{\nabla_H \bar{p}_s}{\bar{p}_s}, \quad (29)$$

where $\mathbf{v}_{1,3}$ denotes either \mathbf{v}_1 or \mathbf{v}_3 , and

$$G = \frac{R}{f_m p_4^*} \int_{p_1}^{p_3} B(p) \gamma(p) p^{*x-1} \delta p, \quad (30)$$

$$\begin{aligned} H_1 &= \frac{R}{f_m p_4^*} \frac{1}{p_3^* - p_1^*} \left[\int_{p_1}^{p_3} (p_3^* - p^*) p^{*x} \gamma(p) \delta p - \right. \\ &\quad \left. - (p_3^* - p_2^*) p_2 \int_{p_1}^{p_3} B(p) p^{*x-1} \gamma(p) \delta p \right], \end{aligned} \quad (31)$$

$$\begin{aligned} H_3 &= \frac{R}{f_m p_4^*} \frac{1}{p_3^* - p_1^*} \left[\int_{p_1}^{p_3} (p_1^* - p^*) p^{*x} \gamma(p) \delta p - \right. \\ &\quad \left. - (p_1^* - p_2^*) p_2 \int_{p_1}^{p_3} B(p) p^{*x-1} \gamma(p) \delta p \right], \end{aligned} \quad (32)$$

and

$$I = \frac{R}{f_m c_p} \int_{p_1}^{p_3} \frac{1}{p} F(p) \delta p. \quad (33)$$

Substituting from (27), (28) and (29) into (11) and (12) we obtain, finally,

$$\begin{aligned} \frac{\partial q_1}{\partial t} &= -\mathbf{v}_1 \cdot \nabla(q_1 + f) + (\mu_1 \mathbf{v}_1 - \nu_1 \mathbf{v}_3) \cdot \frac{\nabla_H \bar{p}}{\bar{p}_s} - \\ &\quad - gK_m \left(\frac{\partial C}{\partial p} \right)_1 \mathbf{k} \cdot \nabla \times S \mathbf{v}_s + I \lambda_1 Q, \end{aligned} \quad (34)$$

and

$$\begin{aligned} \frac{\partial q_3}{\partial t} &= -\mathbf{v}_3 \cdot \nabla(q_3 + f) + (\mu_3 \mathbf{v}_1 - \nu_3 \mathbf{v}_3) \cdot \frac{\nabla_H \bar{p}_s}{\bar{p}_s} - \\ &\quad - gK_m \left(\frac{\partial C}{\partial p} \right)_3 \mathbf{k} \cdot \nabla \times S \mathbf{v}_s + I \lambda_3 Q, \end{aligned} \quad (35)$$

where

$$q_1 = \zeta_1 + \lambda_1(\psi_1 - \psi_3), \quad (36)$$

$$q_3 = \zeta_3 + \lambda_3(\psi_1 - \psi_3); \quad (37)$$

$$\lambda_1 = -\frac{f_m}{G} \left(\frac{\partial B}{\partial p} \right)_1, \quad (38)$$

$$\lambda_3 = -\frac{f_m}{G} \left(\frac{\partial B}{\partial p} \right)_3; \quad (39)$$

$$\mu_1 = \lambda_1 H_1 + \frac{f_m}{p_3^\kappa - p_1^\kappa} \left[p_3^\kappa - p_1^\kappa (1 + \kappa) - p_2 \left(\frac{\partial B}{\partial p} \right)_1 (p_3^\kappa - p_2^\kappa) \right], \quad (40)$$

$$\mu_3 = \lambda_3 H_1 - \frac{f_m}{p_3^\kappa - p_1^\kappa} \left[\kappa p_3^\kappa + p_2 \left(\frac{\partial B}{\partial p} \right)_3 (p_3^\kappa - p_2^\kappa) \right]; \quad (41)$$

and

$$\nu_1 = \lambda_1 H_3 - \frac{f_m}{p_3^\kappa - p_1^\kappa} \left[\kappa p_1^\kappa - p_2 \left(\frac{\partial B}{\partial p} \right)_1 (p_2^\kappa - p_1^\kappa) \right], \quad (42)$$

$$\nu_3 = \lambda_3 H_3 + \frac{f_m}{p_3^\kappa - p_1^\kappa} \left[p_1^\kappa - p_3^\kappa (1 + \kappa) + p_2 \left(\frac{\partial B}{\partial p} \right)_3 (p_2^\kappa - p_1^\kappa) \right]. \quad (43)$$

We note, in passing, that if we had adiabatic frictionless flow over level ground, or

$$Q \equiv 0, \quad K \equiv 0 \quad \text{and} \quad \nabla_H \bar{p}_s \equiv 0,$$

then (34) and (35) would reduce to the simple forms

$$\frac{\partial q_1}{\partial t} = -\mathbf{v}_1 \cdot \nabla (q_1 + f),$$

and

$$\frac{\partial q_3}{\partial t} = -\mathbf{v}_3 \cdot \nabla (q_3 + f).$$

For the surface wind, \mathbf{v}_s , we write

$$\mathbf{v}_s = \mathbf{v}_3 + \int_{p_3}^{\bar{p}_s} \frac{\partial \mathbf{v}}{\partial p} \delta p,$$

and from (2) and (20)

$$\mathbf{v}_s = \mathbf{v}_3 - \frac{R}{f_m p_4^\kappa} \int_{p_3}^{\bar{p}_s} (\mathbf{k} \times \nabla \Theta) p^{\kappa-1} \delta p. \quad (44)$$

Using the approximations:

$$\frac{\partial \Theta}{\partial p} = \frac{\Theta_4 - \Theta_3}{p_4 - p_3}, \quad \text{for } p_3 < p < \bar{p}_s, \quad (45)$$

and

$$\Theta_4 \equiv T_4 = T_g, \quad (46)$$

where T_g is the temperature of the ground reduced to 1000-mb; and substituting for $\nabla \Theta_3$ from the integral of (22), which is

$$\nabla(\psi_1 - \psi_3) = \frac{R}{f_m p_4^\kappa} \nabla\Theta_3 \int_{p_1}^{p_3} p^{\kappa-1} \delta p, \quad (47)$$

we get

$$\nabla\Theta = \frac{\kappa f_m p_4^\kappa}{R(p_3^\kappa - p_1^\kappa)} \left(1 - \frac{p - p_3}{p_4 - p_3}\right) \nabla(\psi_1 - \psi_3) + \frac{p - p_3}{p_4 - p_3} \nabla T_g, \quad (48)$$

for $p_3 < p < \bar{p}_s$.

Substituting from (48) into (44), we obtain

$$\mathbf{v}_s = \mathbf{v}_3 - L(\bar{p}_s) (\mathbf{v}_1 - \mathbf{v}_3) - M(\bar{p}_s) \mathbf{k} \times \nabla T_g \quad (49)$$

where

$$L(\bar{p}_s) = \frac{\kappa}{p_3^\kappa - p_1^\kappa} \int_{p_3}^{\bar{p}_s} \left(1 - \frac{p - p_3}{p_4 - p_3}\right) p^{\kappa-1} \delta p, \quad (50)$$

and

$$M(\bar{p}_s) = \frac{R}{f_m p_4^\kappa (p_4 - p_3)} \int_{p_3}^{\bar{p}_s} (p - p_3) p^{\kappa-1} \delta p. \quad (51)$$

An example of the vertical variation of the wind from p_1 to p_s , in this model, is shown in Figure 3. For a simple illustration we show only the westerly component of the flow, for

$$u_1 = 35 \text{ m s}^{-1}, \quad u_3 = 15 \text{ m s}^{-1}, \quad \bar{p}_s = p_4, \quad \kappa = 0.286$$

and the three cases,

$$\nabla T_g = 0, \quad \text{which gives } u_s = 11.7 \text{ m s}^{-1},$$

$$\nabla T_g = \nabla\Theta_3, \quad \text{which gives } u_s = 8.6 \text{ m s}^{-1},$$

$$\nabla T_g = 2\nabla\Theta_3, \quad \text{which gives } u_s = 5.6 \text{ m s}^{-1}.$$

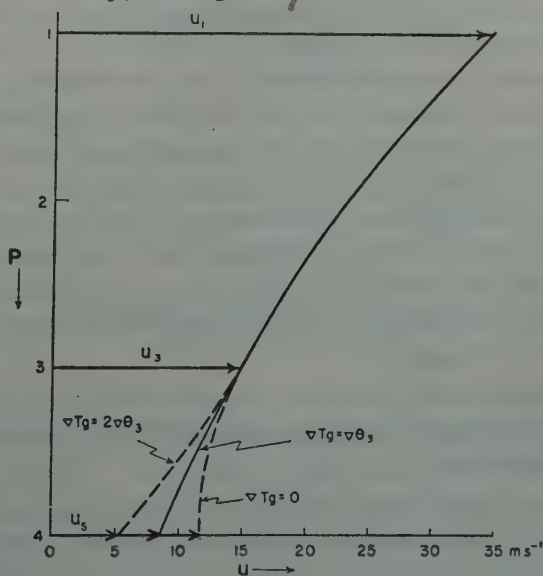


Figure 3

Dependence of the surface wind upon the horizontal surface temperature gradient.

The example shows that there can be large differences in the surface wind depending upon whether the horizontal temperature gradient at the surface is smaller, the same, or larger than the horizontal temperature gradient in the layer from p_1 to p_3 .

For the function $B(p)$, which determines how the vertical velocity will vary with height over level ground, we will use

$$B = 4 \frac{p_4 p - p^2}{p_1^2} . \quad (52)$$

That this parabolic distribution of the vertical velocity is a fair approximation to the normal distribution of ω in the real atmosphere is indicated by those studies in which the vertical velocity is computed from the horizontal divergence of the observed wind.

One such study, by Palmén (1958), is shown in Figure 4. To reduce the effect of instrumental errors in the wind observations and the effect of local deviations of the wind due to eddies of a scale smaller than the distances between observing stations, Palmén averaged the divergence of the observed wind over two large areas: a western area (W) in which the winds in the lower levels were northerly, and an eastern area (E) in which the winds were southerly. These two areas and the streamlines of the wind at the 700-mb level are shown in Figure 4a. The vertical velocity ω , computed from the average divergence of the observed wind in each of the two areas, is shown in Figure 4b. The function $B = \omega/\omega_2$, averaged for the two curves, is shown in Figure 4c.

Another study of this kind is that of Sheppard (1949), who measured the divergence of the observed wind over the triangular area between three radar wind stations. To reduce the effect of instrumental errors in the wind observations and the effect of eddies smaller than the distances between the observing stations, Sheppard formed the time-average of the divergence of the observed wind over monthly periods, averaging the cases separately according to the sign of the vertical velocity at 500-mb. The results for the triangular area (Liverpool-Larkhill-Downham Market) for the period 1 Dec. 1947–31 Jan. 1948 (derived from figure 3 in Sheppard's paper and the number of cases used for each curve, supplied by Prof. Sheppard in a personal communication) are given in Figure 5a. The function $B = \omega/\omega_2$, averaged for the two curves, is shown in Figure 5b.

Both of these studies, which are the only ones of their kind known to the writer, indicate that (52) represents, roughly, the average vertical variation of ω over level ground in the real atmosphere.*

The orographically forced vertical motion, in our model, at each level is equal to the scalar product of the horizontal velocity and the slope of an orographically

* For the longitude-averaged vertical velocity, kinematically computed from the observed winds in the latitude belt 15°–30°N, cf. Vuorela (1955), figs. 9, 10.

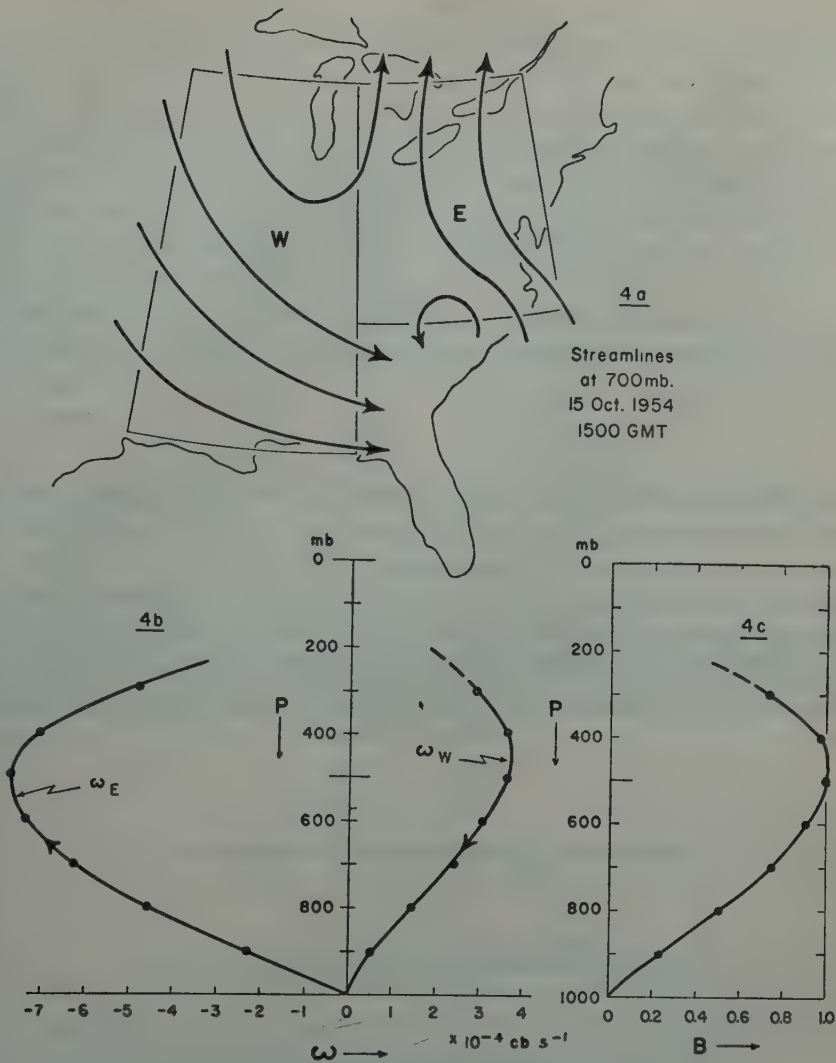


Figure 4

The kinematically computed vertical velocity, and the function $B(p)$, in a synoptic example (from Palmén, 1958).

determined stream surface, $(p/\bar{p}_s)\nabla_H\bar{p}_s$ as shown in Figure 6. The linear variation of this slope, from $\nabla_H\bar{p}_s$ at the ground to zero at the top of the atmosphere, was arbitrarily chosen.

It should be noted that this orographically forced vertical motion differs in an important way from the manner in which orography is usually introduced into numerical forecasting models. In the usual procedure (cf. Estoque, 1957; Haltiner,

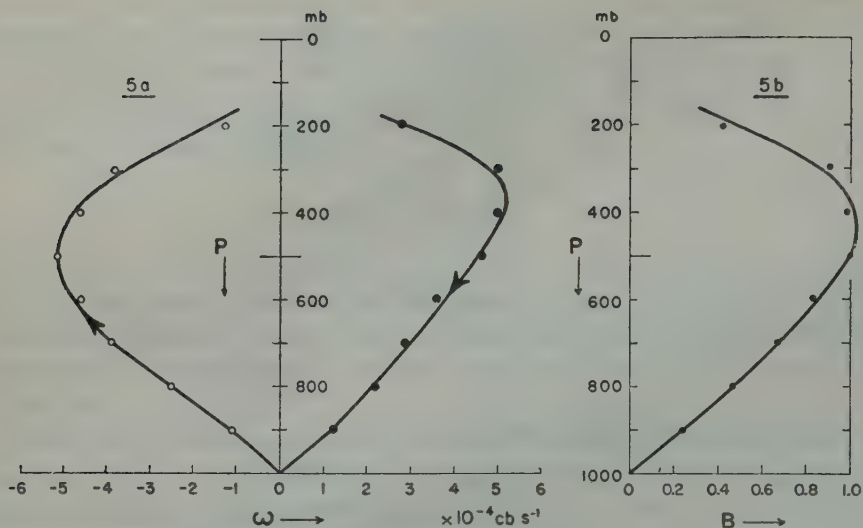


Figure 5

The kinematically computed vertical velocity in the triangular area Liverpool-Larkhill-Downham Market during the period 1 Dec. 1947 to 31 Jan. 1948, averaged according to the sign of the vertical velocity at 500-mb; and the corresponding function $B(p)$. The open circles show the average vertical velocity for all the cases in which the air at 500-mb was ascending ($\omega_{500} < 0$), the closed circles the average for all the cases in which the air at 500-mb was descending ($\omega_{500} > 0$) (data from Sheppard, 1949).

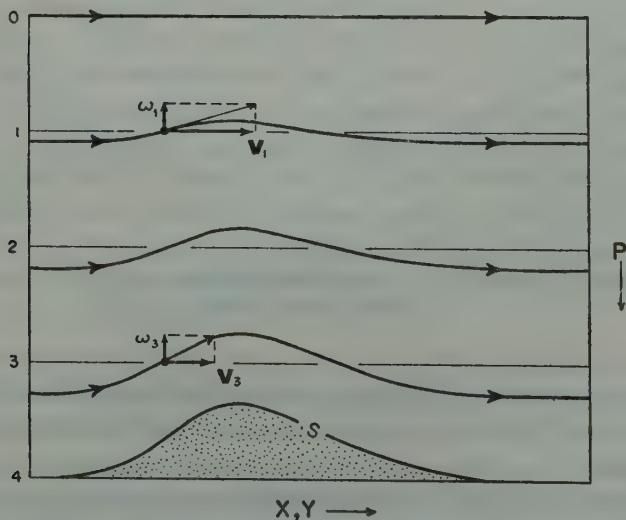


Figure 6

The orographically determined stream-surfaces and forced vertical velocities at the levels 1 and 3.

G. J. and Hesse, T. S., 1958) the orographic vertical motion at all levels depends only upon the slope of the ground and the horizontal velocity *at the ground*. In our model it depends not only upon the wind at the ground but also upon the *vertical wind shear*. For example, to use an extreme case, if the wind changes from an upslope to a downslope direction between the lower and upper levels, the vertical velocity will change from *ascent* at the lower levels to *descent* at the upper levels. This orographic component of the vertical velocity is almost exactly the same as that which obtains in the x, y, σ -coordinate system of Phillips (1957), but it enables us to keep the other advantages of the x, y, p -system.

For the lapse rate of potential temperature in the levels between p_1 and p_3 we will use the values of γ given by the International Standard Atmosphere, in which, for $p > 225$ -mb,

$$\gamma = -\frac{\partial \Theta}{\partial p} = 42.5 \times p^{-1.095}. \quad (53)$$

Our assumption, that $\gamma = \gamma(p)$ for $p_1 < p < p_3$, is a fair approximation to conditions in the real atmosphere. Except in the narrow frontal zones, which are only about 100-mb deep, the lapse rate at these levels in the real atmosphere is in fact remarkably constant.

As we have seen, the condition that γ is constant in x and y signifies that between p_1 and p_3 the wind shear, $\partial \mathbf{v} / \partial p$, does not change direction with height and that its magnitude is proportional to $p^{\kappa-1}$. This means that the vertical wind shear, *in x, y, z -space*, is

$$\frac{\partial \mathbf{v}}{\partial z} = -\varrho g \frac{\partial \mathbf{v}}{\partial p},$$

or

$$\frac{\partial \mathbf{v}}{\partial z} \propto \varrho p^{\kappa-1} = \frac{p^{\kappa}}{RT} = \frac{p_4^{\kappa}}{R\Theta},$$

and

$$\frac{\partial \mathbf{v}}{\partial z} \propto \frac{1}{\Theta}, \quad (54)$$

where ϱ is the density. Because the percentage variation of Θ is small between p_1 and p_3 , $\partial \mathbf{v} / \partial z$ is nearly constant with height between p_1 and p_3 , in the model.

Near the ground, in the real atmosphere, γ varies markedly in x, y and t . And in the model, γ varies in x, y and t according to (45) and (46), where both Θ_3 and T_0 are functions of x, y, t .

In the real atmosphere γ also varies markedly with x, y and t in the high troposphere and in the stratosphere. But γ for $p < p_1$ does not enter into the prediction equations for our model, and therefore need not be specified.

For the function $C(p)$, which specifies how the vertical eddy stress varies with height, we will assume

$$C = \frac{p^2}{p_s^2}, \quad (55)$$

or

$$\frac{\partial C}{\partial p} = \frac{2}{\bar{p}^2} p. \quad (56)$$

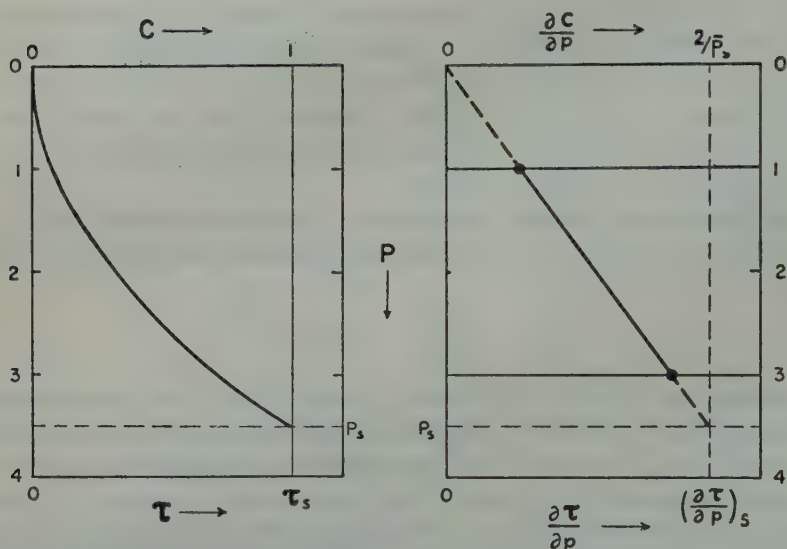


Figure 7

Vertical variations of the frictional stress, τ , and of the frictional force, $\partial\tau/\partial p$.

The resulting parabolic variation of the frictional stress, τ , and linear variation of the frictional force, $\partial\tau/\partial p$, is of course an extremely crude approximation.

The usual assumption made about the vertical eddy stress is that

$$\tau = \mu \frac{\partial v}{\partial z}, \quad (57)$$

where μ is the eddy viscosity.

But in our model, as we have seen, $\partial v/\partial z$ is nearly constant with height between p_1 and p_3 , so that if μ is taken as constant,

$$\frac{\partial\tau}{\partial p} = \mu \frac{\partial}{\partial p} \left(\frac{\partial v}{\partial z} \right) \approx 0.$$

Equation (57) is therefore not a suitable way of estimating the frictional stress when we have only a two-parameter representation of the atmosphere, and we must resort to some approximation such as (8).

For the function $S(\gamma_{3-4})$, which specifies how the surface frictional force will vary with the stability of the air in the lowest layer, we will assume

$$S = \begin{cases} 1.82 & \text{for } \gamma_{3-4} \leq 0 \\ 1.82 - 1.64 \gamma_{3-4} & \text{for } 0 < \gamma_{3-4} < \gamma_T \\ 0.182 & \text{for } \gamma_{3-4} \geq \gamma_T \end{cases} \quad (58)$$

where γ_T is the lapse rate of potential temperature for an isothermal atmosphere and $\gamma = 0$ is the adiabatic lapse rate. Making the surface stress coefficient vary with the stability in this way through a whole order of magnitude is not entirely arbitrary, but is guided by two observed phenomena: (1) for a given geostrophic surface wind, the ratio of the anemometer-measured surface wind to the geostrophic wind is about two to three times larger under unstable than under stable conditions (cf. Barad and Davidson, 1954); and (2) for a given anemometer-measured surface wind, the ratio of the surface stress to the anemometer-measured wind is about twice as large under unstable as under stable conditions (cf. Darbyshire and Darbyshire, 1955). Together with the usual assumption that the surface stress varies with the square of the anemometer-measured wind, these two observed conditions justify, in a rough way, the assumption that the ratio of *surface stress* to *geostrophic wind* is highly dependent upon the stability of the air.

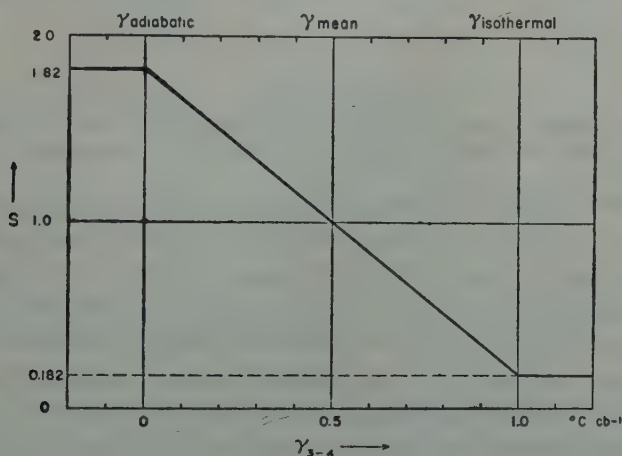


Figure 8

Dependence of the surface stress on the static stability of the air.

The dependence of the surface stress upon the stability of the air may be an important factor in the vorticity budget of the atmosphere. If we write

$$-\mathbf{k} \cdot \nabla \times K \mathbf{v}_s = -\mathbf{k} \cdot \nabla K \times \mathbf{v}_s - K \mathbf{k} \cdot \nabla \times \mathbf{v}_s, \quad (59)$$

the last term always acts to decrease the absolute magnitude of the surface vorticity. But the first term on the right in (59) may increase or decrease the vorticity. For example, off the east coasts of the continents, in winter, a stream of cold air from the land may run parallel to warmer air coming from lower latitudes, as shown in Figure 9. As these air currents of different temperature pass over an ocean surface which has a smaller horizontal gradient of temperature, there will be a gradient of γ_{3-4} in the direction normal to the wind and, according to the first term on the right in (59), cyclonic vorticity will be frictionally generated in the air. A simple calculation,

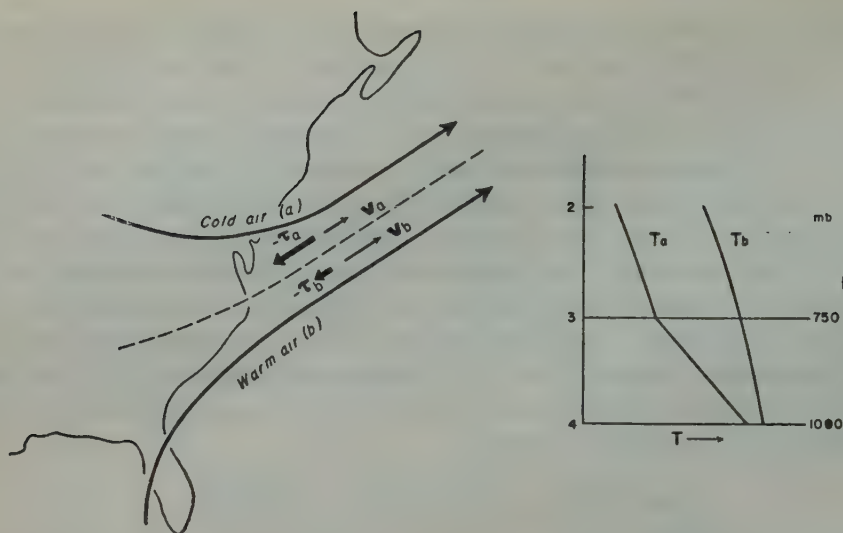


Figure 9

Example of the variation of the surface stress with the static stability over the western oceans.

— τ is the stress of the ground upon the air, in this case producing cyclonic vorticity.

using a moderate value of the surface geostrophic wind and a moderate gradient of γ_{3-4} , shows that the rate of increase of the vorticity of the air by this means will be of the same order of magnitude as the observed advective changes of vorticity. Moreover, with the function $C(p)$ as given, the largest part of the increase of vorticity will be in the air near the ground. We will study the possible contribution of this term to a high frequency of east coast cyclogenesis, in the numerical experiments, by comparing the development of the circulation when K is allowed to vary with the stability, as above, with the development when K is kept constant, all other conditions of the experiment being kept the same.

A word should be said justifying the use of a linear variation between surface stress and surface geostrophic wind and about the neglect of the variation of surface roughness in our model. The linear relationship is used, as a first approximation, because observations in the real atmosphere show that the ratio of the anemometer-measured surface wind to the geostrophic wind decreases as the geostrophic speed increases (*cf.* Gordon, 1950; Barad and Davidson, 1954). Therefore, if the stress varies with the anemometer measured wind raised to the second power, it will vary with the geostrophic wind raised to a power smaller than two. We are arbitrarily making this power unity.

There are also indications (*cf.* Barad and Davidson, 1954) that, at least over the smaller scales of roughness, the ratio of the anemometer-measured surface wind to the geostrophic wind decreases as the surface roughness increases. This acts to reduce the dependence of the stress upon the roughness when the wind used is the geostrophic.

The magnitude of the average surface stress coefficient, K_m , will be derived in Section II.

For the function $F(p)$, which determines how the diabatic heating is distributed with height, we will assume that it is constant, or

$$F = \frac{g}{p_4} = 9.81 \times 10^{-2} \text{ m}^2 \text{ t}^{-1}, \quad (60)$$

so that one-half of the total heating of unit column of air takes place in that part of the column which lies between p_1 and p_3 .

Given $B(p)$, $\gamma(p)$ and $F(p)$, in (52), (53) and (60), and $R = 287 \text{ kJ t}^{-1} \text{ deg}^{-1}$, $c_p = 1004 \text{ kJ t}^{-1} \text{ deg}^{-1}$, $\kappa = 0.286$, $f_m = 10^{-4} \text{ s}^{-1}$ and $g = 9.81 \text{ m s}^{-2}$, we obtain the following numerical values for the constants:

$$\begin{aligned} G &= 1.596 \times 10^6 \text{ m}^3 \text{ s t}^{-1} \\ H_1 &= 5.72 \times 10^6 \text{ m}^2 \text{ s}^{-1} \\ H_3 &= 11.10 \times 10^6 \text{ m}^2 \text{ s}^{-1} \\ I &= 3.08 \times 10^2 \text{ m}^2 \text{ s t}^{-1} \\ \lambda_1 &= -1.261 \times 10^{-12} \text{ m}^{-2} \\ \lambda_3 &= 1.261 \times 10^{-12} \text{ m}^{-2} \\ \mu_1 &= -2.53 \times 10^{-5} \text{ s}^{-1} \\ \mu_3 &= -5.82 \times 10^{-5} \text{ s}^{-1} \\ \nu_1 &= -3.20 \times 10^{-5} \text{ s}^{-1} \\ \nu_3 &= -2.51 \times 10^{-4} \text{ s}^{-1} \end{aligned}$$

For the special case of level ground, or $\bar{p}_s \equiv p_4$, we also have

$$L = 1.66 \times 10^{-1}$$

and
$$M = 3.82 \times 10^5 \text{ m}^2 \text{ s}^{-1} \text{ deg}^{-1}.$$

The heating function, $Q(x, y, t)$, and the expression for the surface temperature, $T_g(x, y, t)$, are described in Section III.

II. EMPIRICAL DETERMINATION OF THE MEAN SURFACE STRESS COEFFICIENT, K_m

Equations (9) and (10) can be used to obtain the mean surface stress coefficient, K_m , if we know the surface geostrophic wind and at the same time we compute, independently, the curl of the surface stress, $\nabla \times \bar{\tau}_s$, where the superior bar operator denotes the mean taken with respect to time.

$\nabla \times \bar{\tau}_s$ can be computed by using the vorticity equation (1) diagnostically. This is done by taking the time-mean and vertical integral of (1) to obtain

$$0 = - \int_0^{p_s} \bar{\mathbf{v}} \cdot \nabla (\bar{\zeta} + f) \delta p + f_m \bar{\omega}_s - g \mathbf{k} \cdot \nabla \times \bar{\tau}_s. \quad (61)$$

The time interval must be chosen sufficiently long to make the mean local time rate of change of vorticity negligibly small.

Substituting for

$$\omega_s \approx -g \varrho_s w_s = -g \varrho_s \mathbf{V}_s \cdot \nabla_H H_s, \quad (62)$$

where $\nabla_H H_s$ is the slope of the ground in x, y, z -space, we get

$$g \mathbf{k} \cdot \nabla \times \overline{\boldsymbol{\tau}}_s = - \int_0^{p_s} \overline{\mathbf{v} \cdot \nabla (\zeta + f)} \delta p - g f_m \overline{\varrho_s \mathbf{V}_s} \cdot \nabla_H H_s. \quad (63)$$

From the observed field of $\mathbf{V}(x, y, p, t)$ over a sufficiently long period of time and to a great enough height in the atmosphere, we could compute, from (63), the geographical distribution of $\nabla \times \overline{\boldsymbol{\tau}}_s$, and from this and the field of $\overline{\mathbf{V}}_s$ obtain the geographical distribution of the surface stress coefficient $K(x, y)$ (Mintz, 1956).

Unfortunately, the data on \mathbf{V} are still not available in a form that will permit this to be done without an excessive amount of labor. But we can reduce equation (63) to a form which permits us, with available data, to obtain the overall mean value of the stress coefficient, K_m .

Using spherical coordinates,

$$\mathbf{k} \cdot \nabla \times \overline{\boldsymbol{\tau}}_s = \frac{1}{a \cos \varphi} \left[\frac{\partial}{\partial \lambda} \overline{\tau}_{y,s} - \frac{\partial}{\partial \varphi} (\overline{\tau}_{x,s} \cos \varphi) \right], \quad (64)$$

and when the wind is non-divergent,

$$\begin{aligned} \overline{\mathbf{v} \cdot \nabla (\zeta + f)} = & -\frac{1}{a^2 \cos^2 \varphi} \left\{ \cos \varphi \frac{\partial}{\partial \varphi} \left[\frac{1}{\cos \varphi} \frac{\partial}{\partial \varphi} (\overline{uv} \cos^2 \varphi) \right] \right. \\ & \left. - \frac{\partial^2}{\partial \lambda^2} (\overline{uv}) + \frac{\partial^2}{\partial \lambda \partial \varphi} [(\overline{u^2} - \overline{v^2}) \cos \varphi] \right\} + \frac{\overline{v}}{a} \frac{\partial f}{\partial \varphi}, \end{aligned} \quad (65)$$

where λ is longitude, φ is latitude, a is the radius of the earth, and the subscripts x and y denote respectively the eastward and northward components of the quantity. Also,

$$g f_m \overline{\varrho_s \mathbf{V}_s} \cdot \nabla_H H_s = \frac{g f_m}{a} \left[\frac{\overline{\varrho_s u_s}}{\cos \varphi} \frac{\partial H_s}{\partial \lambda} + \overline{\varrho_s v_s} \frac{\partial H_s}{\partial \varphi} \right], \quad (66)$$

and when the surface wind is quasi-geostrophic, or $\mathbf{V}_s = \frac{1}{f_m \varrho_s} \mathbf{k} \times (\nabla_H p_s)$,

$$\begin{aligned} g f_m \overline{\varrho_s \mathbf{V}_s} \cdot \nabla_H H_s = & \frac{g}{a^2 \cos \varphi} \left[\left(\frac{\partial \overline{p}}{\partial \lambda} \right)_s \frac{\partial H_s}{\partial \varphi} - \left(\frac{\partial \overline{p}}{\partial \varphi} \right)_s \frac{\partial H_s}{\partial \lambda} \right] \\ = & \frac{g}{a^2 \cos \varphi} \left[\frac{\partial}{\partial \lambda} \left(\overline{p} \frac{\partial H_s}{\partial \varphi} \right)_s - \frac{\partial}{\partial \varphi} \left(\overline{p} \frac{\partial H_s}{\partial \lambda} \right)_s \right]. \end{aligned} \quad (67)$$

Substituting (64), (65) and (67) into equation (63) and taking the zonal average, we obtain

$$\begin{aligned} \frac{\partial}{\partial \varphi} (\overline{\tau}_{x,s} \cos \varphi) = & -\frac{1}{g a} \frac{\partial}{\partial \varphi} \left(\frac{1}{\cos \varphi} \frac{\partial}{\partial \varphi} \right) \int_0^{p_s} \overline{uv} \cos^2 \varphi \delta p - \\ & - \frac{1}{a} \frac{\partial}{\partial \varphi} \left(\overline{p} \frac{\partial H_s}{\partial \lambda} \right)_s, \end{aligned} \quad (68)$$

where the superior curved bar denotes the average taken with respect to longitude completely around the earth, from $\lambda = 0$ to $\lambda = 2\pi$.

Integrating (68) with respect to latitude over the polar cap from φ to $\varphi = \pi/2$, we obtain, for the latitude φ ,

$$\overline{\tau}_{x,s} = -\frac{1}{ga \cos^2 \varphi} \frac{\partial}{\partial \varphi} \int_0^{\pi/2} \overline{uv} \cos^2 \varphi \delta \varphi - \frac{1}{a \cos \varphi} \left(\overline{p_s} \frac{\partial H_s}{\partial \lambda} \right). \quad (69)$$

In general,

$$\overline{uv} = \overline{uv} = \overline{u'v'} + \overline{uv}, \quad (70)$$

where the prime superscript denotes the instantaneous local deviation from the longitude-mean. But because \mathbf{v} is the non-divergent component of the horizontal velocity, ($\mathbf{v} = \mathbf{k} \times \nabla \psi$), we have

$$\overline{v} = \frac{1}{2\pi a \cos \varphi} \int_0^{2\pi} \frac{\partial \psi}{\partial \lambda} \delta \lambda = 0, \quad (71)$$

and

$$\overline{u'v'} = \overline{u'v'}. \quad (72)$$

Substituting from (72) into (69), multiplying through by $2\pi a^3 \cos^2 \varphi$, and integrating once again with respect to latitude over the polar cap, from φ to $\varphi = \pi/2$, we obtain

$$2\pi a^3 \int_{\varphi}^{\pi/2} \overline{\tau}_{x,s} \cos^2 \varphi \delta \varphi = \frac{2\pi a^2}{g} \cos^2 \varphi \int_0^{\pi/2} \overline{u'v'} \delta \varphi - 2\pi a^2 \int_{\varphi}^{\pi/2} \left(\overline{p_s} \frac{\partial H_s}{\partial \lambda} \right) \cos \varphi \delta \varphi. \quad (73a)$$

For convenience of discussion, we will denote the three terms in equation (73a) respectively as \overline{T}_{φ} , \overline{J}_{φ} and \overline{P}_{φ} , or

$$\overline{T}_{\varphi} = \overline{J}_{\varphi} - \overline{P}_{\varphi}. \quad (73b)$$

T_{φ} is the net torque of the atmosphere upon the earth due to surface friction in the polar cap bounded by latitude φ .

P_{φ} is the net torque of the atmosphere upon the earth in the polar cap bounded by latitude φ due to zonal pressure differences across the orographic features of the earth's surface; it is positive when there is a positive correlation between surface air pressure and the zonal slope of the earth's surface, as illustrated schematically in Figure 10b.

J_{φ} is the horizontal eddy flux of angular momentum into the polar cap through the latitude surface φ . It is positive if there is a positive correlation between the wind components u' , v' , as illustrated schematically (for a westerly wave) in Figure 10c.

If, instead of the approximate vorticity equation (1), we had begun with the complete vorticity equation and integrated over the polar cap, as above—or if we had begun

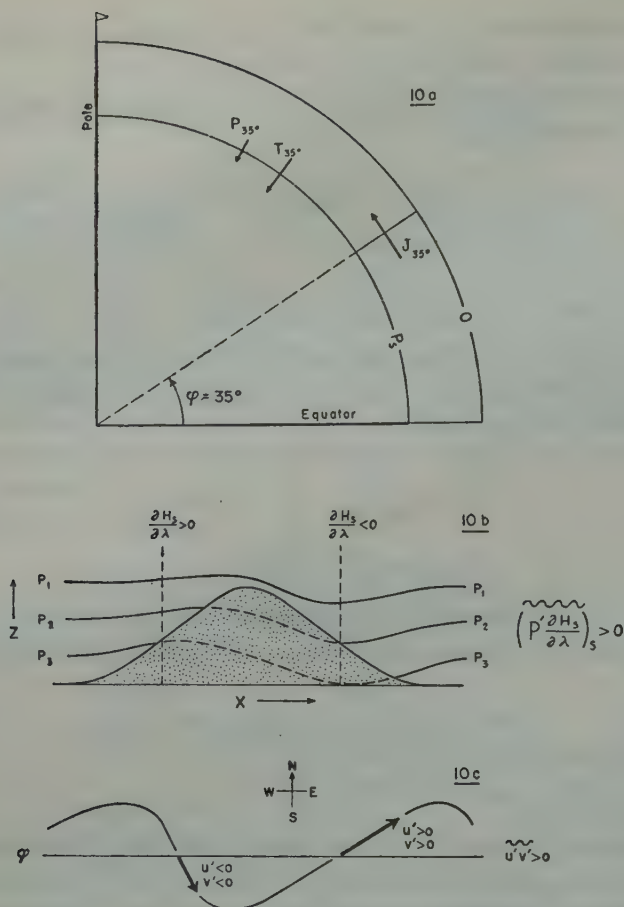


Figure 10

- a) Angular momentum budget of the air in the polar cap bounded by latitude $\varphi = 35^\circ$.
 b) Distribution of pressure which produces a westerly torque upon the earth.
 c) A westerly wave which transports momentum polewards.

more directly with the primitive equation of zonal motion—the final expression for \overline{T}_φ , corresponding to (73), would contain some additional small terms (cf. Mintz, 1955a). The largest of these additional small terms is $2\pi a^2 \cos^2 \varphi \int_0^{p_0} \overline{\overline{u'v'}} \delta p/g$, which is the poleward flux of angular momentum through the latitude surface φ due to the mean meridional circulation $\overline{\overline{v}}$. But latitude 35° is near the position which separates the positive Hadley cell from the negative Ferrel cell of the mean meridional circulation, and the momentum flux due to the meridional circulation is therefore very small at this latitude and can be neglected (cf. Mintz and Lang, 1955; Bjerknes and Venkateswaran, 1957).

The true role of the poleward horizontal eddy flux of angular momentum in the maintenance of the mean zonal motion of the atmosphere was first recognized by

Jeffreys (1926, 1927, 1933). He showed that the previously held view — that the large-scale atmospheric disturbances were perturbations upon a basic zonal current which was capable of an independent existence — was incorrect, and that the mean zonal wind could not exist *without* the eddies. But it was not until many years later that the order of magnitude of the eddy flux of angular momentum was first evaluated from the aerological data: by Priestly (1949), using the radar-observed wind to high levels at a single station in southern England; by Widger (1949), independently, using the geostrophic wind at sea level, 700- and 500-mb around the northern hemisphere; and by Mintz (1949), independently, using the radar-observed wind to high levels at 10 stations across North America and the 500-mb geostrophic wind around the northern hemisphere.

In addition to the magnitude of the momentum flux, these and later studies have shown that the ratio of the large-scale eddy flux of angular momentum to the space-averaged or time-averaged gradient of angular momentum is not constant, but varies in space and time. In fact, the flux is sometimes observed to be in the direction *opposite* to the gradient (so that the fluid may then facetiously be described as having a “negative viscosity”). Moreover, the observed ratio has no apparent relation to the ratio of flux to gradient of other atmospheric properties, such as the sensible heat. For these reasons the “Grossaustausch” concept of Defant (1921), which by analogy with molecular and small-scale eddy motions describes the maintenance of the mean zonal wind as a large-scale diffusion process, is incorrect. We are dealing with a thermally active system in which over one part of the spectrum of motions there is a transfer of kinetic energy *from* the smaller scale *to* the larger scale motion. Therefore, to understand the dynamics of this system, we must integrate the differential equations which describe the *individual details of the velocity* in that part of the spectrum of motions which generates the kinetic energy. It has been known for some time (i.e. Bjerknes, 1935; Mintz, 1947) that the kinetic energy of the general circulation is generated by the cyclonic-scale motions—by the familiar cyclones and anti-cyclones of the weather map and their associated upper level circulations, which have a characteristic wave length of 3000 to 4000 km.

To insure that the data for all of the terms in our computation of the surface stress coefficient shall be homogeneous, we will use the numerical data from the U.C.L.A. general circulation investigation.

Figure 11 shows the quantity $\overline{u'v'}$ at latitude 35°N , for the months January-February-July-August 1949, from the U.C.L.A. study (Mintz, 1955b). The winds used are geostrophic, with the approximations

$$u = -\frac{1}{a} \cdot \frac{\Delta\psi}{\Delta\varphi} \quad \text{and} \quad v = \frac{1}{a \cos \varphi} \cdot \frac{\Delta\psi}{\Delta\lambda},$$

$$\text{where} \quad \psi = \frac{gZ}{2\Omega \sin \varphi_{35}} \quad \text{and} \quad \Delta\varphi = \Delta\lambda = \frac{2\pi}{36}. \quad (74)$$

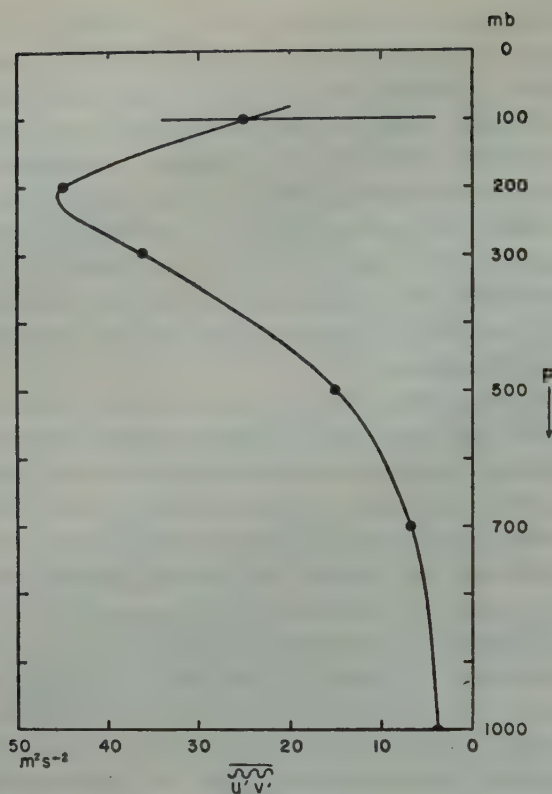


Figure 11

$\overline{u'v'}$, computed from the geostrophic winds at 35°N , in Jan.-Feb.-July-Aug. 1949.

Using these values of $\overline{u'v'}$, and integrating from 1000- to 100-mb—thereby neglecting the flux in the uppermost ten per cent of the mass of the atmosphere, which extrapolation of the upper part of the curve in the figure suggests would be only a small error—we obtain

$$\overline{J}_{35^\circ} = 2.86 \times 10^{16} \text{ t m}^2 \text{ s}^{-2}. \quad (75)$$

It is important to compare the momentum flux obtained from the geostrophic wind in this way with the flux computed from radar wind and pilot balloon observations. When the geostrophic wind is computed by taking contour height differences over ten degrees of latitude and longitude, as above, which at 35° latitude are distances of about 1000 km, we are, in effect, smoothing out all disturbances in the wind field of a smaller size and are computing the momentum flux due only to eddies having a wave length longer than 1000 km. On the other hand, the wind as measured by the standard pilot balloon or radar tracking method is the wind averaged over a two minute interval during which the balloon drifts horizontally only some few kilometers.

The momentum flux computed from these winds will therefore contain the contribution of all horizontal eddies larger than a few kilometers in wave length.

Fortunately, at latitude 30°N we have momentum flux computations on a seasonal basis computed from both kinds of winds. The flux at 30°N computed from the geostrophic wind for the two summer months, July–August 1949, was $1.27 \times 10^{16} \text{ t m}^2 \text{ s}^{-2}$, and for the two winter months, January–February 1949, it was $4.50 \times 10^{16} \text{ t m}^2 \text{ s}^{-2}$ (Mintz, 1955b). In addition, we have the poleward eddy flux of angular momentum computed from the radar and pilot balloon observed wind at 19 stations distributed around the globe in the vicinity of latitude 30°N (Starr and White, 1952): for the six summer months, May to October 1949, this flux averaged $2.05 \times 10^{16} \text{ t m}^2 \text{ s}^{-2}$, and for the six months February, March, April, November and December 1949 together with January 1950, considered as forming a composite winter season, it averaged $3.95 \times 10^{16} \text{ t m}^2 \text{ s}^{-2}$.

Assuming that the flux varies with only an annual period and with its maximum in mid-winter, these values give us, respectively,

$J_{30^\circ, \text{geostr.}} = (2.9 + 1.7 \sin \odot) \times 10^{16} \text{ t m}^2 \text{ s}^{-2}, \tag{76}$

and $J_{30^\circ, \text{rawin-pibal}} = (3.0 + 1.5 \sin \odot) \times 10^{16} \text{ t m}^2 \text{ s}^{-2}, \tag{77}$

where \odot denotes the time of the year ($\odot = 0, 2\pi$ on November 1, $\odot = \pi/2$ on February 1, etc.) (cf. Figure 12).

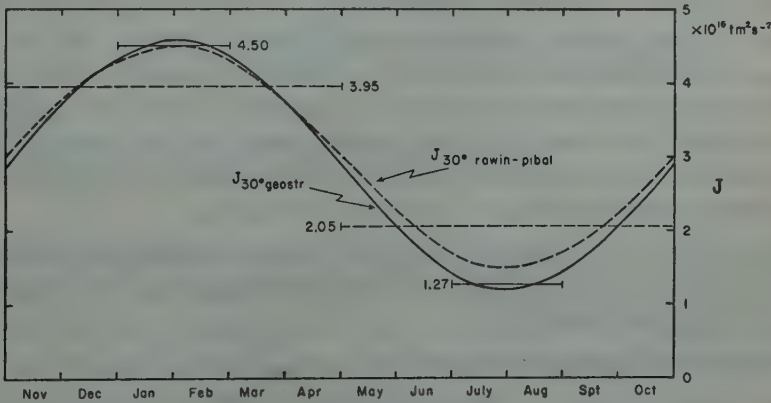


Figure 12

The poleward eddy flux of angular momentum at latitude 30°N, computed from the radar and pilot balloon winds (Starr and White, 1952) and from the geostrophic winds (Mintz, 1952).

The fact that the two fluxes are so very close in mean magnitude and in seasonal amplitude is probably to some extent coincidental. What is significant is that the flux computed from the radar and pilot balloon wind is not substantially larger than the flux computed from the space smoothed geostrophic wind. (The same is also true in other latitudes, where we can compare the mean annual fluxes, and where there is a large gradient of the mean zonal wind: cf. Starr and White, 1955; Mintz,

1955b). The interpretation we must put on this is that eddies in the range of about 1 to 1000 km in wave-length contribute very little, if anything, to the horizontal flux of momentum. If we assume that eddies smaller than 1 km also contribute very little to the horizontal momentum flux (cf. Panofsky and Crutcher, 1951), then the lateral eddy stress can be neglected compared to the advective transport of momentum by the cyclonic-scale geostrophic wind. The agreement between (76) and (77) justifies the approximation made in equation (1), where the frictional force is dependent only on the vertical eddy stress and the lateral eddy stress is neglected.

Before we can compute \bar{P}_ϕ , the mean westerly torque upon the earth due to the correlation between surface air pressure and the slope of the earth's surface, we must first decide what part of the spectrum of the earth's topographic irregularities we will include in this term. It is clear that the dividing line between this term and the \bar{T}_ϕ term is an arbitrary one, because what we call the surface (or skin-friction) stress may include the forces due to horizontal pressure differences across individual hills, individual trees and blades of grass, or the horizontal pressure differences across individual grains of sand.

The distinction between \bar{P}_ϕ and \bar{T}_ϕ must be an operational one, depending upon the way in which we intend to use the prediction equations (34) and (35). In the experiments described in this paper these equations will be replaced by their finite difference equivalents in which all gradients, including $\nabla_H \bar{p}_s$, the slope of the earth's surface in x, y, z -space, will be replaced by differences over two grid intervals. The grid interval we will use will be of the order of 200–400 km. Therefore, the surface stress coefficient which we require is one which will include the horizontal forces due to all scales of surface roughness up to twice this grid interval, leaving for the orographic term in our computations only that part of the spectrum of the earth's irregularities which is larger than two grid intervals.

Accordingly, for the computation of the \bar{P}_ϕ term we have used the space-averaged topography given by Berkofsky (1955), in which the averaging was done over intervals of 5° of latitude and longitude.

For convenience of computation, we let

$$\bar{p} = \bar{\tilde{p}} + \bar{p}'.$$

Then

$$\bar{p} \frac{\partial H}{\partial \lambda} = \bar{\tilde{p}} \frac{\partial H}{\partial \lambda} + \bar{p}' \frac{\partial H}{\partial \lambda},$$

and

$$\left(\bar{\tilde{p}} \frac{\partial H_s}{\partial \lambda} \right) = \left(\bar{p}' \frac{\partial H}{\partial \lambda} \right), \quad (78)$$

where the prime superscript denotes the deviation from the longitude mean.

'By linear interpolation between \bar{p}' at sea level and \bar{p}' at 10,000 feet (obtained from the 700-mb height field), averaged for the four months Jan.–Feb.–July–Aug. 1949,

\overline{p}' was obtained for the ground level given by the space smoothed topography. From this and $\partial H_s/\partial \lambda$ given by the space smoothed topography, we obtain the distribution of $\left[\overline{p}'(\partial H_s/\partial \lambda)\right]_s$ shown in Figure 13.

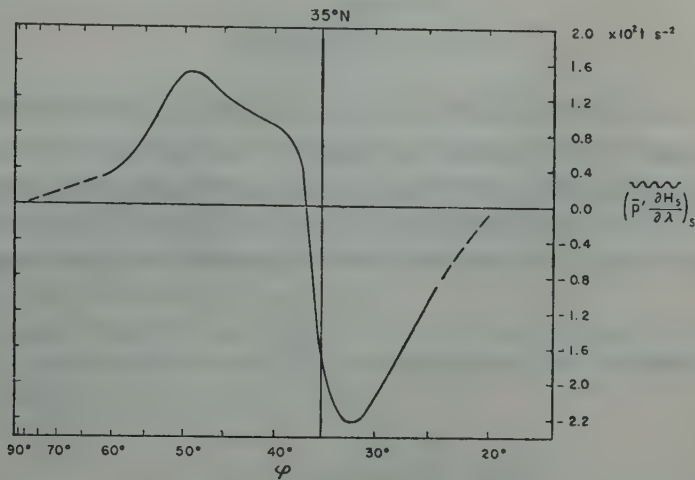


Figure 13
The pressure term, $\left[\overline{p}'(\partial H_s/\partial \lambda)\right]_s$, for Jan.-Feb.-July-Aug. 1949.

Integrating from latitude 35°N to the pole, we obtain

$$\overline{P}_{35^\circ} = 0.67 \times 10^{16} \text{ t m}^2 \text{ s}^{-2} . \tag{79}$$

White (1949) computed this term from maps of normal pressure, using a topography broken down into 1-km vertical blocks, and (neglecting the torque north of 65°) obtained, for the yearly mean, $\overline{P}_{35^\circ} = 0.59 \times 10^{16} \text{ t m}^2 \text{ s}^{-2}$. Of course, if we were to use a more detailed surface topography we would obtain a larger value for this term and consequently a smaller value for the surface stress coefficient. But this is precisely what we do not want for the experiments we are now concerned with.

From (73), (75) and (79), the mean zonal torque of the atmosphere upon the earth, due to surface friction in the polar cap north of latitude 35°, is therefore

$$\overline{T}_{35^\circ} = (2.86 - 0.67) \times 10^{16} \text{ t m}^2 \text{ s}^{-2} = 2.19 \times 10^{16} \text{ t m}^2 \text{ s}^{-2} . \tag{80}$$

From equations (9) and (10),

$$2\pi a^3 \int_{\varphi}^{\pi/2} \overline{\tau}_{x,s} \cos^2 \varphi \, \delta \varphi = 2\pi a^3 K_m \int_{\varphi}^{\pi/2} \overline{u_s S(\gamma_{3-4})} \cos^2 \varphi \, \delta \varphi .$$

Neglecting any correlation between the geostrophic surface wind and the static stability, this gives us

$$K_m = \frac{\bar{T}_\phi}{\bar{U}_\phi S(\gamma_{3-4})_m} \quad (81)$$

where

$$\bar{U}_\phi = 2\pi a^3 \int_{\phi}^{\pi/2} \bar{\bar{u}}_s \cos^2 \phi \, d\phi. \quad (82)$$

The latitudinal distribution of the mean zonal geostrophic surface wind, $\bar{\bar{u}}_s$, for the four months of 1949 is shown in Figure 14. The zonal surface wind, \bar{u}_s , was first found for the surface elevation given by the space smoothed topography by using linear interpolation between the wind at sea level and the wind at 700-mb (10,000 feet), at every 5° of longitude. Then the longitude average of \bar{u}_s was taken to obtain $\bar{\bar{u}}_s$.

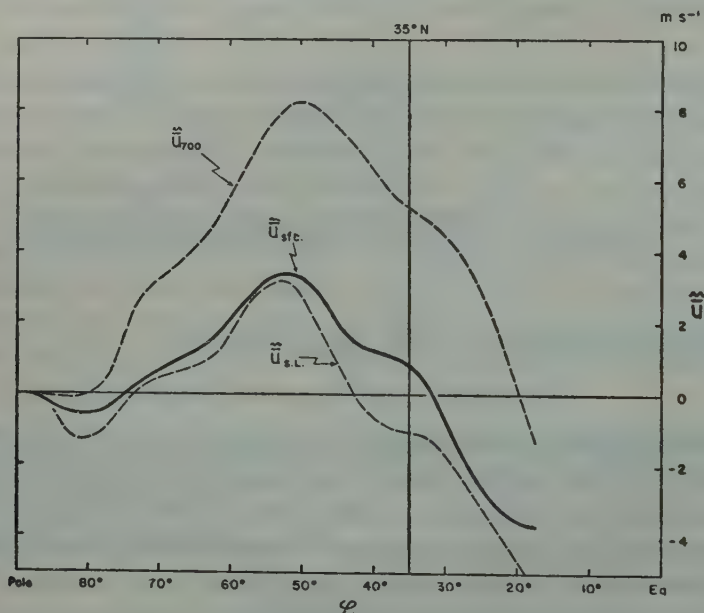


Figure 14

The geostrophic zonal wind at the earth's surface, sea level and 700-mb, averaged over all longitudes in Jan.-Feb.-July-Aug. 1949.

For the purpose of comparison, Figure 14 also shows $\bar{\bar{u}}_{SL}$ and $\bar{\bar{u}}_{700}$, the zonal winds averaged at sea level and at 700-mb individually. We note that at sea level, in this period, the transition from tropical easterly to mid-latitude westerly zonal wind was at 43°N , and at 700-mb the transition was at 19°N . But the mean surface zonal wind changed from easterly to westerly at 32°N , which is almost exactly the latitude of the

observed maximum in the poleward angular momentum flux for this period (Mintz 1955b).

Using the observed distribution of \bar{u}_s , we obtain, by integration of (82),

$$\bar{U}_{35^\circ} = 6.90 \times 10^{20} \text{ m}^4 \text{ s}^{-1}. \quad (83)$$

The mean value of γ_{3-4} is $0.5^\circ \text{C cb}^{-1}$, and from (58),

$$S(\gamma_{3-4})_m = 1.0. \quad (84)$$

Substituting, finally, from (80), (83) and (84) into (81), we obtain

$$K_m = 0.32 \times 10^{-4} \text{ t m}^{-2} \text{ s}^{-1} = 0.32 \text{ dyne cm}^{-2}/\text{m s}^{-1}. \quad (85)$$

This value for the surface stress as a function of the surface geostrophic wind is about $1\frac{1}{2}$ times as large as that which can be derived from the conventional ways of estimating the surface stress. Phillips (1956), for example, obtained and used the equivalent of $K_m = 0.20 \times 10^{-4} \text{ t m}^{-2} \text{ s}^{-1}$.

But if we were to neglect the pressure term in (73), so that every scale of surface roughness was included as part of the skin-friction stress, then, from (80) and (81), we would obtain $K_m = 0.42 \times 10^{-4} \text{ t m}^{-2} \text{ s}^{-1}$.

III. THE HEATING FUNCTION, $Q(x, y, t)$

We can characterize the atmosphere-earth system as a thin layer of gas gravitationally held to a rotating sphere upon which there falls a beam of parallel radiation from a distant source, the declination of the beam varying with an annual period. Very little of the incident radiation is absorbed by the gas, but a sizable part is reflected and the remainder is absorbed by the underlying sphere. By involved and complex processes of heat exchange there is a net transfer of energy from the sphere to the gas. At the same time, the gas itself radiates energy to space.

The net heating of a unit column of the gas, or atmosphere, Q , is equal to the heat transfer from the earth to the atmosphere, Q_4 , minus the heat radiated by the atmosphere to space, Q_0 .

For the energy radiated by the atmosphere to space, Q_0 , we will assume, in our model, that all of it originates at some level, $p < p_1$, at which the horizontal temperature gradient is negligibly small. (Up to this point, we have not specified in any way the temperature distribution above the level p_1). Consequently we assume, in the model, that the energy radiated to space, Q_0 , is a constant. This treatment of the outgoing atmospheric radiation is very similar to that used by Simpson (1929) for the real atmosphere.

In the real atmosphere, the heat transfer from the earth to the air takes place in a complex way. Part of the transfer is due to radiative exchange between earth and air, part is due to conduction at the earth-air interface, and part is due to evaporation of water from the earth (cooling the earth) and condensation in the atmosphere (warming the air).

In the real atmosphere, the heat transfer by radiation depends on the ground-air temperature contrast, the water vapor distribution and the cloudiness. The heat transfer by conduction depends directly on the small temperature difference at the earth-air interface, but indirectly it depends on the temperatures above the interface because the temperature lapse rate in the lower levels of the air determines how rapidly eddy diffusion transfers the conducted heat away from the interface. And the heat transfer by evaporation-condensation depends to a large extent on the temperature lapse rate in the lower layers of the air because much of the condensation and precipitation is of the convective type, especially in the lower latitudes.

In our model we will make the heat transfer from earth to atmosphere, Q_4 , proportional to the temperature difference between the ground and the air — the temperature of the air, for this purpose, being taken as the temperature at the level p_2 . Because we have set $T_g \approx T_4$, this is equivalent to making the heat transfer from earth to air dependent on the temperature lapse rate in the lower half of the atmosphere.

With these assumptions, we have

$$Q(x,y,t) = Q_4(x,y,t) - Q_0 = b\Delta T(x,y,t) - Q_0 \quad (86)$$

where $\Delta T = (T_g - T_2)$ and b is the constant of proportionality.

Taking the global average of (86), we obtain

$$Q_m = b(\Delta T)_m - Q_0 = 0, \quad (87)$$

where the subscript m denotes the time- and space-average over the entire system.

Substituting for Q_0 from (87) into (86), we obtain the simple heating function

$$Q = b[\Delta T - (\Delta T)_m]. \quad (88a)$$

According to this heating function, whenever the lapse rate in the lower half of the atmosphere is larger than the mean lapse rate the heat transfer from earth to air will be larger than from the air to space, and there will be a net heating of the atmospheric column. But when ΔT is smaller than $(\Delta T)_m$, the upward heat flow from earth to air will be smaller than the heat loss to space and there will be a net cooling of the column. These two conditions are illustrated schematically in Figure 15.

For $(\Delta T)_m$ we will use the mean 500-mb temperature, $T_{2,m} = -15.2^\circ\text{C}$ (Burdecki, 1955), and the mean surface temperature, $T_{g,m} = 15.6^\circ\text{C}$, obtained from the normal sea surface temperatures (Sverdrup, 1942) and, over the lands, the normal surface air temperatures reduced to sea level (Hann-Suring, 1939). These give us

$$(\Delta T)_m = 30.8^\circ\text{C}. \quad (89)$$

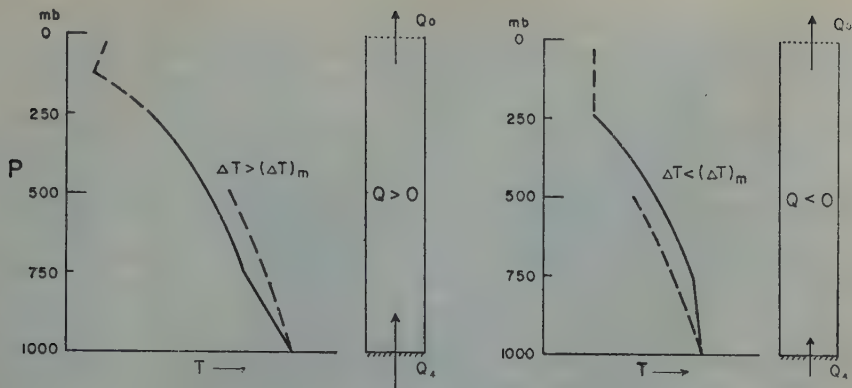


Figure 15

The net heating of an atmospheric column as a function of the earth-air temperature difference.
 $\Delta T = T_g - T_2$.

For Q_0 we will use the average value, $Q_{0,m}$, from recent estimates made for the real atmosphere by different authors. In the real atmosphere, unlike our model, there is some direct absorption of solar radiation by the atmosphere. To obtain the net radiative exchange that takes place directly between the atmosphere and space, we will subtract this direct absorption from the long wave radiation emitted by the atmosphere to space. The estimates are shown in Table I.

TABLE I
Mean radiation, in $10^5 \text{ cal m}^{-2} \text{ day}^{-1}$

	London (1951)	Houghton (1954)	Alissow, Drosdow, and Rubinstein (1956)
Long wave radiation emitted by the atmosphere to space	41	41	38
Short wave radiation absorbed by the atmosphere	9	13	14
Difference	32	28	24

Taking the average of these values, we have

$$Q_0 = 28 \times 10^5 \text{ cal m}^{-2} \text{ day}^{-1}. \tag{90}$$

Substituting from (89) and (90) into (87), we obtain

$$b = 0.90 \times 10^5 \text{ cal m}^{-2} \text{ day}^{-1} \text{ deg}^{-1}, \tag{91}$$

and from (88a),

$$Q = 0.90 (\Delta T - 30.8) \times 10^5 \text{ cal m}^{-2} \text{ day}^{-1}.$$

(88b)

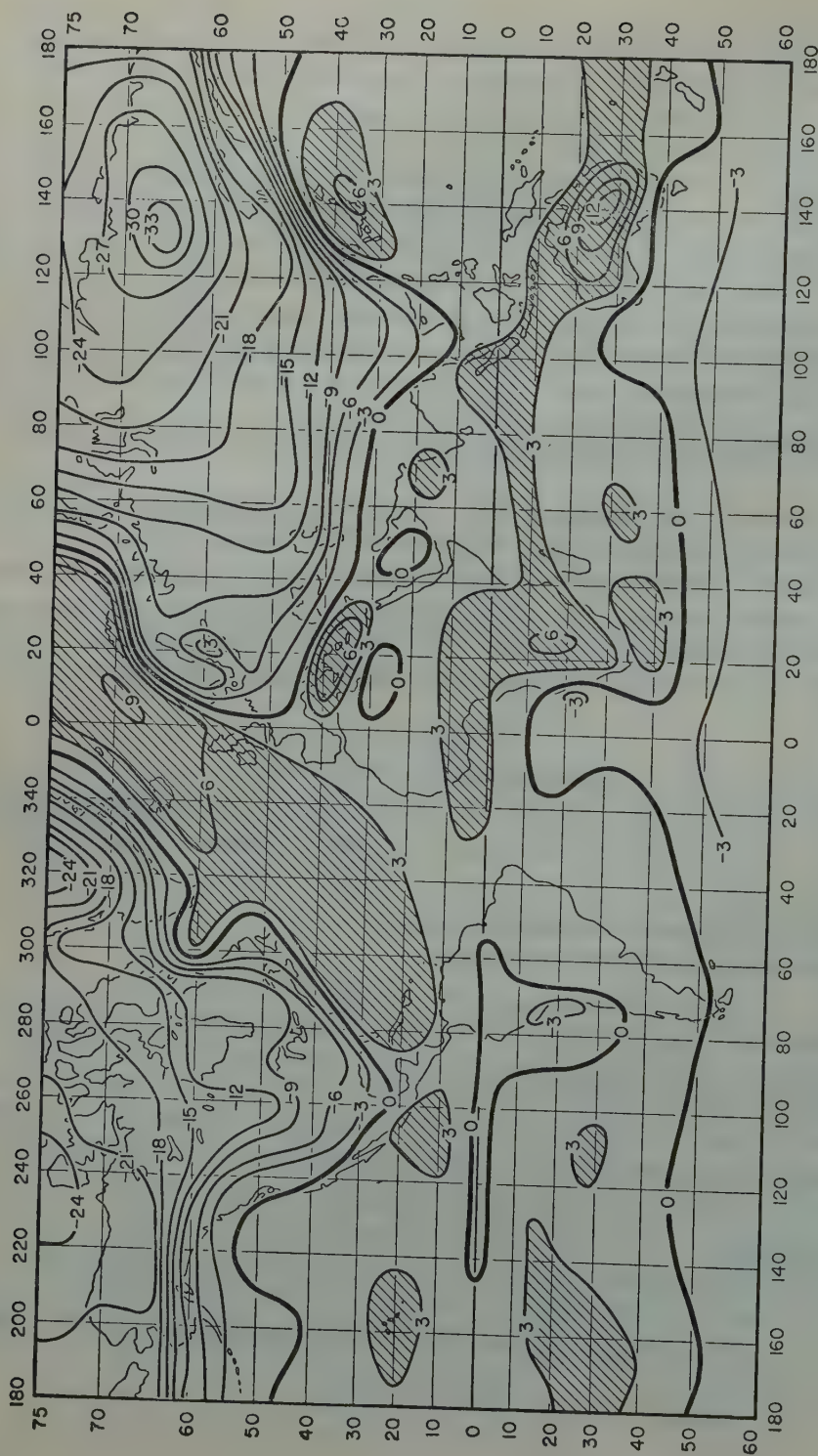


Figure 16

The computed normal heating of the atmosphere in January in $10^5 \text{ cal m}^{-2} \text{ day}^{-1}$.

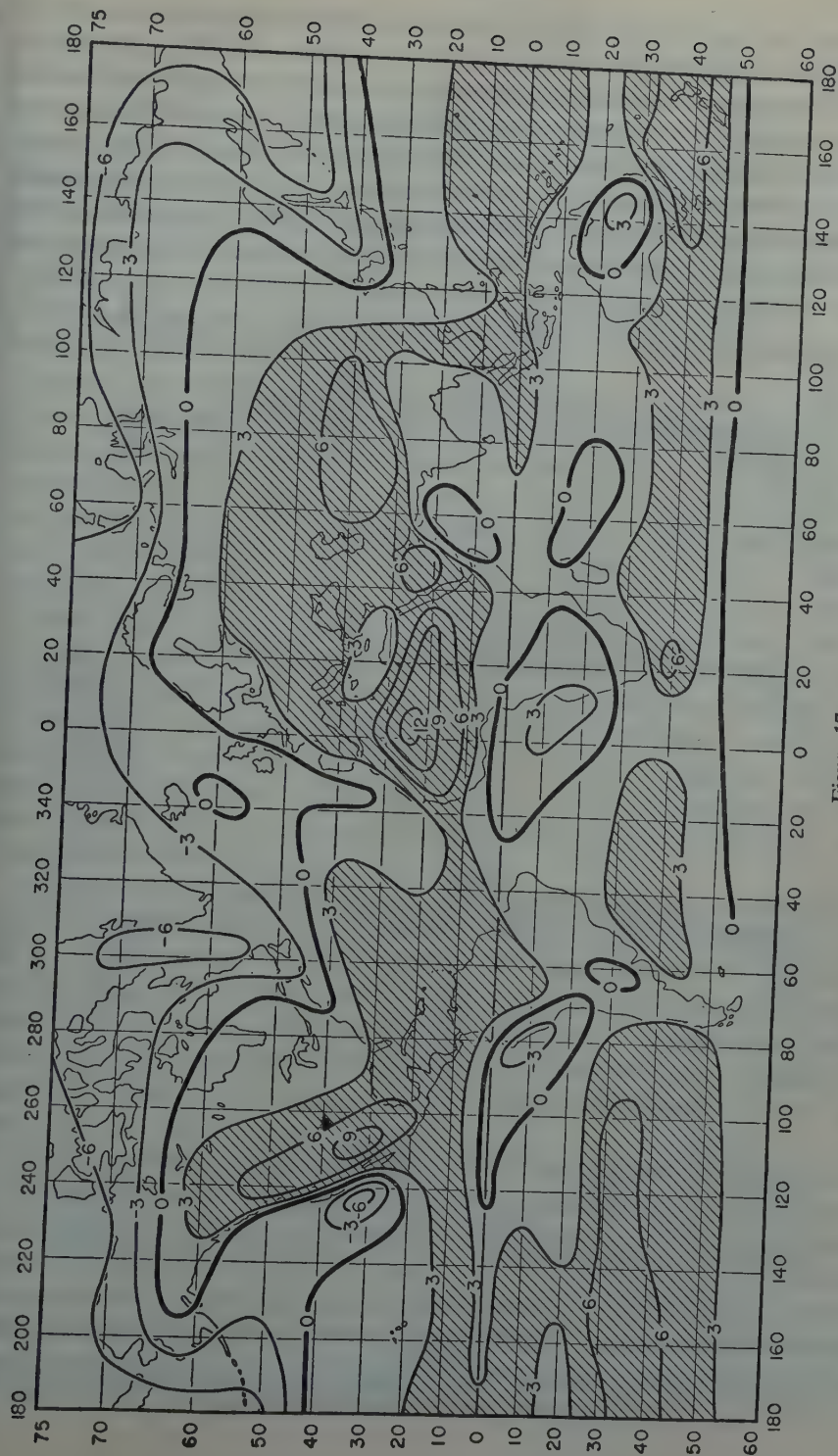


Figure 17
The computed normal heating of the atmosphere in July in $10^5 \text{ cal m}^{-2} \text{ day}^{-1}$.

As a check on whether this heating function is able to reproduce the essential features of the heating and cooling of the real atmosphere, we have applied (88b) to the real atmosphere. For the temperature, T_2 , we used the world charts of normal 500-mb temperature, for the winter and summer seasons respectively, compiled by Upper Air Climatology Branch of the Meteorological Office of Great Britain. These charts were kindly supplied to the writer in manuscript form by the Director of the Meteorological Office. The winter and summer surface temperatures were taken, as before, from Sverdrup and Hann-Suring. The results of the test are shown in Figures 16 to 18.

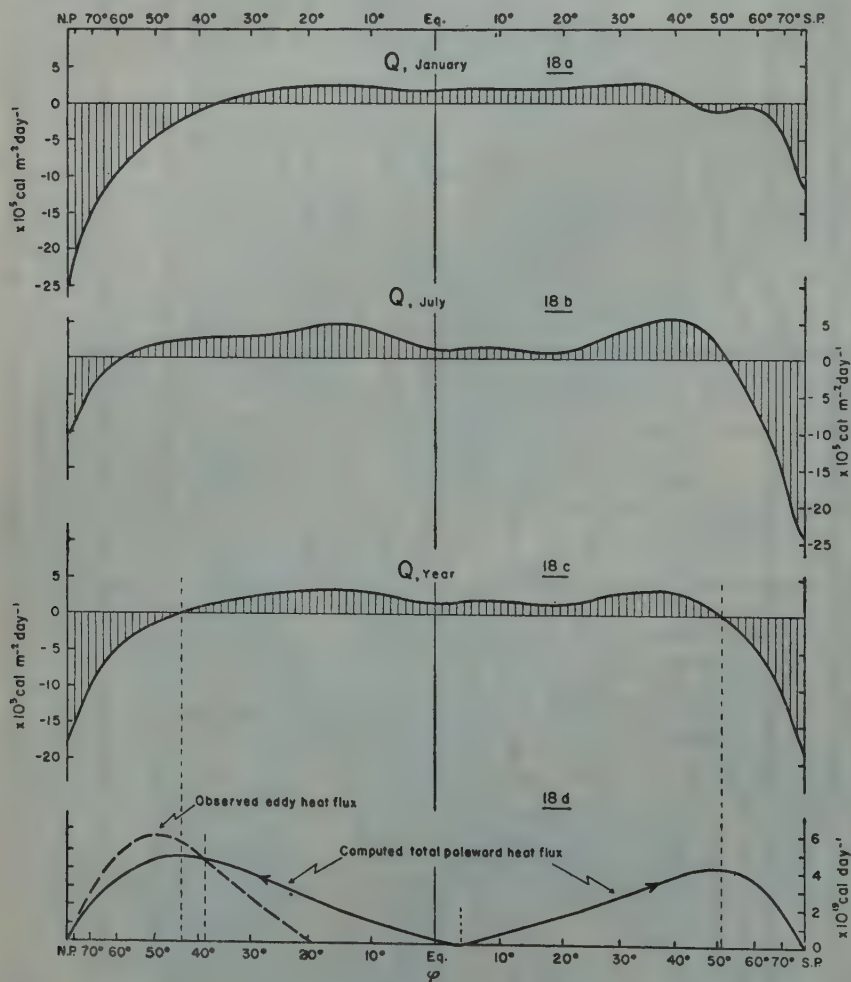


Figure 18

- (a, b, c) The computed heating of the atmosphere in January, July, and for the year, as a function of latitude.
- (d) The atmospheric poleward heat flux. The continuous line shows the computed total flux. The broken line shows the observed eddy flux.

During northern hemisphere winter (Figure 16), our heating function shows a net cooling of the atmosphere over Canada, the United States and Greenland and over central and eastern Europe and Asia, with the maximum cooling in northeastern Asia. A broad band of heating extends from southwest to northeast over the Atlantic, with its maximum between Norway and Greenland. There is a heating maximum over the Mediterranean and another maximum off the east coast of Japan. A band of heating extends from the central south Pacific, across Australia, where it has its maximum, and across the south Indian Ocean to Africa and to the eastern Atlantic north of the equator. Cooling is found in the eastern parts of the subtropical southern hemisphere oceans. In the middle and higher latitudes of the southern hemisphere there is cooling.

During the northern hemisphere summer (Figure 17), a band of heating extends across the tropical Pacific, across central Asia, with a maximum over the highlands of Asia, across southern Europe and north Africa, with a relative minimum over the eastern Mediterranean and a strong maximum over Africa, across the tropical Atlantic and across western North America, where there is another maximum over the land of high elevation. There is cooling in the higher latitudes over the continents, and cooling in middle latitudes over the oceans and over the eastern parts of the subtropical oceans. (Cooling signifies a smaller upward heat transfer from earth to air than from air to space.) In the southern hemisphere, in its winter season, there is a middle latitude band of heating circling the globe corresponding to the band of heating over the north Atlantic during northern hemisphere winter). Between the southern hemisphere middle latitude band of heating and the northern hemisphere tropical band of heating, there is a zone of cooling, with maxima over Australia, and the eastern south Atlantic and Pacific. In the higher southern latitudes, there is cooling.

Of course, all that we have shown in these two figures is the observed distribution of ΔT , the vertical temperature gradient in the lower half of the atmosphere, expressed as the net heating of the atmosphere according to (88b). But it is surprising how well these patterns conform to our preconception of what the true distribution of the heating and its changes with the seasons ought to be. Unfortunately, we do not know the quantitative geographical distribution of the true heating, so that we cannot make any more critical comment on Figures 16 and 17 than to say that the patterns "look reasonable".

A more critical test of the heating function is obtained by taking the zonal average of the heating. The zonal averages of the fields given in Figures 16 and 17 are shown, respectively, in Figures 18a and 18b (poleward of 60°S , the temperatures T_2 were taken from Burdecki, 1955). The figures show net heating in the lower latitudes, net cooling in the higher latitudes. In January, there is zero net heating at 37°N and averaged over the whole of the northern hemisphere there is a net cooling (which can be balanced by a northward heat flux across the equator). In July, the latitude of zero heating has shifted to 58°N and averaged over the whole of the northern

hemisphere there is a net heating (which can be balanced by a southward heat flux across the equator). It will be noticed that averaged from pole to pole there is a very small net cooling in January and net heating in July.

One shortcoming in the distribution of heating shown in these figures is the absence (or underestimate) of the narrow belt of intense heating which we expect to find in the regions of the heavy intertropical convergence rains. But this, it should be pointed out, is very likely not a shortcoming of our heating function but of the temperature data used in the computations. The 500-mb temperatures that we used showed broad maxima of temperature in the equatorial regions. But the detailed temperature analysis over the Atlantic by Schnapauff (1936) has shown that the air in the middle troposphere is colder along the line of intertropical convergence than it is on either side. This is probably true for the line of intertropical convergence generally, and if we were to introduce such a minimum in the 500-mb equatorial temperature field our heating function would show the expected equatorial heating maxima.

Figure 18c shows the average of the January and July computed heating. Integrating this heating over the polar caps bounded by each latitude φ , we obtain the poleward atmospheric heat flux shown by the continuous line in Figure 18d. Beginning at about latitude 4°S there is a heat flux directed toward each pole, with the two maxima, 4.7×10^{19} cal day $^{-1}$ at 43°N and 4.3×10^{19} cal day $^{-1}$ at 51°S .

For comparison we show the observed northern hemisphere eddy flux of heat (Mintz, 1955b) by the broken line in Figure 18d. As we pointed out earlier, 35°N is about the latitude which separates the Hadley cell from the Ferrel cell of the mean meridional circulation. Therefore the heat flux due to the mean meridional circulation (like the momentum flux) is very small near this latitude. We notice, in Figure 18d, that the curves for the computed total flux and for the observed eddy flux cross at latitude 38°N . In the lower latitudes, where the Hadley cell operates, we expect the total flux to be greater than the eddy flux, and this is what the figure shows. North of 35° , where the Ferrel cell operates, we expect the total flux to be smaller than the eddy flux, and again, with just a small discrepancy, our computations show this. Near the pole, north of about 70° , there may be a second direct mean meridional circulation: but this second direct cell, if it exists at all, is very weak and will produce only a negligible heat flux.

The remarkably accurate poleward heat flux given by our heating function, as shown in Figure 18d, must in part be considered coincidental: so good a result obtained from so simple a model must in part be due to a fortuitous cancellation of errors. But though we may doubt that the heating function will be this good in all respects, the results of the test should encourage us to believe that we have a useable first approximation.

When the heating function (88), is used for numerical prediction experiments, it is necessary also that the surface temperature, T_g , be determined. This we will do for the ocean and land areas separately in the following simple way.

For the oceans we will assume in the model an upper layer of water in which there is no vertical temperature gradient and which has no heat exchange with the water below it. For this layer the local change of temperature can be written

$$\frac{\partial T_g}{\partial t} = -\mathbf{v} \cdot \nabla T_g + \frac{S - Q_4}{C_h}, \quad (92)$$

where S is the solar radiation absorbed by the ocean and C_h is the heat capacity of unit column of the upper layer.

We will assume also that in the ocean the advective temperature change is negligibly small and that the heat capacity of unit column is *very large*, so that

$$\frac{\partial T_g}{\partial t} \approx 0,$$

and

$$T_g \equiv (T_g)_{t=0}, \text{ over the ocean.} \quad (93)$$

Over the land we will assume in the model that the temperature changes of the ground are confined to a very shallow layer having a heat capacity which is *negligibly small*. Then

$$C_h \frac{\partial T_g}{\partial t} = S - Q_4 \approx 0, \quad (94)$$

and

$$\begin{aligned} S &= Q_4 \\ &= b(T_g - T_2), \end{aligned} \quad (95)$$

or

$$T_g = \frac{S}{b} + T_2, \text{ over the land.} \quad (96)$$

The constant ocean surface temperature given by (93) approximates the observed condition in the real oceans in which, averaged over 5° latitude-longitude intervals, the local temperature changes are less than a degree centigrade per month.

Over the land, our model is not as good an approximation to real conditions as it is over the oceans. But it does reproduce one of the important features of the real atmosphere, which is that the temperature difference $(T_g - T_2)$ varies latitudinally and seasonally in the same sense as the insolation, S . In low latitudes and in the summer season the temperature lapse rate in the lower part of the atmosphere is large; in high latitudes and in the winter season it is small. This is observed in the real atmosphere only over the lands and not over the oceans: a distinction which is preserved in our model.

It is possible to construct a more refined heating function than the one described, even for a two-parameter model of the atmosphere (cf. Mintz, 1958). One of the modifications that we may experiment with consists of treating the heat of condensation in two parts: a convective condensation which is made a function of the ground-air temperature difference and is part of the heat transfer, Q_4 , as before; and a non-convective condensation which is made a function of the large-scale vertical velocity, ω , by assuming that some predetermined fraction of the air column is saturated wherever the air ascends. (We would not wish, at this stage, to add another parameter to the model in order to carry the history of the water vapor content of the air explicitly.)

We can anticipate a number of important consequences of having the air in the model release latent heat of condensation when it ascends. One result would be the same as if there were an overall reduction in the stability, γ ; namely, a decrease in the wave-length of the disturbances of maximum growth rate. But unlike the effect of an overall reduction in γ , having the air descend dry-adiabatically and ascend with individual temperature changes less than the dry adiabatic will produce an asymmetry in the disturbances that develop, smaller areas of more intense cyclonic development being balanced by larger areas of less intense anti-cyclonic development. But the most important effect of all would be that for the wave-lengths of maximum growth rate a smaller vertical shear would be required for a given rate of growth, and therefore smaller vertical shears (and smaller horizontal temperature gradients) would develop in the model.

IV. FOUR NUMERICAL EXPERIMENTS

We define the *general circulation* as the time-averaged velocity field of the atmosphere as seen in its world-wide distribution*. By the velocity we mean here the vertical velocity, ω , as well as the horizontal velocity, \mathbf{V} , where, as in the previous chapters, these are not physical-point velocities but velocities averaged over horizontal areas of the order of 500 km in diameter.

For the specification of how the time average is to be taken, we define both a "transient general circulation" and a "normal general circulation".

By the *transient general circulation* we mean the velocity field averaged over a time interval which is an order of magnitude larger than the characteristic period of the synoptic-scale atmospheric disturbances. As these disturbances, the ordinary cyclones and anti-cyclones of the weather map, have an average period of about three days, the transient general circulation will be the velocity field averaged for about a month. Thus, the transient general circulation for 15 January 1959 would be the world-wide fields of \mathbf{V} and ω averaged from 1 January to 31 January 1959.

* Some meteorologists use the term "general circulation" for what we call the "mean zonal circulation", or for the "mean meridional circulation" (or for both). Others give still different meanings to the expression "general circulation". It is to avoid ambiguity that we give here our own, perhaps cumbersome but necessary, definitions.

By the *normal general circulation* we mean the transient general circulation of a particular day of the year averaged over a large number of years. Thus, the normal general circulation for 15 January would be the world-wide fields of \mathbf{V} and ω averaged from 1 January to 31 January for many years. In this way we can speak of a normal general circulation for each day of the year.

In addition to the general circulation proper, we can take the zonal average of the general circulation (the average over all longitudes). The zonal average of the west-east (or zonal) component of the time-averaged velocity, \overline{u} , is called the *mean zonal circulation*. The zonal average of either the south-north (or horizontal meridional) component of the time-averaged velocity, \overline{v} , taken alone, or both \overline{v} and $\overline{\omega}$ together (which are related in a simple way by the equation of continuity of mass) is called the *mean meridional circulation*. The mean zonal circulation and the mean meridional circulation are functions of only two of the space coordinates, latitude and elevation, and are usually shown in meridional cross sections.

Finally, we note that we can have a transient or a normal mean zonal circulation, also a transient or a normal mean meridional circulation, with the time-averaging in each case being specified in the same way as for the general circulation proper.

In the pages that follow we will propose four numerical experiments which deal with either the normal general circulation or with the normal mean zonal and mean meridional circulations. In the first experiment the prediction equations (34) and (35) and the heating function (88) are applied to a planet which is entirely land-covered. In the second experiment these equations are applied to a planet which is entirely ocean-covered and in which the initial surface temperature is a function only of latitude. In the third experiment the equations are applied to a planet which is entirely ocean-covered and in which the initial surface temperature is a function of both latitude and longitude. In the fourth experiment the equations are applied to a planet which is partly covered by land and partly by ocean.

1. *The general circulation on a land-covered planet*

On a land-covered planet we have, from (95),

$$Q_4 = S,$$

and from (86),

$$Q = S - Q_0. \quad (97)$$

If we neglect cloudiness and variations of surface albedo, then S is a known function of latitude, φ , and the time of the year, \odot . And if, for the the purpose of a simple experiment, we neglect also the seasonal variation of S , then the net heating per unit atmospheric column, Q , is a function only of latitude, or

$$Q = S(\varphi) - Q_0 = Q(\varphi). \quad (98)$$

Figure 19b shows the mean annual distribution of the net heating, $Q(\varphi)$, as obtained by making $S(\varphi)$ proportional to the mean annual insolation and with its global average $S_m = Q_0 = 28 \times 10^5 \text{ cal m}^{-2} \text{ day}^{-1}$. This, of course, is not exactly the same as the heating computed from the earth-air temperature difference shown in Figure 18c. But they are approximately the same.

Heating which is a function only of latitude was used by N. Phillips (1956) in his remarkable pioneering experiment in the prediction of the normal mean zonal and mean meridional circulations of the atmosphere. Although many meteorologists have contributed greatly to our understanding of the physical processes by which the mean zonal and meridional circulations are maintained, Phillips' experiment was the first successful attempt to *predict* these circulations. It was the first time that the observed circulations were predicted by the direct application of the laws of fluid motion, starting with an atmosphere at rest.

Because we can interpret Phillips' experiment as being the first in the series of four experiments which differ from one another only in the kind of surface on which the

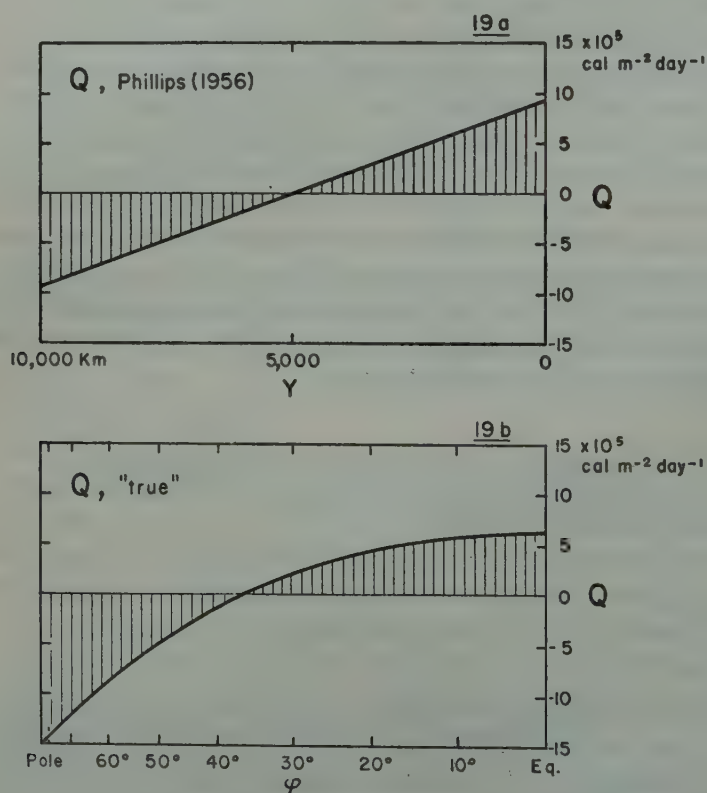


Figure 19

- a) The heating function used by Phillips (1956).
- b) The mean annual heating of the real atmosphere.

atmosphere rests, we will briefly describe some of its features. For details the reader is referred to Phillips' paper.

Phillips considered the motion that would develop in a two-layer model of the atmosphere in a rectangular region bounded by "walls" at the north and south, but open at the western and eastern sides ($x = 0$ and L), with the condition imposed that the flow at $x = 0$ is identical with that at $x = L$ (cyclic continuity). The distance between the north and south walls was taken as 10,000 km (approximately the pole-to-equator distance on the earth). L was taken as 6,000 km. The heating was made a linear function of the south-north coordinate, y . The heating used, in units of cal. per meter square column per day, is shown in Figure 19a.

The dynamical prediction equations were derived by Phillips for a discontinuous two-layer atmosphere rather than for a two-parameter representation of a continuous atmosphere, as in our Section I. However, except for the choice of constants, the resulting prediction equations are the same.

Phillips assumed flow over level ground so that, in terms of our equations (34) and (35), $\bar{p}_s = p_4$ and $\nabla_H \bar{p}_s = 0$. For $C(p)$ he used the equivalent of $C = (p/p_2) - 1$ for $p_2 < p < p_4$, and $C = 0$ for $p < p_2$, so that surface friction operated on \mathbf{v}_3 but had no direct effect on \mathbf{v}_1 . For the equivalent of our K_m he used $0.2 \times 10^{-4} \text{ t m}^{-2} \text{ s}^{-1}$, and $S(\gamma_{3-4}) = S(\gamma_{3-4})_m = 1$. For $\mathbf{v}_s = \mathbf{v}_4$ he assumed a linear extrapolation of the wind from \mathbf{v}_1 and \mathbf{v}_3 , so that in terms of our equation (49), $L = 0.5$ and $M = 0$. The boundary conditions used were $\mathbf{v} = 0$ at the north and south walls. For λ he chose $\lambda_3 = -\lambda_1 = 1.5 \times 10^{-12} \text{ m}^{-2}$. In addition, Phillips used a small-scale lateral eddy diffusion term both for momentum and for heat, with the lateral diffusion coefficients $A_v = A_T = 10^5 \text{ m}^2 \text{ s}^{-1}$. But it is not likely that these played anything but a minor role in determining the form of the motion which developed.

Figures 20, 21 and 22 show the predicted fields of the mean zonal and mean meridional circulations and of the mean temperature (for the 10th to 20th day of the period when disturbances were allowed to develop), together with the mean annual observed fields of these parameters for the real atmosphere.

For the zonal circulation (Figure 20), the prediction given by Phillips' experiment shows in a remarkable way the essential features of the real atmosphere; that is, surface easterlies in the low and high latitudes and surface westerlies in middle latitudes, with a general increase of westerlies with elevation. (The model, in our interpretation, makes no prediction of the temperature above the level p_1 and therefore no prediction of the wind above this level.)

It is clear from the prediction equations that where there are surface easterlies there must be a net divergence in the poleward eddy flux of momentum and where there are surface westerlies there must be a net convergence in the poleward eddy flux of momentum. The numerical values for these flux divergences, at levels 1 and 3, are given by Phillips in his paper.

One noticeable difference between the predicted mean zonal circulation and the observed circulation, shown in Figure 20b (Mintz, 1954), is that the predicted ver-

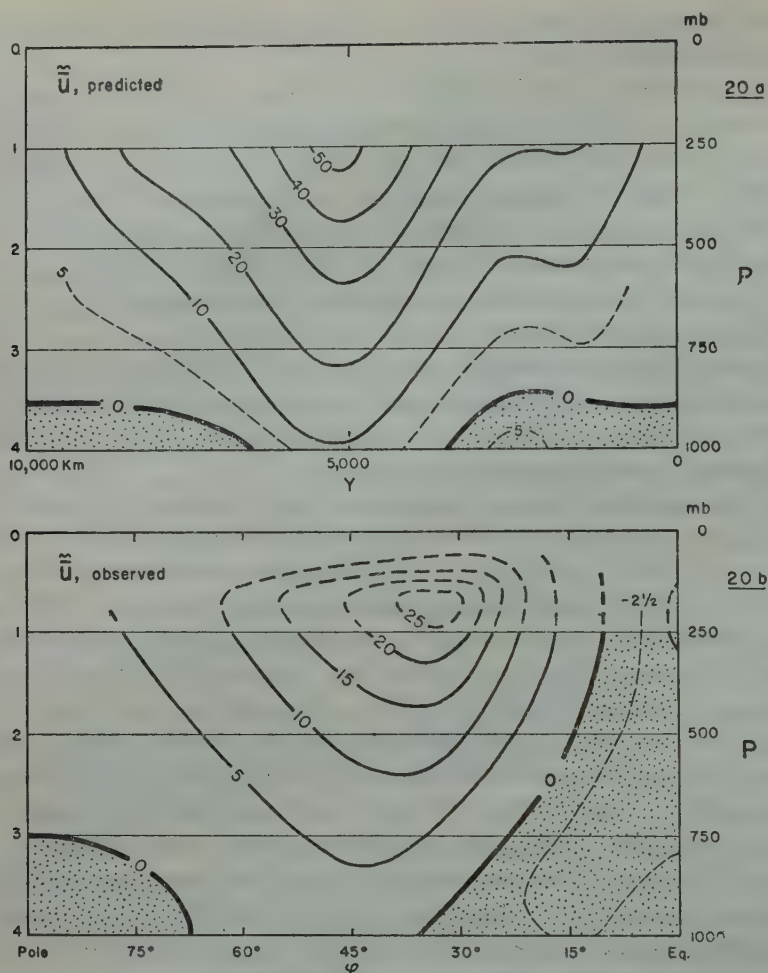


Figure 20

- a) The predicted mean zonal circulation, in m s^{-1} (Phillips, 1956).
 b) The observed mean zonal circulation, in m s^{-1} .

tical shear of the zonal wind, and hence the magnitude of the high level zonal wind, is about twice as large as what is observed. But the large shear that is predicted would presumably be reduced if, as suggested in the last section, the experiment were to be made with a release of latent heat as a function of the computed vertical velocity. The consequent ascent of the air at the individual saturated rate and descent at the unsaturated rate would have the same effect as a large overall reduction of the static stability. It would decrease the vertical shear required for given growth rates, especially in the region of maximum growth rate of the disturbances. Because the equilibrium vertical shear results from the balance between the horizontal gradient of heating and the horizontal flux of heat, which is mainly the eddy flux

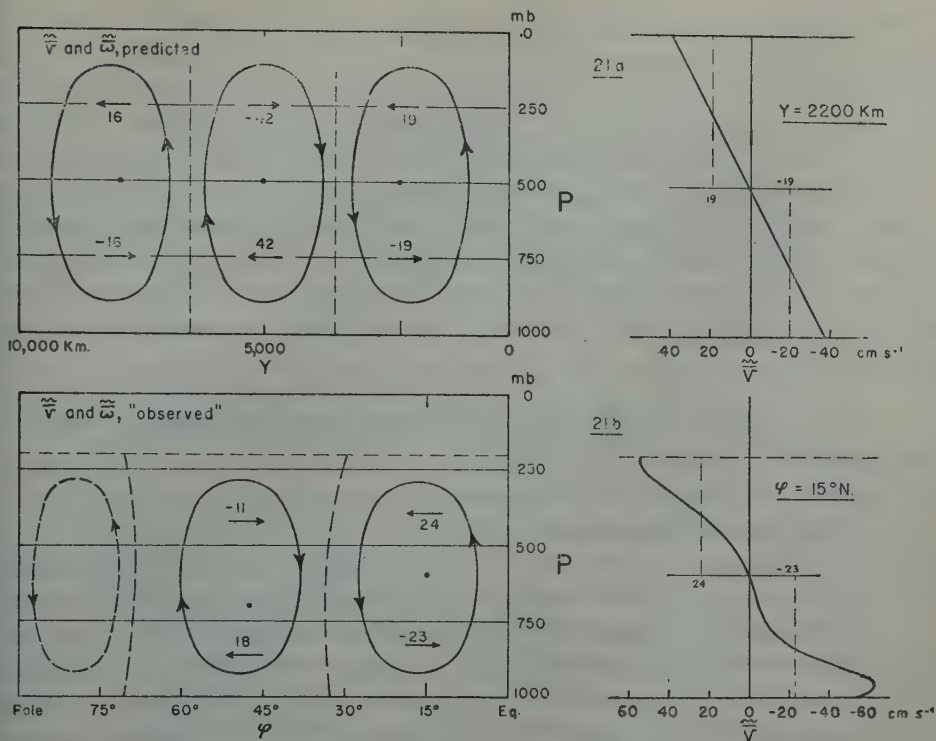


Figure 21

- a) The predicted mean meridional circulation, in cm s^{-1} (Phillips, 1956).
 b) The "observed" mean meridional circulation, in cm s^{-1} .

of heat by the disturbances themselves, there would be a reduction of the predicted vertical shear.

The predicted surface zonal winds, in this experiment, although correct in sign, are also about twice as large in magnitude as the observed surface winds. Very likely the predicted winds would be reduced to about the correct magnitude if, instead of the stress coefficient $K_m = 0.2 \times 10^{-4}$ used by Phillips, $K_m = 0.42 \times 10^{-4}$ were used, this being our empirically determined value of K_m in the absence of large-scale topography.

The remaining discrepancy between the predicted and observed mean zonal circulations is the predicted symmetrical development of the high latitude and low latitude easterlies, especially the fact that the low latitude easterlies do not extend to high levels, as they do in the real atmosphere. There are several possible reasons for this. One is the difference in the geometries of the two systems, rectangular on the one hand and hemispherical on the other. A second reason might be the fact that in the model the flow is set identically equal to zero at the southern wall. (This boundary condition could be overcome by integrating over both northern and southern hemispheres simultaneously, assuming symmetry about the equator.) A third reason

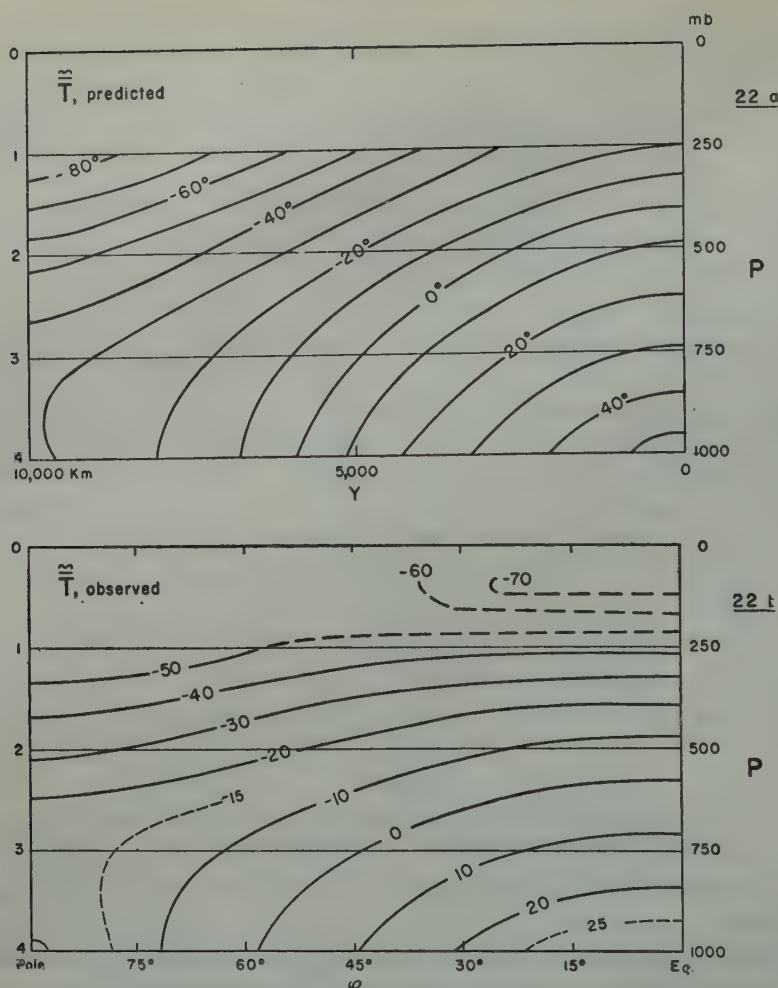


Figure 22

- a) The predicted mean temperature, in °C (Phillips, 1956).
 b) The observed mean temperature, in °C.

for the predicted development of the low latitude easterlies may be the constant Coriolis parameter that is used in the model. A fourth reason, suggested by Phillips, is the neglect of the terms in the vorticity equation which lead to transports of zonal momentum by the horizontal and vertical components of the mean meridional circulation and the vertical eddy transport by the large-scale (computed) vertical velocities of the disturbances. An improvement of the model along these or other lines is needed to obtain a more realistic prediction of the low latitude easterlies.

Figure 21 shows the predicted and "observed" mean meridional circulations. The reason we put quotation marks around the word "observed" is that Figure 21b is

not based on actual observations of the meridional wind but is derived as that meridional circulation which will satisfy the momentum requirements of the real atmosphere under the assumption that we can neglect all scales of vertical eddy stresses above the 700-mb level (Mintz and Lang, 1955).^{*} Having seen that there is fairly good agreement (in pattern and in order of magnitude) between the predicted and observed zonal surface circulations, and hence between the predicted and observed convergences of the poleward momentum flux, we expect to find agreement between the predicted and "observed" meridional circulations. Clearly, in the model as in the real atmosphere, if we assume no frictional forces in the upper levels, then wherever there is divergence in the poleward momentum flux it must be balanced by a positive Coriolis torque ($\overline{\tilde{v}} > 0$), and wherever there is convergence in the poleward momentum flux it must be balanced by a negative Coriolis torque ($\overline{\tilde{v}} < 0$).

In Figures 21a and b, the numerical values show the pressure-averaged values of \tilde{v} for each poleward and equatorward branch of the meridional circulation. We note that in the real atmosphere the intensity of the low latitude direct cell is *greater* than the middle latitude indirect one. This is true because the polar cell plays a negligible role in the real atmosphere and because the Coriolis parameter is small in the tropical latitudes. (As the equations show, the small Coriolis parameter is more important than the greater length of the latitude circles. And integrated from equator to pole the total Coriolis torque must be zero: that is to say, the total transport of momentum from the upper part to the lower part of the atmosphere by these circulations must be zero.)

In the model, however, the Coriolis parameter is the same in all latitudes. In addition, because of the geometry of the system, the contribution of the polar cell to the upward transport of momentum (or one can say, its contribution to the total Coriolis torque) is not negligible, but equal in magnitude to the tropical cell. Both of these reasons operate together to make the intensity of the tropical direct cell *smaller* than that of the indirect cell of the predicted meridional circulation.

On the right hand side of Figure 21 we show the profiles of $\overline{\tilde{v}}$ as a function of pressure for the central latitude of the tropical direct cells. For the predicted circulation, this was obtained from the predicted $\overline{\tilde{v}}_1 = -\overline{\tilde{v}}_3$, given by Phillips, and the

^{*} We may say in support of this usage that where we do have a reliable determination of the mean meridional circulation based on the actual observed winds—in the centre of the tropical direct cell and in the winter season—it is very much like the circulation given by the technique used to construct Figure 21b. The best of the direct determinations is that of Vuorela (1955), and it shows almost exactly the distribution of $\overline{\tilde{v}}$ as that given for the same latitude and season by Mintz and Lang (1955).

The difficulty with using the direct technique to obtain a reliable estimate of $\overline{\tilde{v}}$ in the middle and higher latitudes is that \tilde{v} is ageostrophic; and in these latitudes, unlike the tropics, the ageostrophic component of the observed wind is masked by its much larger geostrophic component.

assumption about the distribution of vertical velocity given in our equation (52). As we have just indicated, the good agreement between the predicted and observed magnitudes of \bar{w} in these tropical direct cells must be attributed to a fortuitous cancellation of errors.

With respect to the temperature field, Phillips shows only the predicted temperature for the 500-mb level. It is a simple matter, however, using the given lapse rate (equation 53), to obtain the complete temperature distribution between p_1 and p_3 . In addition, from (96) and (95), we have

$$T_g = S/b + T_2,$$

and

$$S = Q + Q_0.$$

Using the value of $Q(\varphi)$ given by Phillips, and $Q_0 = 28 \times 10^5 \text{ cal m}^{-2} \text{ day}^{-1}$, we obtain the values of $T_4 \approx T_g$ shown in Figure 22a.

The predicted temperature field agrees with the observed field (Burdecki, 1955) in its general pattern. But the magnitude of the predicted horizontal temperature gradient, as we have already indicated, is about twice as large as that of the observed field. This discrepancy, as we have said, would probably be eliminated by introducing a term into the heating function such that latent heat would be released when the air ascends. This would increase the growth rate of the disturbances, increase the poleward heat flux, and reduce the poleward temperature gradient.

Although there are details that are wrong, the overall remarkable success achieved by Phillips in using the hydrodynamical equations to predict the mean zonal and mean meridional circulations of the atmosphere must be considered one of the landmarks of meteorology.

2. *The mean zonal and mean meridional circulations on an ocean-covered planet, given $T_g(\varphi)$, at $t = 0$*

In our second (and also third) class of experiments we consider the atmosphere to rest upon an earth which is entirely ocean-covered, this ocean having an infinite heat capacity and negligible temperature advection so that the ocean surface temperatures remain constant with time.

For computational purposes we simply maintain each T_g at its initial value. But we can better understand the physical character of these classes of experiments by substituting in

$$Q = b[\Delta T(\lambda, \varphi, t) - (\Delta T)_m]$$

the expressions

$$(\Delta T)_m = T_{g,m} - T_{2,m}$$

and

$$\Delta T(\lambda, \varphi, t) = T_g(\lambda, \varphi) - T_2(\lambda, \varphi, t) = T_g(\lambda, \varphi) - [T_{2,m} + T_2'(\lambda, \varphi, t)], \quad (99)$$

where T_2' is the deviation of T_2 from its mean global value.

Then

$$Q = b[T_g(\lambda,\varphi) - T_{g,m}] - bT_2'(\lambda,\varphi,t). \tag{100}$$

The first term on the right in (100) is a geographically specified *forced heating* and the second term is a *temperature dependent heating*.

As a special case we can take the initial ocean-surface temperature as a function only of latitude. Then we have

$$Q = b[T_g(\varphi) - T_{g,m}] - bT_2'(\lambda,\varphi,t).$$
(101)

Here the forced heating depends only on latitude and the temperature dependent heating varies linearly with the temperature deviations at the level p_2 .

A heating function of precisely this kind (although arrived at by following a quite different line of physical reasoning) has been used by Phillips in a second numerical general circulation experiment. The writer was privileged to be shown some of the first results of this experiment (made on the IBM 704 Computer at the Massachusetts Institute of Technology), but the general and final results have not yet been published by Professor Phillips.

3. *The general circulation on an ocean-covered planet, given $T_g(\lambda, \varphi)$, at $t = 0$*

In the first two classes of experiment described above there is nothing in the heating functions to distinguish one longitude from another. Therefore (unless one introduces a large-scale orography) there is nothing to cause time-averaged variations with longitude, and any time-averaged velocity field which develops must be zonally symmetrical. The first two heating functions, therefore, while adequate for the study of mean zonal and mean meridional circulations of the atmosphere, cannot be used for the study of the general circulation proper.

There is no reason, however, why the ocean surface temperature, T_g , should not be made a function of longitude as well as latitude so that we can use equation (100) in its general form,

$$Q = b[T_g(\lambda,\varphi) - T_{g,m}] - bT_2'(\lambda,\varphi,t).$$
(100)

Each column of the atmosphere is aware that it is in rotation about the local vertical, but it has no way of knowing which way is north and which way is east. The west-east gradients of surface temperature and, as far as we can tell, the west-east gradients of atmospheric heating (cf. Figures 16 and 17) are as large if not larger than the south-north gradients. There is every reason to expect that the model

atmosphere will respond to a forced heating which is a function of longitude by developing a time-averaged velocity field which is not zonally symmetrical but is a true general circulation. That is, it will predict what the old terminology called "centers of action". And, of course, the prediction of a general circulation will implicitly contain the prediction of mean zonal and mean meridional circulations.

A numerical general circulation experiment of this kind, using an ocean-covered planet with the initial surface temperatures varying with longitude as well as latitude, is being carried out by Mr. Avraham Huss, of The Hebrew University of Jerusalem. He is using the WEIZAC Computer, at Rehovot, Israel, for his computations. The results of this experiment should be most interesting.

4. *The general circulation on a planet covered partly by land and partly by ocean*

Finally, we can carry out a general circulation experiment with a planet partly land- and partly ocean-covered.

Over the oceans, in this experiment, the surface temperatures remain constant and equal to their initial values. Here we can take either $T_g = T_g(\varphi)$ or $T_g = T_g(\lambda, \varphi)$ so that the heating is given by either (101) or (100).

Over the land the heating is given by (97), or

$$Q = S(\varphi, \odot) - Q_0,$$

where \odot is the time of the year.

The writer will carry out an experiment of this kind in the near future on the IBM 709 Computer at the University of California, Los Angeles.

Because S varies with \odot , the time-averaged motions that will be of greatest interest to us in this experiment will be those of the transient general circulation. But by averaging over many (annual) cycles, we can obtain a prediction of the normal general circulation.

Assuming that the experiment is successful, it is not at all obvious that in the same phase of each annual cycle the predicted transient general circulations will be approximately the same. This is one of the things we want to learn from this experiment. It may give us some clue to the answer to one of the important questions in meteorology, which is whether the large differences that are observed in the seasonal circulation (and seasonal weather) from year to year in the real atmosphere are due to extra-terrestrial causes or have their origin in the earth-atmosphere system itself.

It is clear, of course, that our experiment may be deficient in the important respect that the ocean, with its great capacity to store heat from one season to another, and even from one year to another, is treated in our model as being inert—in the sense that in our model it is only the atmosphere itself which determines how much heat it will take up from the oceans. We have also neglected other effects which may be important in causing the transient circulation to be different in different years; for example, the variation of albedo, and hence of S , due to variations of cloud- or snow-cover over the land.

But assuming that after developing a hierarchy of models we eventually find one which takes all important effects into account, and gives us in fact a transient general circulation that varies from one cycle to another even with a constant external energy source, the question will remain whether we can use that model to predict, from an observed initial state, the transient general circulation of the real atmosphere.

The answer to this question will depend on whether, in such a self-contained system, the heating which generates the transient general circulation depends upon only the broad scale (and therefore observable) features of the initial state, or whether the heating depends also upon the details (and therefore for all practical purposes the unobservable features) of the initial state. Because the atmosphere is slow in responding to its heating, there is reason to be optimistic and to expect that for a forecast over some large part of an annual period (say a three-month or six-month forecast of the transient general circulation—and also for the forecast of other statistical properties of the velocity field, such as the variability of the wind, the cyclone tracks, and so on) errors in the details of the observed initial state will be of little importance. We can say that with respect to the initial information that is needed (as well as with respect to what is predicted), the transient general circulation bears the same relation to the details of the instantaneous motion as the temperature of a gas bears to the motion of its individual molecules.

A rational, physical method for long-period forecasts of the transient general circulation—that is, for long-range seasonal weather forecasts—is an ambition or dream for the future. But we will never arrive at this goal (or even know whether we *can* arrive) unless we begin with the first steps.

REFERENCES

1. ALISSOW, B. P., DROSDOW, O. A. AND RUBINSTEIN, E. S., 1956, *Lehrbuch der Klimatologie*.
2. BARAD, M. L. AND DAVIDSON, B., 1954, Preliminary report on the relationship between the synoptic weather chart and low level micrometeorological data, *Symposium on Micrometeorology – Turbulent Diffusion, Dugway Proving Ground, 29 June 1954, Report of the Proceedings*, pp. 49–68.
3. BJERKNES, J., 1935, La circulation atmosphérique dans les latitudes sous-tropicales, *Scientia*, February, 1935.
4. BJERKNES, J. AND VENKATESWARAN, S. V., 1957, A model of the general circulation of the tropics in winter, *Large Scale Synoptic Processes, Art. III, Final Report, Univ. of California, Los Angeles, Dept. of Meteorology*, 28 pp.
5. BURDECKI, F., 1955, A study of temperature distribution in the atmosphere, *Notos*, 4, 192–203.
6. DARBYSHIRE, J. AND DARBYSHIRE, M., 1955, Determination of wind stress on the surface of Lough Neagh by measurement of tilt, *Quart. J. Roy. Met. Soc.*, 81, 333–39.
7. DEFANT, A., 1921, Die Zirkulation der Atmosphäre in den Gemäßigten Breiten der Erde, *Geograf. Ann.*, 3, 209–66.
8. ESTOQUE, M., 1957, A graphically integrable prediction model incorporating orographic influences, *J. Met.*, 14, 293–96.
9. GORDON, A. H., 1950, The ratio between observed velocities of the wind at 50 feet and 2000 feet over the North Atlantic Ocean, *Quart. J. Roy. Met. Soc.*, 76, 344–48.
10. HALTINER, G. J. AND HESSE, T. S., 1958, Graphical prognosis including terrain effects, *J. Met.*, 15, 103–07.
11. HANN, J. AND SURING, R., 1939, *Lehrbuch der Meteorologie*, Leipzig.
12. HOUGHTON, H., 1954, On the annual heat balance of the northern hemisphere, *J. Met.*, 11, 1–9.

13. JEFFREYS, H., 1926, On the dynamics of geostrophic winds, *Quart. J. Roy. Met. Soc.*, **52**, 85–104.
14. JEFFREYS, H., 1927, Cyclones and the general circulation, *Quart. J. Roy. Met. Soc.*, **53**, 401–06.
15. JEFFREYS, H., 1933, The function of cyclones in the general circulation, *Procès-verbaux de l'assoc. de météor., Un. Géod. Géophys. Int.*, Lisbon, pp. 219–229.
16. LONDON, J., 1951, Study of the atmospheric heat balance, *Progress Report* 131.06, Research Division, College of Engineering, New York University.
17. MINTZ, Y., 1947, On the kinematics and thermodynamics of the general circulation of the atmosphere in the higher latitudes, *Trans. Am. Geophys. Un.*, **28**, 539–44.
18. MINTZ, Y., 1949, The maintenance of the mean zonal motion of the atmosphere, Doctoral dissertation, *Univ. of California, Los Angeles, Dept. of Meteorology*.
19. MINTZ, Y., 1954, The observed zonal circulation of the atmosphere, *Bull. Amer. Met. Soc.*, **35**, 208–14.
20. MINTZ, Y., 1955a, The zonal-index tendency equation, *Investigations of the General Circulation of the Atmosphere, Final Report, Article III*, *Univ. of California, Los Angeles, Dept. of Meteorology*, 5 pp.
21. MINTZ, Y., 1955b, Final computation of the mean geostrophic poleward flux of angular momentum and of sensible heat in the winter and summer of 1949, *Investigations of the General Circulation of the Atmosphere, Final Report, Article V*, *Univ. of California, Los Angeles, Dept. of Meteorology*, 14 pp.
22. MINTZ, Y., 1956, An empirical determination of the surface drag coefficients for extended-range and long-range numerical weather forecasting and the study of the general circulation (preliminary report), *Scientific Report No. 3, Contract AF 19(604)–1286*, *Univ. of California, Los Angeles, Dept. of Meteorology*, 18 pp.
23. MINTZ, Y. and LANG, J., 1955, A model of the mean meridional circulation, *Investigations of the General Circulation of the Atmosphere, Final Report, Article VI*, *Univ. of California, Los Angeles, Dept. of Meteorology*, 10 pp.
24. MINTZ, Y., 1958, On the incorporation of non-adiabatic effects in numerical integration models for the study of the general circulation, in *The Dynamics of Climate: Proceedings of the General Circulation Conference, Institute for Advanced Study at Princeton, October 1955* (in press).
25. PALMEN, E., 1958, Vertical circulation and release of kinetic energy during the development of hurricane Hazel into an extratropical storm, *Tellus*, **10**, 1–23.
26. PANOFSKY, H. AND CRUTCHER, H. L., 1951, Horizontal momentum flux due to small scale turbulence, *J. Met.*, **8**, 420–21.
27. PHILLIPS, N. A., 1956, The general circulation of the atmosphere: a numerical experiment, *Quart. J. Roy. Met. Soc.*, **82**, 123–64.
28. PHILLIPS, N. A., 1957, A coordinate system having some special advantages for numerical forecasting, *J. Met.*, **14**, 184–85.
29. PRIESTLEY, C. H. B., 1949, Heat transport and zonal stress between latitudes, *Quart. J. Roy. Met. Soc.*, **75**, 28–40.
30. SCHNAPPAUFF, W., 1937, Untersuchungen über die Kalmenzone des Atlantischen Ozeans, *Veröff. Meteor. Inst. Univ. Berlin*, **2** (4), 1–35.
31. SHEPPARD, P. A., 1949, Large scale vertical motion in the atmosphere: discussion of recent research at Imperial College, *Quart. J. Roy. Met. Soc.*, **75**, 188–95.
32. SIMPSON, G. C., 1929, The distribution of terrestrial radiation, *Mem. Roy. Met. Soc.*, **3** (23), 53–78.
33. STARR, V. P. AND WHITE, R. M., 1952, Note on the seasonal variation of the meridional flux of angular momentum, *Quart. J. Roy. Met. Soc.*, **78**, 62–69.
34. STARR, V. P. AND WHITE, R. M., 1954, Balance requirements of the general circulation, *Geophysics Research Papers*, No. 35, 57 pp.
35. SVERDRUP, H. U., 1942, *Oceanography for Meteorologists*, Prentice-Hall, New York, 235 pp.
36. VUORELA, L. A., 1955, On the observed zonal and meridional circulations at latitudes 15°N and 30°N in winter, *Geophysica* (Helsinki), **6** (2), 106–20.
37. WHITE, R. M., 1949, The role of mountains in the angular-momentum balance of the atmosphere, *J. Met.*, **6**, 353–55.
38. WIDGER, W. K., 1949, A study of the flow of angular momentum in the atmosphere, *J. Met.*, **6**, 291–99.

STUDIES OF THE EFFECT OF SALINE IRRIGATION WATER ON CALCAREOUS SOILS. II. THE BEHAVIOUR OF CALCIUM CARBONATE

DAN H. YAALON

The Hebrew University of Jerusalem

ABSTRACT

The presence of CaCO_3 has often been considered to be a sufficient guarantee for prevention of sodium adsorption by clay from saline irrigation water. A scrutiny of the behaviour of CaCO_3 at conditions prevailing in the soil environment was undertaken to test this concept.

It is shown that the physico-chemical equilibria of the soil- CaCO_3 system are analogous to the equilibria of the pure CaCO_3 system. Because of its effect on the pH of the saturated solution, there too carbon dioxide pressure of the gaseous phase is the most important variable affecting the solubility of CaCO_3 . Exchangeable ions of the clay exert an influence similar to that of dissociated salts.

It is concluded that under conditions prevailing in the soil during percolation, the solubility of CaCO_3 is too low to supply sufficient Ca^{++} -ions to the soil solution and thus unable to prevent the adsorption of sodium. Only in the case of very dilute saline solutions is solid CaCO_3 able to supply sufficient Ca^{++} -ions to the percolating water in order to alter the undesirable $\text{Na}^+/\text{Ca}^{++}$ ratio. The effect of flow rates on dissolution is considered.

Since gypsum, on the other hand, is sufficiently soluble to prevent the adsorption of sodium from moderately saline waters, it is suggested that it be applied as a preventive soil conditioner on all soil where permanent irrigation with more or less saline water is established. In order to prevent the dispersion of the clay and to keep the highest possible concentration of calcium ions during leaching with salt-free water, it is suggested that gypsum be supplied regularly before the winter rains.

INTRODUCTION

During percolation of saline water through soils, exchange reactions take place between the exchangeable ions of the solid clay phase and the electrolytes of the liquid phase, until an equilibrium between the solid and liquid phases is established. If slightly soluble salts are present in the soil, they perpetually supply to the percolating soil solution additional ions and thus continuously affect the adsorption equilibrium. The exchange reactions taking place in calcareous soils during percolation with saline irrigation water belong to this special case and will be discussed in the present paper.

The questions asked are: What amount of calcium carbonate can the soil solution dissolve, and is this sufficient to prevent the adsorption of sodium by the clay? How

Received June 10, 1957.

does it affect soil pH and other soil properties? What practical conclusions can be drawn? The answer must necessarily be based on the elucidation of the solubility relationships of calcium carbonate under the various environmental conditions of calcareous soils, and an integration of its capacity to supply calcium ions to the soil solution with the laws of ion exchange.

SOLUBILITY AND INTERACTION OF CALCIUM CARBONATE IN THE SOIL ENVIRONMENT

Applying the law of mass action, various workers have shown that in aqueous solutions in contact with solid CaCO_3 definite relationships are established between atmospheric CO_2 pressure, pH, and ionic strength of the solution (e.g. Bjerrum and Gjaldbaek 1919). Based on a systematic theoretical analysis and incorporating available experimental data, several equations and equilibrium constants have been derived, showing the effect of all relevant variables on the solubility (Yaalon 1954 and 1957).

The system $\text{CaCO}_3\text{--CO}_2\text{--H}_2\text{O}$ at different pH values

In an invariant system the solubility of CaCO_3 increases logarithmically with decreasing pH and is proportional to the cube root of CO_2 pressure. By combining the effect of these variables and the effect of the ionic strength, an overall equilibrium equation (at 25°C) is obtained,

$$2\text{pH} + \log [\text{Ca}^{++}] + \log P_{\text{CO}_2} = 9.85 + f(\mu) \quad (1)$$

where $[\text{Ca}^{++}]$ is the molar concentration of calcium and $f(\mu)$ is some function of the ionic strength of the solution. A satisfactory approximation of the theoretical Debye-Hueckel function is given by the expression $1.7 \sqrt{\mu}$, derived graphically by plotting ionic strength against the apparent equilibrium constant.

The relation is presented in the solubility curve of Figure 1, demonstrating that CaCO_3 solubility and pH of the resulting solution are determined by the CO_2 pressure of the gaseous phase. At the normal CO_2 content of atmospheric air the solubility is only 0.6 mM per litre and the resulting pH of the solution is 8.31.

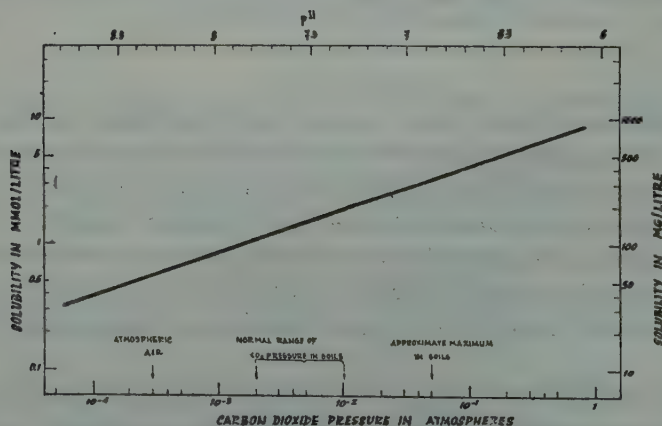


Figure 1

Solubility of calcium carbonate as a function of pH and carbon dioxide pressure (25°C)

Effect of neutral salts. In dilute solutions up to ionic strength of 0.01, increase in solubility is for all practical purposes a linear function of $\sqrt{\mu}$ resulting from increments of neutral salts. At higher concentrations the relation is curvilinear. Generally the increase in solubility is accompanied by a slight decrease in the pH of the saturated solution. At the concentration of electrolytes and at the carbon dioxide pressure likely to occur in soils, the increase in solubility is slight and will not be over 1 mM per litre.

Effect of a common ion. A salt with a common ion decreases the solubility of CaCO_3 , but on the other hand, if the common ion is Ca^{++} , it permits a much higher total calcium concentration in the solution. This in turn is limited only by the solubility product of the more soluble salt. Hence, if CaSO_4 is also present in the soil the calcium-ion concentration can reach a value of about 30 mEq per litre, and is practically unlimited if the salt is CaCl_2 .

When considering the interaction of calcium carbonate with the clay minerals of a soil, the important variables affecting it are (1) the carbon dioxide content of the soil atmosphere, (2) the ionic composition and strength of the soil solution, and (3) the exchangeable ions of the clay complex. The effect of these variables will be examined in the following.

The effect of carbon dioxide

The effects of variations in carbon dioxide pressure on CaCO_3 solubility are large in comparison with other factors.

Though at constant pH an increase in carbon dioxide pressure causes a decrease in solubility (cf. equation 1), when pH is permitted to adjust itself, higher pressure of CO_2 is accompanied by a decrease in pH (cf. equation 3 below), with an overall effect of enhanced CaCO_3 solubility. Thus

$$\log [\text{Ca}^{++}] = 1/3 \log P_{\text{CO}_2} - 1.95 + f(\mu) \quad (2)$$

The constants of equations 1 and 2 are the product of the equilibrium constants of the participating simultaneous equilibria, and have been calculated for 25°C (Yaalon 1954), using the best available thermodynamic constants. Figure 1 shows graphically also this relationship.

Consequently, the carbon dioxide content of the soil atmosphere must be regarded as one of the important variables affecting the capacity of CaCO_3 to release Ca^{++} -ions to the soil solution. The range of its concentration in the soil atmosphere is a function of biological activity and is therefore much wider and higher than that of the air above the soil. It is known to vary between the concentration of the atmospheric air, 0.03%, and up to 5–10% (Russel 1950, p. 339). Not many exact determinations of CO_2 content in irrigated arid soils are available, but assuming it to be somewhat lower than in humid soils, its normal range can be tentatively set to be between 0.2–1.0%, higher values being applicable for tropical soils with considerable microbiological activity. At this range of CO_2 pressure, the solubility of CaCO_3 reaches 1.0–1.9 mM per litre and imparts to the solution a pH of 7.3–7.8, which is the normal range of pH in calcareous soils under field conditions (Figure 1).

The pH of a CaCO_3 solution in equilibrium with atmospheric air ($P_{\text{CO}_2} = 0.00032$ atm) is 8.31 at 25°C, which should therefore also be the pH of calcareous soils aerated with atmospheric air of normal composition. Usually it is found to be somewhat higher, but does not exceed 8.5 (Bradfield and Allison 1933). This might be due to the inherent colloidal properties of the clay, but is generally ascribed to the presence of exchangeable monovalent bases, usually sodium. Also MgCO_3 , which is more soluble than CaCO_3 and yields a higher pH at similar CO_2 pressure (Gjaldbaek 1921), will contribute to this effect.

The effect of carbon dioxide on the soil reaction of calcareous soils has been investigated by Whitney and Gardner (1943). The curve showing the effect of partial CO_2 pressure on pH was found to follow the same logarithmic shape as for pure carbonates. The average regression for the 18 soils tested has been calculated by the present author and results in the following equation:

$$\text{pH} = -0.65 \log P_{\text{CO}_2} + 6.00 \quad (25^\circ\text{C}) \quad (3)$$

The constants are practically identical with those obtained for pure calcium carbonate, which are $-2/3$ and $5.90 + f(\mu)$ respectively. A more careful scrutiny of Whitney and Gardner's data reveals slightly different functions for three different types of soils (Yaalon 1957).

This, in addition to evidence obtained recently by Turner and Clark (1956) and Cole (1957), enables us to conclude that the effect of carbon dioxide on CaCO_3 solubility in calcareous soils is analogous to its effect on the pure salt, and can be deduced with sufficient accuracy from theory.

The effect of the soil solution

The concentration of the soil solution, defined as the solution existing at a soil moisture content within the field range and containing the salts of unadsorbed anions, varies inversely with the amount of moisture present in the soil. The change in total concentration is accompanied by a shift in the relative concentration and distribution of the different ions, mainly as a result of different absorbing powers of the exchangeable cations in the ionic double layer of the soil phase (Reitemeier 1946). Consequently there exists no static boundary between the adsorbed ions in the solid phase and those in the soil solution.

The soil solution of a leached agricultural soil under normal conditions of moisture contains up to 500 ppm of soluble matter (Russek 1950, p. 438). Reckoning with the normal composition of the common ions, this becomes equivalent to about 7 mEq/litre with an ionic strength of $\mu = 0.01$ and osmotic pressure of 0.25 atm. Hence the soil solution in such a soil is very dilute, even at low moisture content.

In soils of arid regions, because of the occurrence of slightly soluble salts and minerals and because of retarded leaching, the concentration is usually several times higher. In calcareous soils the concentration is about 1000–5000 ppm and can be much higher in calcareous-saline soils. Reckoning with the above range, we obtain an ionic strength of $\mu = 0.04$ –0.15 ($\sqrt{\mu} = 0.2$ –0.4) (expressed in equivalents 20–100 mEq/litre), and an osmotic concentration of 1–4 atm. The solubility of CaCO_3 at this range of ionic strength and normal CO_2 pressure is 4–5 mEq/l. and the pH of its solution 7.2–7.7. But if due to the presence of Na^+ -clay the pH of the soil rises above 8.0, and carbon dioxide pressure is decreased as a result of reduced biological activity and air exchange, then the solubility of CaCO_3 is less than 2 mEq/l.

The analytical results of Ca^{++} concentration in the soil solution of the permeability experiments reported in Part I of this study (Yaalon 1955) agree well with the above considerations, as do also concentrations of soil solutions at field moisture and saturation percentage as determined by Reitemeier (1946). For calcareous soils not containing gypsum, the concentration of soluble calcium was within the limits discussed above. Where Na_2CO_3 was present, and the pH was high, the concentration of calcium was considerably lower, while CaSO_4 was able to keep the concentration of calcium at a level of about 25 mEq/litre.

The effect of exchangeable ions

The most important variable affecting the behaviour of CaCO_3 in the soil is the exchange complex of its clay minerals. The calcium dissolved from the calcium carbonate may be exchanged for other cations:



Thus the solubility equilibrium of the CaCO_3 -soil solution system (equation 1 and 2) is affected by the additional equilibrium with the clay mineral (equation 4). Hydrogen, calcium and sodium can typify the main types of exchangeable ions encountered in the soil, and their effect on the behaviour of CaCO_3 will be considered.

If hydrogen is the exchangeable ion of the clay, the acid soil will cause the decomposition of the CaCO_3 with a resulting neutralisation of the clay, a reaction utilised in the liming of acid soils in humid areas. The solid of CaCO_3 constitutes a reserve of calcium ions, which will tend to keep the clay saturated with bases and maintain a constant pH. The level of the pH will depend solely on the carbon dioxide pressure and on the electrolyte concentration of the soil solution. Only when all CaCO_3 has been dissolved will there exist the possibility that the pH decreases, since the buffer capacity of the bicarbonate system is rather small.

Ca^{++} -clay will interact in a manner similar to that of an ordinary ionised Ca^{++} -salt at the same Ca^{++} -ion activity. A "titration" curve of CaCO_3 with increasing amounts of Ca^{++} -clay is presented in Figure 2. The data were obtained at constant P_{CO_2} of 0.00032 atm (by aeration) and at 25°C. It can be seen that the effect of exchangeable Ca^{++} on the pH and solubility is very small, which is in agreement with Marshall's determinations of the active fraction (Marshall 1950). For a Ca^{++} -clay an activity coefficient of not more than 0.09 was obtained, kaolinite having the highest value.

As exchange reactions between Na^+ and Ca^{++} will take place when Na^+ -clay is added to a CaCO_3 solution, it cannot be a priori expected that the Na^+ -clay will behave similarly to a dissociated neutral Na^+ -salt. Because of its alkaline reaction, sodium clay will also effect solubility differently

than a neutral Na^+ -salt. A "titration" of CaCO_3 with Na^+ -clay, analogous to Figure 2, is presented in Figure 3. It can be seen that increasing amounts of Na^+ -clay increase the pH of the resulting equilibrium solution, the extent of the increase depending on the CO_2 pressure. Also, in agreement with the effect of pH on solubility of the pure salt, the calcium ion concentration in the solution decreased. Similar curves have been obtained by Puri and Puri (1938).

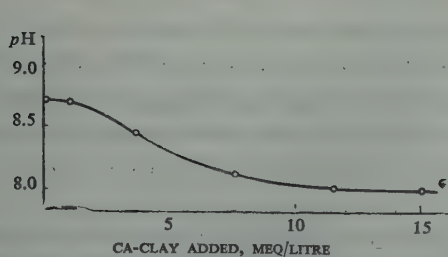


Figure 2
pH of a saturated CaCO_3 solution as a function of added Ca-clay (at CO_2 pressure of atmospheric air)

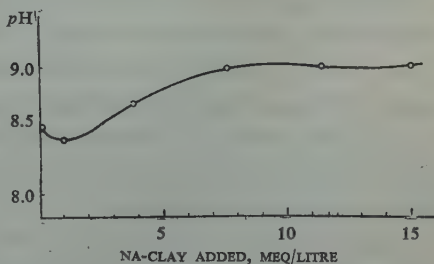


Figure 3
pH of a saturated CaCO_3 solution as a function of added Na-clay (at CO_2 pressure of atmospheric air)

In conclusion, it can be said that the physico-chemical equilibria of the CaCO_3 system are not appreciably affected by the presence of soil minerals, and hence that the laws governing these equilibria are directly applicable to the soil CaCO_3 system. Collaterally it is possible to interpret observed soil phenomena in terms of solubility, pH and ionic strength.

THE BEHAVIOUR OF CALCIUM CARBONATE DURING PERCOLATION

The preceding chapter has demonstrated that under the environmental conditions prevalent in calcareous soils the solubility of CaCO_3 is low, and that even under relatively favourable conditions it would reach only about 5 mEq Ca^{++} per litre. CaCO_3 is thus ordinarily unable to supply sufficient calcium ions to a saline solution to alter materially an unfavourable proportion of $\text{Na}^+/\text{Ca}^{++}$. Normal exchange reactions between the percolating liquid and the exchangeable ion will lead to a gradual saturation of the exchange complex with sodium, which may eventually attain an undesirable level of saturation (Yaalon 1955).

Having derived the amount of CaCO_3 carried in the soil solution in equilibrium with a given environment, there remains to consider the rate at which this equilibrium concentration is attained.

The rate of dissolution of a solid is related to its solubility; the greater the solubility, the higher the rate of solution. Of the many variables affecting and controlling the rate, the more important ones are: (1) the exposed surface and structure of the solid, (2) the rate of diffusion of the dissolving ions, which in turn is a function of the concentration gradient and the ionic mobility, and (3) the state of motion of the dissolving liquid.

Consider a granule of CaCO_3 embedded in a column of soil through which water is percolated. The percolating liquid removes dissolved ions from the vicinity of the granule as long as a saturation deficit exists. The maximum rate of dissolution is encountered at high rates of flow with solutions possessing a high capacity to hold calcium. When the percolation rate decreases—in soils primarily due to the

swelling and dispersion of clay—the rate of dissolution decreases for two reasons. As the rate of removal of the solution film surrounding the calcium carbonate decreases, the concentration gradient is gradually reduced, with a consequent decrease in the diffusion rate of the ions. Also, as a result of ion exchange and hydrolysis, the capacity to hold calcium is further decreased.

Permeability characteristics of the soils reported in Part I of this study (Yaalon 1955) agree well with these considerations. In all cases where permeability has been reduced by the swelling of the clay, the resulting slower rate of flow, the water being forced to flow through narrower and more twisted channels, has reduced the rate of dissolution of CaCO_3 to such an extent that it has become ineffective as supplier of calcium ions to the solution.

Information on the amount of CaCO_3 dissolving during percolation with saline solutions was obtained from the following experiment. NaCl solutions were percolated through a 10 cm deep bed of precipitated CaCO_3 ($< 1\mu$) and washed quartz sand (0.05–0.1mm), thoroughly mixed at the weight ratio of 1:2. The calcium ion concentration and pH of the percolate were determined. In Table I the concentrations reached during steady flow are compared to the concentration of the percolating solution used. Considering these values as the limiting values of Ca^{++} concentration in the soil solution, it is evident that only where the percolating solution is very weak will sufficient calcium carbonate dissolve to alter its undesirable ratio of $\text{N}^+/\text{Ca}^{++}$. A solution containing 6 mEq Na^+ and 3 mEq Ca^{++} per litre (67% Na^+) was percolated through the CaCO_3 sand bed and passed through practically unaltered.

TABLE I

Effect of percolating solution on composition of leachate

Medium: Precipitated CaCO_3 mixed with quartz sand (0.05–0.1 mm) at weight ratio 1:2
Percolating fluid: NaCl solution. Room temperature and P_{CO_2} of atmospheric air

Concentration of percolating solution NaCl (mEq/l.)	Composition of leachate at steady flow conditions		Equivalent Na^+ percentage of leachate*
	Ca^{++} (mEq/l.)	pH	
0	0.85	8.70	—
1	1.18	8.45	46
2	1.03	8.65	66
5	0.97	8.90	84
10	0.98	9.10	91

* Ionic strength ($\sqrt{\mu}$) of leachate is about 0.12–0.16

PRACTICAL IMPLICATIONS

To prevent the adsorption of sodium from irrigation water with an undesirable $\text{Na}^+/\text{Ca}^{++}$ ratio, a considerable increase in the calcium ion concentration of the soil solution must be obtained. The logical conclusion for calcareous soils would be to try to increase the solubility of the lime present, which after all presents an almost inexhaustible resource of calcium.

Since carbon dioxide is the most important factor enhancing lime solubility, soil management and irrigation practice must aim to fulfill this requisite. Improved aeration in itself will not increase the carbon dioxide content of the soil atmosphere unless it is accompanied by increased microbiological activity or respiration of the root system. Hence plants with an extensive root system are preferred, and a periodic addition of organic manure should be beneficial. Also, the evidence that drying of the soil improves permeability should be examined in this light.

Should the above measures not suffice, and a decrease in permeability be observed, then means of increasing the calcium-ion concentration by a suitable external addition must be considered.

Gypsum is many times more soluble than CaCO_3 and is able to supply about 25–30 mEq Ca^{++} ions per litre. Its capacity to alter the composition of the liquid phase is therefore considerable. Its solubility relationships in soils have been studied by Vanoni and Conrad (1942) and found to be explicable in terms of solubility product and ionic strength phenomena. It fulfills all requirements of a suitable amendment, and can be added either to the irrigation water or directly to the soil.

It seems to the writer that in arid and semi-arid irrigated agriculture, gypsum application should take the place of liming in humid climates, and that it should be introduced as a regular feature in soil management, especially where a permanent system of irrigation agriculture has been established and water of more or less doubtful quality is being used.

It is probable that better results will be obtained with smaller and more frequent additions. An application prior to a change in the composition of the water—this includes the effect of salt-free winter rains—should be beneficial and enable the establishment of a calcium ion concentration at a sufficiently high level to keep the soil colloids in a flocculated and permeable condition.

ACKNOWLEDGEMENT

The author wishes to record his indebtedness to the late Prof. A. Reifenberg for his continuous interest and encouragement in these studies, and to Dr. M. Rim for constructive and helpful criticism of the manuscript.

REFERENCES

1. BJERRUM, N., AND GJALDBAEK, J. K., 1919, Investigation of the factors which determine the reaction of the soils. I and II, *Kgl. Vet. Landboh. Aarskrift*, 48–91.
2. BRADFIELD, R., 1942, Ca in the soil. I. Physico-chemical relationships, *Proc. Soil Sci. Soc. Amer.*, 6, 8–15.
3. BRADFIELD, R. AND ALLISON, W. B., 1933, Criteria of base saturation in soils, *Trans. 2nd Comm. Intern. Soc. Soil Sci., Copenhagen, A*, 63–79.
4. COLE, C. V., 1957, Hydrogen and calcium relationships of calcareous soils, *Soil Sci.*, 83, 141–150.
5. GJALDBAEK, J. K., 1921, Investigation on the factors which determine the reaction of the soil. III. MgCO_3 , *Kgl. Vet. Landboh. Aarskrift*, 245–296.
6. MARSHALL, C. E., 1950, The electrochemistry of clay minerals in relation to pedology, *Trans. 4th Int. Cong. Soil Sci., Amsterdam*, 2, 71–82.
7. PURI, A. N. AND PURI, M. L., 1938, Interaction between carbonates and soils, *Soil Sci.*, 46, 401–408.
8. REITEMEIER, R. F., 1946, Effect of moisture content on the dissolved and exchangeable ion of soils of arid regions, *Soil Sci.*, 61, 195–214.
9. RUSSEL, E. J. AND RUSSEL, E. W., 1950, *Soil Conditions and Plant Growth*, 8th ed., Longmans Green, London, 635 pp.
10. SIMMONS, C. F., 1939, The effect of carbon dioxide pressure upon equilibrium of the system hydrogen-colloidal clay- $\text{H}_2\text{O}-\text{CaCO}_3$, *J. Am. Soc. Agron.*, 31, 638–648.
11. TOVBORG-JENSEN, S., 1936, Kalkens omsaetninger i jordbunden, teoretisk og eksperimentelt belyst, *Tids. f. Planteavl*, 41, 571–649.

12. TURNER, R. C. AND CLARK, J. S., 1956, The pH of calcareous soils, *Soil Sci.*, **82**, 337-341.
13. VANONI, I. E. AND CONRAD, J. P., 1942, Calcium and sulfate ion concentration in a soil receiving excess gypsum, as influenced by several factors, *Soil Sci.*, **53**, 125-133.
14. WHITNEY, R. S. AND GARDNER, R., 1943, The effect of carbon dioxide on soil reaction, *Soil Sci.*, **55**, 127-141.
15. YAALON, D. H., 1954, Physico-chemical relationships of CaCO_3 , pH and CO_2 in calcareous soils, *Trans. 5th Intern. Cong. Soil Sci.*, **2**, 356-363.
16. YAALON, D. H., 1955, Studies of the effect of saline irrigation water on soils. I. Permeability characteristics and adsorption of sodium, *Bull. Res. Counc. of Israel*, **5B**, 83-97.
17. YAALON, D. H., 1957, Problems of soil testing on calcareous soils, *Plant and Soil*, **8**, 275-288.

SIMULATION, BY DYNAMICAL MODEL, OF SAND TRACT MORPHOLOGIES OCCURRING IN ISRAEL

M. RIM

The Hebrew University of Jerusalem

ABSTRACT

The question of which configuration is attained (and maintained) by the surface of a bed of loose sediment when it is subjected to the erosive and simultaneously depositional action of a sediment-carrying stream is studied with the aid of a hydraulic flume. The experimental results obtained for this particular system have significance also for analogous systems (where the fluid may be a fluid other than water) if a certain relationship exists between the scales for geometrical dimensions, velocities, forces, specific gravities, viscosities, etc., in the experimental system (model specimen) and the corresponding scales in the analogous system (prototype specimen). This relationship between the scales is defined here in a non-rigorous manner (by three "Prerequisites of Dynamical Analogy") which makes it applicable to geomorphological and geological problems.

On the basis of these Prerequisites the flume experiments and the miniature landscapes created in the flume under the water current are postulated to be dynamically analogous to large-scale landscapes formed by wind—which analogy is then proven to be real by actual comparisons. Thus it becomes possible to study the mechanism of geomorphological evolution and the relative importance and interdependence of the factors involved on a dynamical model instead of on a full-size dynamical prototype, which latter would usually be impracticable. Here such a study of a collection of dynamical prototypes, the typical sand tract morphologies occurring in Israel, is reported.

Dynamical model studies of fossil landscapes could also contribute to the identification of wind regimes and environmental conditions of past periods.

THE PREREQUISITES OF DYNAMICAL ANALOGY

Dynamical models are functioning models in which, besides geometrical proportions, the time scales and mass scales (and thereby the inertia and force units) also bear a fixed relationship to the imitated system, which is then referred to as the prototype. Designers of machinery and structures involving relative motions of fluids and solids (such as missiles, airplanes, ships, river channels, wave- and wind-breakers, etc.) depend fully on dynamical modelling, and it is also a dependable tool in geophysical investigations that deal with problems concerning atmospheric or oceanic currents. As long as the fluid involved is of the "Newtonian fluid" kind, and as long as the confinements are not deformable by the fluid's motion, the correspondence between a dynamical model and its prototype is mathematically rigorously definable by the "criteria of dynamical similitude".*

* A set of formulae that are derived by "dimensional analysis" of the relative parameters and which shall make it possible to predict, for instance, whether a half-size model airplane of say one-tenth the weight of the full-size prototype will lift itself off the ground at one-half of, the same as, or twice the prototype's runway velocity.

Received July 18, 1955.

Geomorphological prototypes, on the other hand, present mathematical difficulties because they do not fulfill the two above-mentioned conditions. Firstly, the fluids involved, which in geomorphological prototypes naturally are always carrying sediments, no longer display "Newtonian" behaviour. Secondly, geomorphological systems deform their confining boundaries by erosion and deposition.

Thus it is clear that some of the mathematical rigour of the criteria of dynamical similitude must be sacrificed when interpreting analogies in geomorphology.*

For the task confronting the author in the work reported here it was sufficient to simplify the rules of dynamical analogy and reformulate them as "General Prerequisites of Dynamical Analogy in Eroding and Depositing Systems" which state the conditions that must be fulfilled if the functioning of a prototype is to be re-enacted on different time-, size-, and mass-scales.

Prerequisite 1

When a bed of loose sediment is exposed to the action of a fluid flowing over it, the equilibrium between erosion and redeposition will lead to a steady (not static) state of configuration of the bed surface. The height of the relief of the bed surface, usually a pattern of undulations and knolls, is then commensurate with the height of what will be termed here "sediment atmosphere," namely the churned-up sediment cloud that consists of the fluid-carried portion of the sediment (suspended, saltating or otherwise moving) and blankets the solid sediment bed. There is a fixed relationship between relief and atmosphere heights in dynamically comparable systems; in other words, if R_1 and R_2 denote the relief heights in two systems and A_1 and A_2 correspondingly the atmosphere heights in these systems, then $R_1/R_2 \approx A_1/A_2$, irrespective of fluid velocities.

Prerequisite 2

Since the sediment atmosphere is isotropically turbulent except nearest to the sediment bed, it determines the horizontal dimensions, i.e. the dimensions of the plan projection of the sediment-bed surficial features, in such a way that $A_1/A_2 \approx L_1/L_2$, where L stands for corresponding distances between markers on the bed surfaces. For the lateral distances between any other markers, $L', L'', L''', \dots L^{(n)}, \dots$, the same relationship holds, of course. Consequently,

$$L'_1 : L'_2 : L'_3 : \dots : L'_n : \dots \approx L''_1 : L''_2 : L''_3 : \dots : L''_n : \dots,$$

i.e. there ought to be full geometric similarity between dynamically similar systems. Conversely, full geometric similarity between the surficial patterns formed in two systems is a weighty argument, though not a fully conclusive one, in favour of the assumption that these two systems are functioning dynamically analogously.

* It is possible to conceive of the confining sediment bed not as deformable walls and floor, but as the multitude of rigid grains it really is, and to treat the fluid not as a sediment-carrying non-Newtonian mixture but as a clear Newtonian fluid that surrounds each suspended grain. This approach leaves the problem in principle a rigorously solvable one, but the solution would be impractically complicated.

Prerequisite 3

In the case of non-steady multi-directional fluid flow, the "resultant" flow vector does not necessarily coincide with the "resultant" vector of sediment drift. The latter depends on a host of environmental factors, particularly on local differences of sediment configuration and abundance. For two systems to function as dynamical analogs it is necessary that the lateral distribution of sediment drift be similar in both systems. Conversely, similar drift distribution in two systems may indicate analogy of dynamical functioning in other respects.

Additional Prerequisites and Simplifications

If the systems contained sediments other than completely loose sand, it would have been necessary to add here prerequisites concerning the relative scales of the cohesion forces in the compared systems. This problem is too complicated and therefore all modelling studies so far have been confined to modelling eolian sand tract morphologies. A prior dynamical model study of eolian sand landscapes by hydraulic flume (a study of the Sahara desert sand dune morphologies) had been completed with the aid of similar experimental aids by L. Escande (1950, 1951). Escande's prototypes were selected as the most simple (or assumedly simple) existing systems: he took for granted in his prototypes that winds were unidirectional and that sand was omnipresent. These assumptions eliminated the problems connected with Prerequisite 3 and made it possible for him to apply formally, without modification, the mathematical criteria based on dimensional analysis. By means of these criteria Escande was the first to show that sub-aerial sand landscapes must be modelled dynamically not by miniature sand landscapes formed in *wind* tunnels, but by those formed under flowing *water*. This is what is expressed implicitly in the first of the above prerequisites.

METHOD AND RESULTS OF EXPERIMENTATION

The hydraulic flume in which the dynamical model experiments were carried out consisted of a 10 m long channel of square cross section (0.35×0.35 m) and a pipe fitted underneath through which the fluid was continuously pumped from the channel tail end back to the channel head (Figure 1).^{*} The channel floor was completely covered with fine sand, forming the sediment bed. The surface of the bed attained and maintained specific shapes when water was made to flow through the flume channel.

The variables were the kind of sediment, sediment distribution and current velocity. Only one kind of sediment was used in the series of experiments reported here, namely, fine sand consisting of well-rounded quartz grains of uniform size (sieved and winnowed by means of a specially constructed machine which removed all grains that were larger than 0.14 mm or smaller than 0.11 mm in diameter, or deviated

^{*} This flume was built for sediment traction studies by the U.S. Soil Conservation Service, at the Sedimentation Laboratory of the California Institute of Technology. The author thanks Professor V. A. Vanoni for the permission to use this flume, and for the help and instruction received

too much from spherical shape or average specific gravity). Local sediment distribution in the flume was influenced (in a manner described in detail further on) by placing "false bottoms" into the channel. Water-current velocity was regulated to the desired values by inclining the whole channel lengthwise to the horizontal (and adjusting correspondingly also the pump speed in the re-circulation pipe). The maximum useful velocity in this system was 1.2 m/sec as measured in the channel centre, beyond which critical velocity the current attained the undesirable characteristics of "shooting flow"*. In the following, the expression "swift current" designates all currents of velocities between critical velocity and half this velocity. "Medium current" designates all currents of velocities of between one-half and one-fourth of the critical velocity. "Slow current" refers to all currents of velocities below one-fourth of the critical one and above threshold velocity (the velocity at which the current starts to be able to move grains at all). The latter velocity depended very much on the momentary bed smoothness, and was about one-tenth of the critical velocity.

Experiment Series 1: Effect of swift current

A swift current allowed to act on the sediment bed lifts up so much sediment that the total channel height of fluid is turbid with sediment and always $A/R \gg 1$. It establishes in the course of only a few minutes a bed configuration pattern that is in harmony with the eroding and depositing action of the current: straight, transversally aligned equidistant corrugation (see Figure 2, where these are seen as photographed through the glass side-windows of the flume). Preferential erosion takes place on those slopes of the corrugations that face away from the current and preferential deposition on those that face into the current, so that the corrugations, while maintaining their shape, translate themselves slowly in the same direction as the current flows, at about one-tenth the current velocity. The height of the relief increases somewhat with current velocity.

No experiment, either in this series or in any of the others, ever made it appear likely that there exists a set of conditions where the equilibrium relief could be made nil, i.e. where a flat bed would remain a flat bed. (Even shooting flow does not sweep the bed surface into a flat shape, but digs into it at some unpredictable spots and builds it up at others.) Theory too negates the possibility of dynamical stability of a flat bed.

Experiment Series 2: Effect of medium current

Medium currents raise loose sediment from the bed just enough to make the lower portion of the flowing fluid turbid, so that $A/R \approx 1$.

* So-called shooting flow ensues when current velocity reaches the order of magnitude of gravity-wave propagation. Then the moving fluid elements have no chance of adjusting their motions into a geometrically repetitive pattern. (Normally such a pattern is effected by gravity waves running ahead, being reflected from obstacles and running back. Under shooting-flow conditions there is only one-way communication between the bed configurations on different parts of the channel and no true equilibrium pattern results.)

To attain a bed configuration that persists (i.e. perpetuates itself instead of giving way to new evolving patterns one after the other), up to several hours of recirculating the current over the bed may be necessary, if the current chosen is a medium current. The self-perpetuating pattern which eventually emerges does not show that high degree of simplicity and uniformity displayed by the patterns formed by swift current. It is conceivable that there exist some less simple starting conditions of bed shape that lead into a different cycle of evolution than the one obtained in the author's experiments described in this paragraph (e.g. see Experiment Series 6 further on). The simplest starting conditions are a bed shape in equilibrium with a swift current, the speed of which is then reduced to the lesser speed of a medium current. Then the troughs of the transversal pre-existing corrugations are seen to become gradually filled up with sediment, but only at equi-distant nodule points, about one corrugation distance apart. The end product observed was an array of rectangularly arranged erosion holes as shown in Figure 3.

This array translates itself in the direction of the current at a small fraction of the current speed by the following observed mechanism. Suddenly, at irregular time intervals and at unpredictable spots, protuberances of suspended sediment are seen to shoot out of an erosion hole and then dissipate, while being carried down the current, by diffusing and settling into the sediment atmosphere. These protuberances are the result of spontaneous local increase of current turbulence. On closer inspection it is seen that the part of the erosion holes most afflicted are the slopes facing the current. These slopes are thus eaten up by erosion exceeding deposition while the opposite slopes are built forward by the complementary depositional activity of the current.

A variant of the above experiment series consisted of using non-steady medium current, such as intermittent swift current. The resulting bed shapes turned out to be similar to the above-described ones, often even of improved uniformity and regularity.

Experiment Series 3: Effect of slow current

Slow currents do not create a sizeable sediment atmosphere, but merely propel the surficial sediment grains rolling or sliding over the bed. Using the terminology of the sediment atmosphere, this means that $A/R \ll 1$. Under these conditions the initial abundance and local distribution of sediment on the bed surface becomes a decisive factor, so that one cannot give a generally valid description of the effect of slow currents. Even for the case of omnipresence of sediment on the channel floor and complete symmetry of the current, one cannot say for sure that evolution of the bed surface shape will lead to a self-perpetuating pattern of defined size.

When slowing a medium current that flows over a bed it has shaped (into the shape described in the preceding paragraph) the following changes can be observed. The crests bend gradually around so that the erosion holes become circular, and at the same time dwindle away at the down-current side of each erosion hole, so that the crest system finally breaks up into individual semi-circular knolls, each knoll in front of a flattened-out erosion hole. These knolls grow slowly in a haphazard manner,

the larger ones at the expense of their smaller neighbours. Their shape, as seen from the top, retains more or less the shape of a crescent moon or a horseshoe. Translation of the pattern units in the current direction is individual; the more the features grow, the slower the translation. There seems to be no definite end to this growth but gradual freezing of all translational motion of the surface features with increasing relief. Small-size features (ripples) that originate spontaneously here and there translate themselves with considerable speed over the current-facing slopes of the large knolls (see Figure 4).

Experiment Series 4: Effect of sediment scarcity

If there is a limit to the availability of sediment on the channel bottom so that a non-erosible floor under the sediment is exposed in the low spots of the relief, knolls cannot grow without limit at the expense of their neighbours since they become isolated by the baring of the low portions of the relief. Evolution continues then by virtue of the following mechanism. As small knolls travel forward faster than big ones, the small ones continuously overtake the bigger ones. Whenever it happens that a big one is in the way of a small one the two coalesce. The final self-perpetuating pattern is reached when all knolls have identical size and thus identical travel speeds, which state is reached in a surprisingly quick time. In Figure 5a, an almost final stage of an array produced* in this way of horseshoe knolls on a non-erosible substratum is seen photographed from the top through the water current.

Experiment Series 5: Effect on non-symmetry of sediment availability

If during an experimental run, sediment was plentiful all the time on one, say the left, bank of the main current bed and continuously trapped on the other bank, sediment would drift also, energised by the fluid motion's *random* components (turbulence-agitated diffusion), *across* the current direction. Such conditions of non-symmetry of sediment availability could be created simply by tilting slightly sideways the false bottom described in the preceding paragraph. The effect of cross-current drift of sediment on the sediment-morphology on the bottom is very pronounced. With plentiful sediment and stronger currents, the sediment shapes into obliquely aligned corrugations similar to the artificial corrugations shown in Figure 5b. With scarce sediment and slower currents, the pattern of horseshoe knolls shown in Figure 5a is obtained, but distorted so that the right prongs of the horseshoes are extended and the left ones reduced to rudiments. The degree of this distortion is a measure of

* For convenience, sediment-scarcity in these experiments was not produced by emptying the flume and connected pipes of a portion of the sand, but by the following artifice. A "false bottom" with legs was placed into the channel so that the sediment-carrying current flowed partly underneath it and partly over it. The level of this false bottom was variable and so was the configuration of the bottom itself. In the experiment described in this paragraph, the false bottom was flat, only slightly roughened. In experiments described in the following paragraphs, the false bottom was corrugated, as shown in Figure 5b. The length of the false bottom was 150 cm (the length of the flume's working section) and its width 8 cm narrower than the flume's width. Its leg height was adjusted to give the desired degree of sediment scarcity in each case.

the intensity of the cross-current sediment drift. In Figure 5a some slight distortion of this kind can actually be perceived, owing to some extremely slight tilt of the false bottom during production of this particular specimen.

Experiment Series 6: Effect of pre-existent bed configuration

A false bottom of non-symmetrical non-erosible shape (a rectangular piece of corrugated sheet, cut so that the corrugations run 45° inclined to the edges and current direction, as shown in Figure 5b) inserted into the current in the flume proved to induce cross-current drift of sediment even if sediment availability itself was painstakingly made equal at both sides of the current. The drifting could be noticed by eye.

In the course of time, however, current transversal ripples superimposed themselves on the corrugation crests and on the corrugation troughs. Growing steadily, they tended to change the oblique alignment of the corrugations to transversal alignment.

SAND TRACT MORPHOLOGIES OCCURRING IN ISRAEL

The sand tracts occurring in Israel, except those scattered among the mountainous stone desert in the south of the country, are coastal dune areas of different morphological age, substratum, surroundings and wind regime, displaying different morphologies in different regions. Their common denominator is that the sand source is a defined line, namely the beach. The sand morphology specimens described in the following shall be referred to as prototype specimens in view of the fact that the experiment series reported here had been selected to model dynamically just those typical specimens. The specimens shall be presented here in such sequence that Experiment Series 1 models Prototype Specimen 1, Experiment Series 2 models Prototype Specimen 2, and so on.

Prototype Specimen 1: Ripple marks

The sediment atmosphere for the case of wind-driven sand is determined by saltation height and is thus fairly constant, about 30 cm, unless there is very strong wind (or local turbulence for other reasons). Thus, eolian morphological features that are dynamically analogous to those water-produced morphological features for which $A/R \gg 1$ (Experiment Series 1) are those that have the smallest geometrical dimensions: the eolian ripple marks found on every wind-swept sand surface as seen, for instance, in Figures 6a and 6b (which are not typical of any specific locality. The white arrows indicating wind direction show the transversal alignment of the ripple marks, which typically is also the alignment of their dynamical counterpart shown in Figure 2). They are mentioned here only for the sake of completeness.

Prototype Specimen 2: Erosion hollows

A region where sand is transported not by steady wind but rather by intermittent gusts from opposite directions (the turbulence of which does succeed in raising temporarily the sediment atmosphere considerably) is the plain of Acre. A specimen of the sand morphology found on this plain is seen on the aerial photograph in Figure 7. A dia-

gram showing the wind regime in winter (full lines) and in summer (broken lines) as stated in Ashbel's Meteorological Atlas is reproduced in the marginal inset of the same photograph. None of the wind directions is predominant, since the shifting winds mutually cancel their direct shifting effects. Nevertheless, sand travels inland steadily, owing to the sand-trapping action of the swampy and vegetated land on one side and the continuing sand supply from the beach on the other side, a sort of diffusion being effected by the random components of the winds. Conditions here resemble best the ones produced in the variants of Experiment Series 2, and so do the morphological features obtained. There are zig-zag crests enclosing erosion hollows, so that the latter form a rectangular pattern of their own, diagonally aligned to the general direction of the crests. In winter the wind gusts are seen to whip up sand protuberances from the hollows, which presumably are the dynamical prototypes (several hundred times larger) of the protuberances seen in the model experiments. Also all geometrical dimensions of the prototype features are several hundred times larger than those of the model, so that $A/R \approx 1$.

Prototype Specimen 3: Horseshoe dunes

The wind regimes in the rest of the prototypes to be described here are characterised by the dominance of one steady wind direction (see diagram on the marginal inset of Figure 8). Thus the sediment atmosphere is always low and sand would travel mainly in the dominant wind direction, analogous to conditions of Experiment Series 3, if sand were everywhere deep and plentiful. However, there is no large continuous area where sand depth would not be a limiting factor, mainly because the ground-water table is everywhere in this coastal region close to the dune surface and the water-pervaded substratum is not erodible by wind. Thus there is here no real continuous large area covered with ever-growing dunes comparable to those in Experiment Series 3 produced on model-scale. (Such dunes would look like those shown on Figures 6a and 6b, centre and prong respectively.) Only isolated dunes of this kind occur in odd patches here and there.

Prototype Specimen 4: Array of horse-shoe dunelets

The non-erodible substratum mentioned above as the growth-limiting factor of horseshoe dunes causes the incipient horseshoe dunes to form a repetitive array which is persistent, since the individual horseshoes do not have a chance to grow at each other's expense. They may grow only until the substratum becomes exposed in the deep spots of the array. To show the array on a single plate, vertical aerial photographs have been fitted together in Figure 8 to form a "mosaic". (The original photographs can still be distinguished by the differences of tone on the two sides of the straight lines where they were joined). Scale and wind regime are indicated diagrammatically in one of the marginal insets. In the other inset the position of the sand-source (the coast) is indicated, which extends parallel to the bottom edge of the mosaic, about 500 m beyond it.

This is rather similar to the effect produced in Experiment Series 4.

*Prototype Specimen 5: Elongated dunes**

The horseshoes seen in Figure 8 display asymmetry similar to the asymmetry of those experimentally obtained and shown in Figure 5a. Their right prongs are more developed than their left ones. As in the case of the model, this phenomenon is associated with asymmetry of sand availability. The asymmetry in the prototype case is attributable to the sand-supplying coast being on one side of the main wind stream, the sand-trapping inland on the other. Thus there is traffic of diffusive sand motion across the main wind stream.

In Figure 9, which depicts a sand tract parallel to the one shown in Figure 8, situated further inland (i.e. closer to the sand-trapping region), this asymmetry is seen to have become extremely pronounced: the left prongs of the horseshoes are only rudimentary, hardly discernable at all in some cases, while the right prongs now completely dominate the pattern. From the ground these elongated dunes look like those shown in Figure 6b.

Prototype Specimen 6: Superimposed ridges

The obliquely-aligned elongated dunes are not only a result of diffusive sand traffic across the main wind direction, but—as Experiment 6 proved—are also a factor contributing in turn to cross-wind sand traffic. This means that the obliquely-aligned elongated dunes in the fringe area of the coastal dune belt translate themselves inland by a self-accelerating process, and eventually outrun the rate of sand supply coming cross-wind from the coast. Thus the outlying portion of the coastal dune belt, if it consists of obliquely aligned dunes, is likely to sever itself at some stage from the main body of coastal sand, and then develop a morphology suiting the new conditions. Such a morphology is shown in Figure 10, a vertical aerial photograph of a sand tract parallel and situated landward to the areas pictured in Figures 8 and 9 but not adjacent to them: there is a vegetated area of several kilometers width between. There is no doubt that this tract was once continuous with the tracts described before. Then it developed its basic morphology—and thereafter was severed by its own action or by an accident of nature.

The repetitive direction of the small ridges that are seen superimposed on the elongated dune's ridges and troughs follows the alignment of the pre-existing elongated dunes. This fact indicates that sand transport takes place not only in the direction of the main wind, but is deflected in the landward direction, obviously because of the asymmetry of the pre-existing morphology. At the same time it is seen—from the alignment of the individual *faces* of these same ridges, which is strictly transversal to the dominant wind direction—that there is a tendency in the system—starting with the smaller features—to revert to a symmetrical pattern since the external factors of asymmetry (left-hand side source) have ceased to exist.

This is in line with the observations of Experiment Series 6.

* In some publications these dunes have been referred to as "Seif" dunes, while horseshoe dunes have been called "Barchan" dunes. The author feels that these terms should remain reserved for desert type dunes, and not be used for coastal type dunes, in order to avoid confusion.

THE HELP OF DYNAMICAL MODELS FOR PURPOSES OF GEOMORPHOLOGICAL ANEMOMETRY AND PALAEO-ANEMOMETRY

One of the purposes of geomorphological studies of sand tracts is to obtain a scientific tool for air-photographical evaluation of wind regimes of inaccessible desert areas, or, from analysis of fossil landscapes, for the evaluation of wind regimes of past geological epochs. Rosenan (1943) and Striem (1954), who have attempted to correlate present-day wind regime and dune alignment for sand areas near the ones described here, have not reached entirely identical conclusions. The wind regime of past periods was discussed by Picard (1943) on the basis of the presence of a huge cemented sand ("Kurkar") ridge presumed by him to be a fossil "Seif" dune. His deductions are, unfortunately, subject to re-examination because of a misquotation on which he based his reasoning*. These attempts in the past so far demonstrate that the problem has some urgency, but to be solved, more factors must be taken into consideration than could be done by those authors at that time. It is impossible to correlate merely main-wind direction and dune alignment. The inter-relation between these and all the additional factors (sand supply, sand kind, pre-existing morphology, and traps, wind steadiness, etc.) must be studied first. Such a study is possible only by exhaustive experimentation, which in turn is possible only by means of dynamical models. The selected experiments described in this paper have revealed some of the significance of such factors as sand source or sand trap location in relation to wind direction, and of pre-existing morphology. But certainly there are other factors operative, not included in the present study (e.g. sand composition, treated by the author (1951).

This state of affairs makes geomorphological anemometry and palaeo-anemometry more complicated. But when finally developed, it will render also information regarding the environment, in addition to wind-data.

REFERENCES

1. ASHBEL, D., 1950. *Bioclimatic Atlas of Israel and the Near East*, The Hebrew University of Jerusalem, 154 pp.
2. BAGNOLD, R. A., 1942, *The Physics of Blown Sand*, Methuen and Co. London.
3. ESCANDE, L., 1951., Similitude des ondulations de sable des modeles reduit et des dunes du desert, *La Houille Blanche*, No. special A/1950;
4. ESCANDE, L., 1951, *Colloque International No. 35*, Centre National de la recherche Scientifique (Colloque d'Alger), pp. 71-80.
5. PICARD, L., 1943, Structure and volution of Palestine, *Bull. Geological Dept., The Hebrew University of Jerusalem*, 4, Nos. 2-3-4.
6. RIM, M., 1951, Les classements des mineraux du sable par les agents naturels sin les dunes cotieres, *Colloque International No. 35*, Centre National de la Recherche Scientifique (Colloque d'Alger), pp. 259-274.
7. RIM, M., 1951, The influence of geophysical processes on the stratification of sandy soils, *Journ. of Soil Science*, 2, 188-195.
8. ROSENAN, E., 1953, "Seif" dune alignment and wind direction in Sinai and the Negev, *Eretz-Israel, Liff Memorial Volume* (in Hebrew); *Israel Expl. Soc., Jer.*, 2.
9. STRIEM, L., 1954, The seifs on the Israel-Sinai border and the correlation of their alignment, *Bul. Res. Counc. of Israel*, 4, 195-198.

* He quoted (p. 96) Bagnold to say that Seif dunes are the product of uni-directional wind regimes, while Bagnold (1942, p. 195) states them to be products of bi-directional ones.

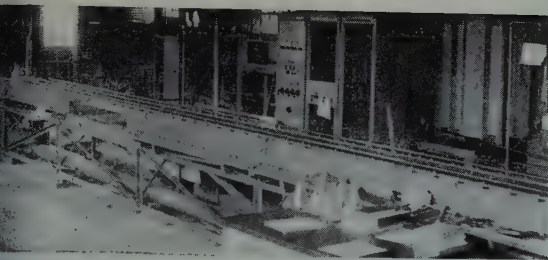


Figure 1
View of experimental flume

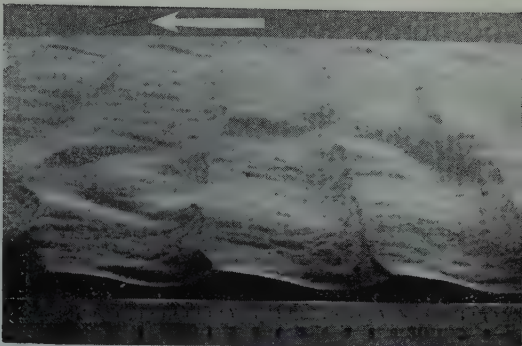


Figure 2
Miniature landscape photographed through the flume window during swift current flow

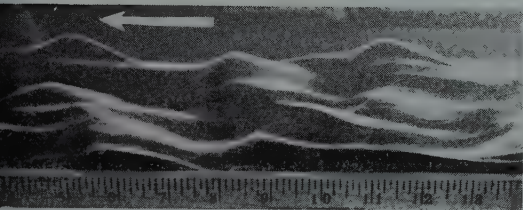


Figure 3
Miniature landscape photographed through the flume window during medium current flow



Figure 4
Miniature landscape photographed through the flume window during slow current flow

Figure 5a
Miniature landscape
photographed from
channel top, show-
ing plan view of sand
configuration on the
floor

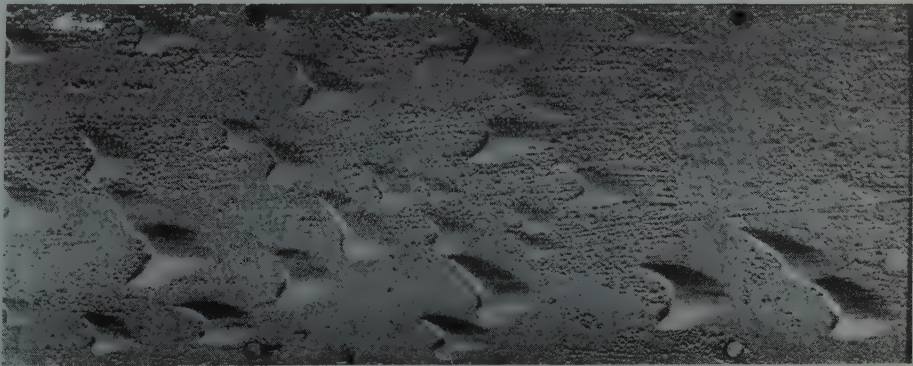


Figure 5b
Arrangement of elevated
floor with oblique cor-
rugations (line drawing)

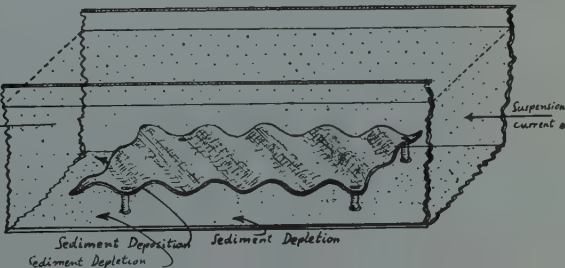




Figure 6a
Centre part of horseshoe
dune

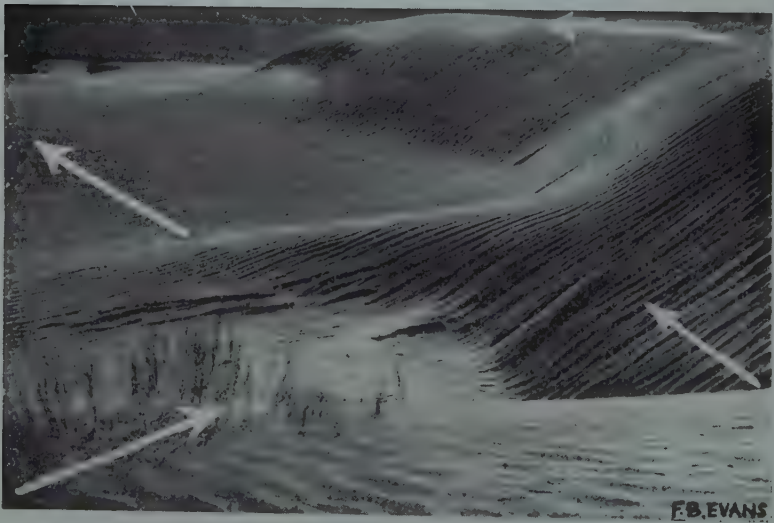


Figure 6b
Elongated part of
dune

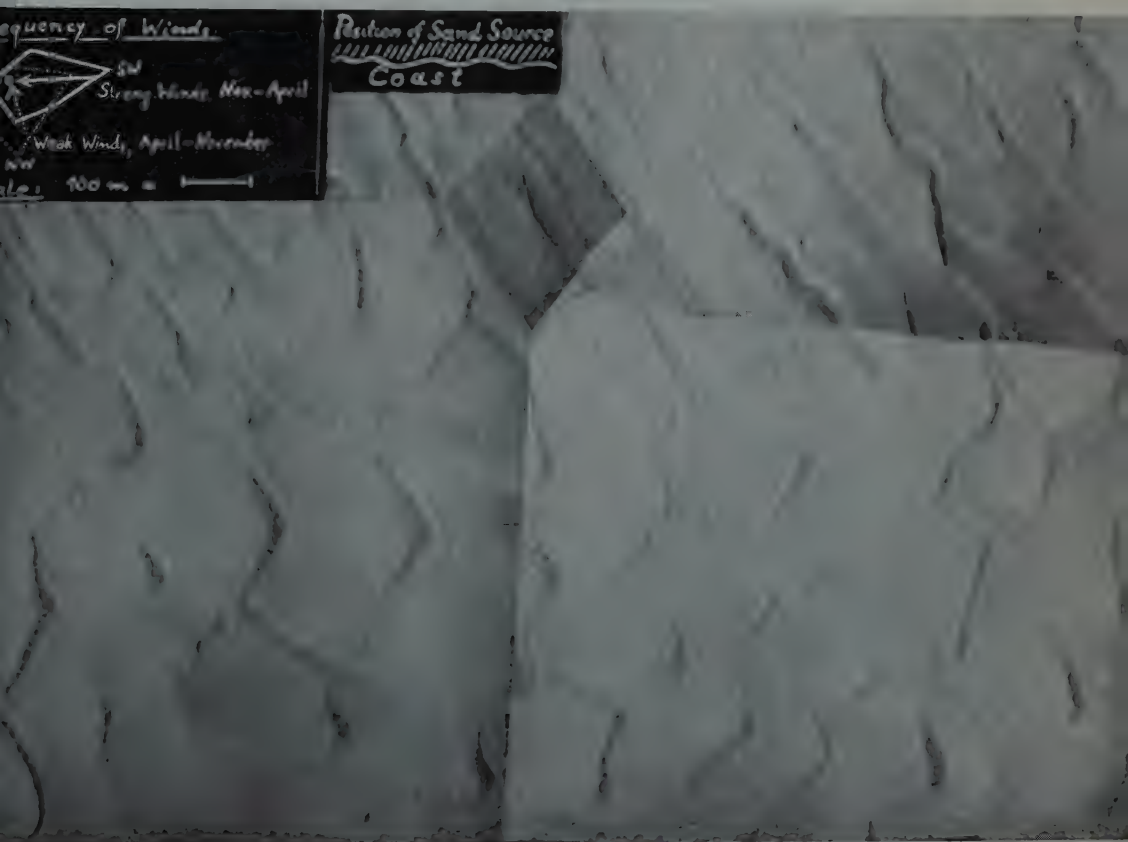
Figure 7

Vertical aerial photograph
of dune landscape near Acre



Figure 8

Vertical aerial photograph (mosaic) of
landscape next to the Mediterra-
nean coastline in the south of Israel



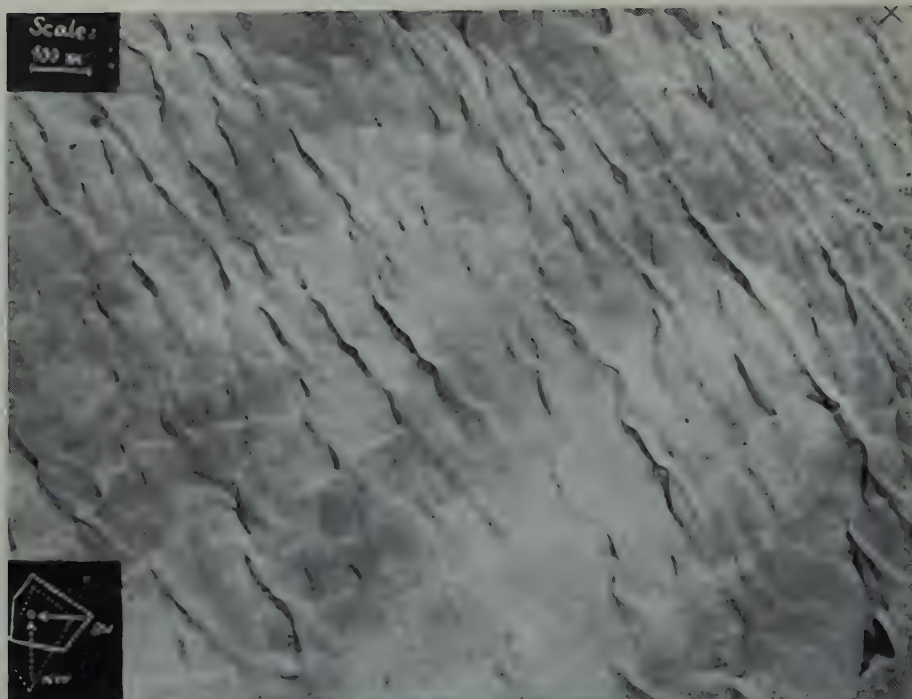


Figure 9
Vertical aerial photograph of dune landscape adjacent to the one shown in Figure 8



Figure 10
Vertical aerial photograph of dune landscape further inland in the south of Israel

TENTATIVE ENERGY AND WATER BALANCES FOR THE DEAD SEA

J. NEUMANN

*Meteorological Service, Israel Ministry of Transport and Communications**

ABSTRACT

The average annual rates of evaporation from the northern and southern basins of the Dead Sea are calculated from the energy balance of the sea. The resulting evaporation rates are as follows: Northern basin— 150 cm yr^{-1} (nominally, 147 cm yr^{-1}), southern basin— 180 cm yr^{-1} . For the Dead Sea as a whole, the rate works out as 155 cm yr^{-1} .

Next, from a combination of the energy balance and water balance approaches, average monthly evaporation rates are derived. These figures and figures for monthly lake level change lead to estimates of monthly inflow of water into the lake. Finally, the figures for monthly inflow are partitioned into component terms in a tentative manner. One of the conclusions of the analysis is that the underground inflow of water to the Dead Sea is at most of the order of $10^7 \text{ m}^3 \text{ yr}^{-1}$.

1. INTRODUCTION

1.1 *Method of calculation*

The annual rate of evaporation from the Dead Sea is calculated in this study by the energy balance method. No details of the method will be given here. A review and critical remarks on applicational aspects of the method are found in a paper by Anderson (1952). A brief review and discussion are given in a paper by the present writer (1953a) in connection with an investigation of the energy balances of and evaporation from Lake Hula and Lake Tiberias. By considering the energy balance of the Dead Sea, the present study completes the investigation for the lakes of the Jordan Rift.

The fundamental idea of the method is that in the process of evaporation, heat (latent heat of vaporisation and in the case of a saline lake such as the Dead Sea, "differential heat of solution") is being removed from the water body. By virtue of the principle of conservation of energy, it is possible to express this heat energy by means of the other terms constituting the energy or heat balance of the water body. The terms of the heat balance may be divided conveniently into two groups: radiation group and convective-conductive group. Evaporation is by far the most important term of the second group.

The magnitudes of various radiation terms forming the radiation balance of the Dead Sea were computed in almost exactly the same manner as followed in the

* Present address: Department of Meteorology, The Hebrew University of Jerusalem.

(B) Southern basin

Month	T_w^{***} °C	T_a^* °C	e_w^{****} mb	e_a^* mb	P^{**} mb	C^* tenths	β^{***} g*cm ⁻³
January	17.5	15.9	15.2	10.5	1066	3.6	1.188
February	18.7	16.8	16.8	9.6	1065	3.3	1.185
March	21.5	19.4	20.1	10.5	1063	2.4	1.183
April	24.8	24.0	24.4	11.3	1061	1.6	1.182
May	27.7	29.0	28.4	14.1	1057	2.1	1.182
June	30.2	31.6	33.0	15.7	1054	0.3	1.183
July	32.0	33.6	36.8	17.3	1051	0.2	1.184
August	32.2	33.8	37.1	18.0	1052	0.2	1.185
September	30.3	31.8	32.4	19.3	1055	0.5	1.187
October	27.0	28.0	27.2	16.7	1060	1.3	1.188
November	23.0	23.0	20.9	14.4	1062	2.2	1.189
December	18.5	18.1	16.3	11.6	1065	3.7	1.19
Annual average	25.28	25.4	24.6	14.1	1059	1.8	1.185

- * Data for Dead Sea Works (Factory), South, 1943/47
- ** Data for Kallia, 1942/46
- *** Data due to Ashbel (1950 and files of data)
- **** See note No. 4 for the northern basin

Department of Meteorology and Climatology, The Hebrew University of Jerusalem, covering a longer period. Temperature data for Dead Sea Works, North, are published on p. 13 of the supplement *Meteorological Normals of Israel* to Ashbel's (1951) *Regional Climatology of Israel*. Data of cloud amount for the latter station as well as the temperature data for Dead Sea Works, South, ("Camp"), are taken from files of Ashbel's data in the archives of the Meteorological Service.

a) Air temperatures — yearly averages

Station	Period	Air temperature (°C)	Supervising authority	Remarks
Kallia	1942/46	23.6	P. M. S.	See Table IA
Dead Sea Works, North	1928/47	23.8	D. M. C. H. U.; from 1942: P. M. S.	Station 3.5 km from Kallia
Dead Sea Works, South	1943/47	25.4	P. M. S.	See Table IB
Dead Sea Works, South (Camp)	1936/47	25.0	D. M. C. H. U.	

b) Cloud amount — yearly averages

Kallia	1942/46	2.9 tenths	P. M. S.	See Table IA
Dead Sea Works, North	1936/47	3.0 tenths	D. M. C. H. U.; from 1942: P. M. S.	

P. M. S. = Palestine Meteorological Service
D. M. C. H. U. = Department of Meteorology and Climatology, The Hebrew University of Jerusalem

It is seen from the above comparison that the differences between the averages of the data in Table I and those for longer periods are small. For that reason, we may consider the data in Table I as representative for a period of some length.

A further point illustrating the relatively small variability of meteorological elements and their effects on evaporation is offered by the recent work of C. E. Jacob (see Section 5 below) who computed the evaporation rate from the Dead Sea by studying fluctuations of meteorological and hydrometric data, for the years 1930/37 and 1938/44, respectively. The resulting rates differ by *less* than 1%.

1.22 *Temperature of surface waters.* Systematic measurements are available only for the southern basin, initiated and supervised by Ashbel (1950, p. 76, Figure 136). Data for the northern basin, which is the major basin (area ca. 760 km² vs. an area of ca. 260 km² for the southern basin, at a lake level of about -392 m M. S. L; see de Leeuw, 1946), are deficient. The figures adopted (Table IA) are the outcome of interpolation between surface water temperature data for the southern basin, on the one hand, and for Lake Tiberias (Ashbel 1945) on the other hand. In making the interpolation, it was appreciated that deep water bodies (the northern basin has an average depth of 185 m, the southern basin 6.4 m; see de Leeuw 1946) tend to have somewhat high temperatures in autumn and winter, and somewhat low temperatures in spring and summer. Also, account was taken of such scattered data as are on hand for the northern basin.

The annual averages work out as follows:

Lake Tiberias	23.4°C
Dead Sea, northern basin	24.7°C
Dead Sea, southern basin	25.2°C

1.23 *Specific gravity of surface waters.* Systematic measurements are available for the southern basin (Ashbel 1951, p. 168 and p. 181; 1950, p. 78). Again, for the more important northern basin, the situation is far from satisfactory. Some values, especially those obtained in the vicinity of the Dead Sea Works, North (see Figure 1), and in the western half of the basin, are high (verbal communication by F. Yaron), such as 1.18 and even 1.19 g*cm⁻³, and several of the occasional observations taken by Ashbel (1950, p. 77) are similarly high. However, some *sporadic* measurements by Ashbel and by others (Ashbel 1951, p. 180; 1950, p. 11) are low: 1.14 g*cm⁻³ and even lower.

The view has been expressed in discussions that as a consequence of inflow of large volumes of sweet water, the average specific gravity of the surface waters in the northern basin is likely to be appreciably less than in the southern basin. Paucity of data makes it hard to decide the issue, but the following considerations tend to disfavour the view just cited.

The rivers and streams draining to the Dead Sea may be regarded to be like narrow jets of fluid entering a fluid of high density at rest. Now, from an examination of the

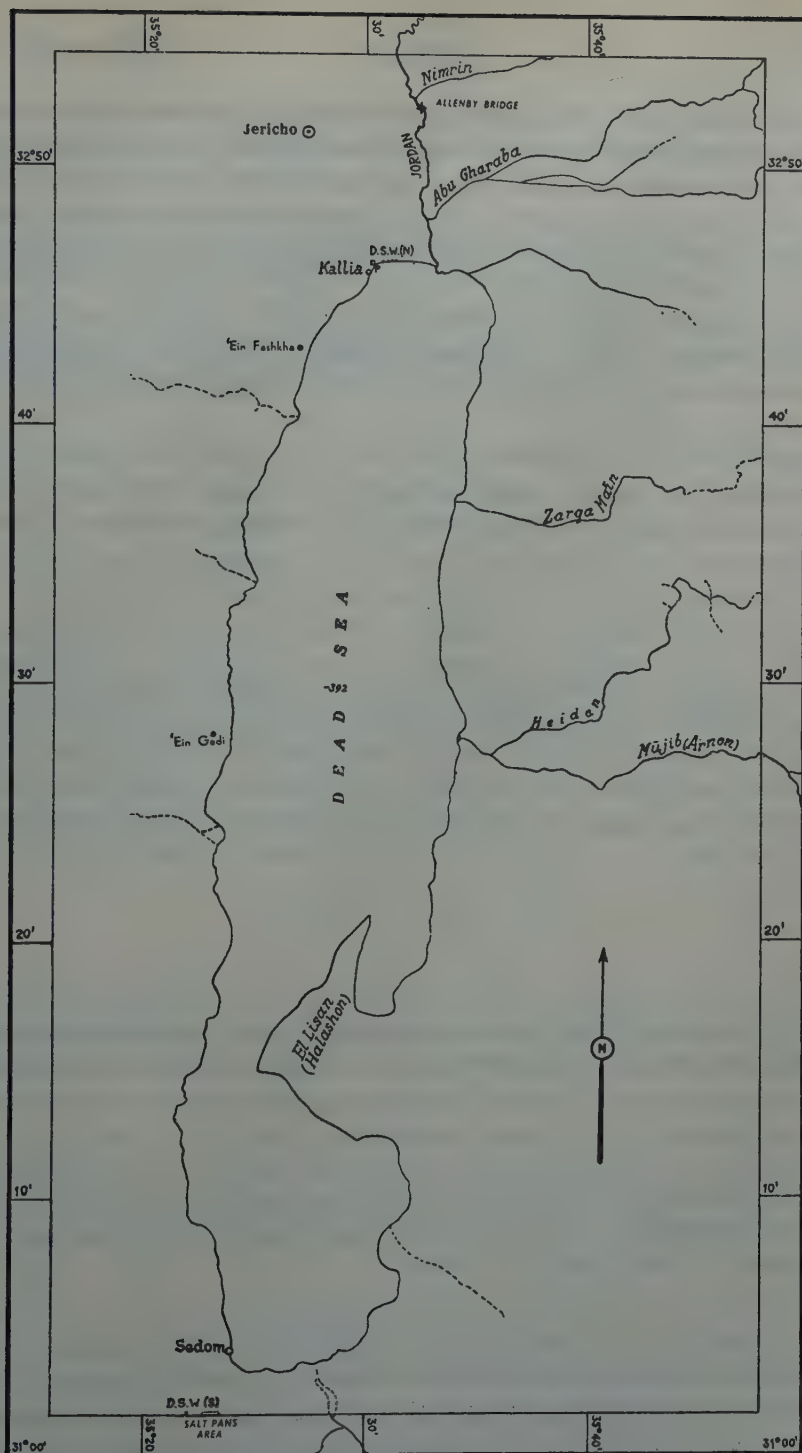


Figure 1

The lower Jordan and the Dead Sea

D. S. W. = Dead Sea Works

P = Police Station (near Kallia)

theoretical literature on jets (e.g. Goldstein 1938, Vol. 2, Art. 255), the writer is inclined to believe that the area of waters of low specific gravity near the affluence of rivers and streams is small. The literature on jets of a temperature and velocity different from those of the resting fluid would indicate that the region of disturbance in the resting fluid is limited in extent as a result of the mixing developing about the edges of jets.

We have assumed that a representative figure for the average annual specific gravity of the surface waters in the northern basin is 1.17 g*cm^{-3} . For the southern basin, Ashbel's figures (see Table I) give an annual average of 1.185 g*cm^{-3} which we adopt.

As the above figures, particularly the one for the northern waters, may be slightly in error, it is worth pointing out that a $\pm 1\%$ change in the value of specific gravity entails a change of $\mp 1\%$, approximately, in the evaporation rate. Raoult's law

$$\frac{e_{w0} - e_w}{e_{w0}} = \xi, \quad (1)$$

where e_{w0} = vapour pressure of pure solvent, e_w = vapour pressure of solution at the same temperature and ξ = mole fraction of solute, does, of course, not hold for brines of high concentration, such as the waters of the Dead Sea. However, inspection of a recent synopsis by Harbeck (1955, Figure 1) of data on vapour-pressure lowering by salts, taken mainly from the "International Critical Tables," shows that one may write for a not too narrow range of mole fractions, say $\xi' \leq \xi \leq \xi''$,

$$\frac{e'_w - e_w}{e_w} = c(\xi - \xi'), \quad (2)$$

e'_w = being the vapour pressure of the solution when the mole fraction of the solute is ξ' and c is a constant of proportionality. From (2), if Δ denotes a finite, but not too great change,

$$-\Delta e_w \propto \Delta \xi, \quad (3)$$

i.e. the vapour pressure of the solution changes *linearly* with the concentration ξ of the solute in the range $\xi' \leq \xi \leq \xi''$. On the other hand, the evaporation rate E can be represented by the (empirical) equation

$$E = K_a(e_w - e_a), \quad (4)$$

K_a being the "coefficient of vapour transfer" for the height at which e_a , the water-vapour pressure in air, is measured. It is clear from equations (3) and (4) that, for fixed values of K_a and e_a , the variation of E is linear, to a close approximation, with mole fraction of the solute or, what comes to the same, with specific gravity of the solution.

We infer from the above discussion that the evaporation rates obtained below are not likely to be in significant error on account of a minor uncertainty in the value assigned to the average specific gravity.

1.24 *Vapour pressure of surface waters of the Dead Sea.* For an average annual cycle, changes in storage of heat in the lake should vanish. Moreover, for an extensive water surface, horizontal advection of heat may be considered negligible. Under such conditions, the convective-conductive transfer of heat to the atmosphere, say Q_A , will equal the net radiation surplus Q_r at the lake surface, or

$$Q_A = Q_r. \quad (5)$$

But

$$Q_A = Q_e + Q_c, \quad (6)$$

Q_e standing for the heat utilised in evaporation, which in the case of brines includes, as pointed out earlier, in addition to the latent heat of vaporisation and a small term representing "energy advected by the evaporated water" (for the latter, see Anderson 1952), the differential heat of solution (e.g. Glasstone 1951, p. 241). In (6), Q_c is the symbol for the "sensible" heat transferred from the lake surface to the air. Further, Bowen's (Bowen 1926, Anderson 1952) ratio is

$$\frac{Q_c}{Q_e} = R, \quad (7)$$

$$R = 61 \times 10^{-5} P \frac{T_w - T_a}{e_w - e_a}, \quad (8)$$

where P = atmospheric pressure in mb, T_w and T_a = temperature of water surface and air, respectively, in °C, e_w = vapour pressure of the water surface and e_a = water vapour pressure in air at the height at which T_a is measured; e_w and e_a are in mb.

It is seen from equations (5) to (8) that for partitioning $Q_A = Q_r$ into its constituents Q_e and Q_c , we have to know e_w , the vapour pressure at the water surface. In the case of brines, e_w is, of course, lower than the vapour pressure at the surface of distilled water of the same temperature. From the point of view of turbulence theory, it is this lowered vapour pressure which accounts for the reduced evaporation rates from brines.*

A group of investigators (M. R. Bloch, Y. Schnerb and F. Yaron), representing the Research Council of Israel and the Dead Sea Works Research Laboratory, measured the vapour pressure of Dead Sea brine for a range of specific gravities and temperatures. The results of this work were kindly made available for the present study.

* On heat-balance theory, the reduced evaporation rate from brines is accounted for by the need of supplying the evaporating molecules with the differential heat of solution *in addition* to the latent heat of vaporisation.

Most of these vapour-pressure determinations were made for specific gravities and temperatures found in the "solar evaporation pans" or "salt pans" (where the brine is evaporated for the purpose of production of salts), which are much higher than those occurring in the surface waters of the Dead Sea. In view of this situation, we have decided to check how well the experimental data which correspond to natural conditions at the surface compare with data for (concentrated) sea water at similar chlorinities and temperatures.

Data of vapour pressure of sea water, for temperatures upward of 25°C and for concentrations up to saturation, are available through the work of the Japanese chemists Higashi, Nekamura and Hara (see Arons and Kientzler 1954). Arons and Kientzler* (1954) have lately completed and perfected the work of Higashi et al. by measuring the vapour pressure of sea water from 30°C downward to freezing point. In these experiments, chlorinities of sea water varied from 1% to 16%. *Inter alia*, the two authors present a diagram (their Figure 5) which combines, after some smoothing, their own results with those of the above-named Japanese chemists.

On plotting the data obtained for Dead Sea brine by the Research Council-Dead Sea Works Research Laboratory group in the diagram representing the smoothed results of Higashi et al. and those of Arons and Kientzler for sea water, no systematic separation of the data was apparent. It was for this reason that we have decided to proceed on the assumption that the lowering of vapour pressure of Dead Sea surface waters is the same as for sea water of similar chlorinity and temperature. For the northern basin of the Dead Sea, we have taken a chlorinity of 13.5% (~specific gravity 1.17 g*cm⁻³) and for the southern basin, a chlorinity of 15% (~specific gravity 1.185 g*cm⁻³).

2. AVERAGE ANNUAL RATES OF EVAPORATION

According to the results listed in Table II, the average annual radiation balances of the two basins are as follows:

Radiation terms	Northern basin (gcal cm ⁻² yr ⁻¹)	Southern basin (gcal cm ⁻² yr ⁻¹)
Insolation	+ 186,000	+ 202,000
Insolation reflected from lake surface	- 11,000	- 12,000
Atmospheric radiation	+ 276,000	+ 281,000
Atmospheric radiation reflected from lake surface	- 8,000	- 9,000
Thermal radiation from lake surface	- 333,000	- 335,000
Net radiation surplus at lake surface	+ 110,000	+ 127,000

* The writer is indebted to Dr. A. H. Woodcock of Woods Hole Oceanographic Institution, Woods Hole, Mass., for making a copy of a report by Arons and Kientzler available in advance of publication (Wood Hole Oceanographic Institution, Reference No. 52-94, dated October 1952).

Radiation balance for the surface of the Dead Sea (calculated). Unit: gcal cm⁻²

TABLE II

(A) Northern basin

Month	Short Waves		Long Waves		Balance		
	Insolation (B)	Insolation reflected from lake surface (C)	Atmospheric radiation (D)	Atm. radiation reflected from lake surface (E)	Thermal radiation from lake surface (F)	Short-wave balance (B)+(C) (G)	Long-wave balance (D)+(E)+(F) (H)
(A)	(B)	(C)	(D)	(E)	(F)	(G)	(H)
January	8700	-500	20700	-600	-25300	8200	-5200
February	9800	-600	18700	-600	-22700	9200	-4600
March	13900	-800	21400	-600	-25900	13100	-5100
April	18000	-1100	22000	-700	-26500	16900	-5200
May	19700	-1200	24300	-700	-28600	18500	-5000
June	23100	-1400	24400	-700	-28900	21700	-5200
July	22800	-1400	25700	-800	-30700	21400	-5800
August	21700	-1300	25700	-800	-30800	20400	-5900
September	18300	-1100	24400	-700	-29500	17200	-5800
October	13000	-800	24600	-700	-29500	12200	-5600
November	9200	-500	22500	-700	-27200	8700	-5400
December	7900	-400	21600	-700	-26800	7500	-5900
Annual Total*	186000	-11000	276000	-8000	-333000	175000	-65000

(B) Southern basin

Month	Short Waves		Long Waves		Balance		
	Insolation (B)	Insolation reflected from lake surface (C)	Atmospheric radiation (D)	Atm. radiation reflected from lake surface (E)	Thermal radiation from lake surface (F)	Short-wave balance (B)+(C) (G)	Long-wave balance (D)+(E)+(F) (H)
(A)	(B)	(C)	(D)	(E)	(F)	(G)	(H)
January	10000	-600	20700	-600	-25500	9400	-5400
February	11500	-700	18700	-600	-23500	10800	-5400
March	16800	-1000	21400	-600	-27000	15800	-6200
April	19900	-1200	22500	-700	-27200	18700	-5400
May	21200	-1300	25300	-800	-29400	19900	-4900
June	23400	-1400	24800	-700	-29300	22000	-5200
July	23500	-1400	26300	-800	-31100	22100	-5600
August	21700	-1300	26800	-800	-31200	20400	-5200
September	18300	-1100	25100	-800	-29300	17200	-5000
October	15200	-900	25000	-700	-29100	14300	-4800
November	11200	-700	22700	-700	-26600	10500	-4600
December	9200	-500	21600	-600	-25900	8700	-4900
Annual Total*	202000	-12000	281000	-9000	-335000	190000	-63000

* All annual totals have been rounded off to the nearest thousand

It is seen from the above that the amount of insolation reaching the northern basin is estimated at $186,000 \text{ gcal cm}^{-2} \text{ yr}^{-1}$. For the southern basin, the corresponding figure comes to $202,000 \text{ gcal cm}^{-2} \text{ yr}^{-1}$. The reason for this 8% difference resides first and foremost in the difference between cloud coverage for the two basins. Table I indicates that the average annual cloud amount at Kallia, in the north (see Figure 1), is 2.9 tenths, whereas at Dead Sea Works, South (Factory), in the south (see Figure 1), the parallel figure is 1.8. A recent analysis (Neumann 1954a) of the relationship between insolation and cloud amount shows that, under average conditions, each tenth of the sky obscured by clouds is responsible for a reduction by 5 to 6% of the insolation which would reach the surface from a cloudless sky.* Estimating the cloud coverage over the southern basin as just over one-tenth less compared with the northern basin, the calculations thus lead to an insolation rate ca. 6% higher than for the north. The remaining 2% of excess in insolation is explained as the result of two factors. The first is the difference in solar radiation reaching the top of the atmosphere over the two basins. It may be shown, by readily available equations or by reference to tables, that the outer atmosphere over the southern basin receives some $1,500 \text{ gcal cm}^{-2} \text{ yr}^{-1}$ more solar radiation than over the northern basin. The second factor is the lower water-vapour content of the atmosphere in the southern region of the lake. A dry atmosphere depletes by absorption less of the solar radiation than a humid atmosphere. Table I shows that at the southern station, the absolute humidity is 14 mb, while at the northern station it amounts to 16 mb. These are surface data, but under average conditions, there is a close connection between the water-vapour content of the air near the surface and the water-vapour content of the overlying atmospheric column.

The long-wave radiation balances (= atmospheric radiation *less* atmospheric radiation reflected from the lake surface *less* "thermal" radiation emitted by the lake surface) of the two basins are almost equal. A consequence of this is that the difference in net radiation surplus for the two basins practically equals the difference in insolation.

The net radiation surplus Q_r works out as $110,000 \text{ gcal cm}^{-2} \text{ yr}^{-1}$ for the northern basin and $127,000 \text{ gcal cm}^{-2} \text{ yr}^{-1}$ for the southern basin. Using equation (8) and the data of annual averages in Table I, the Bowen's ratios $R = Q_c / Q_e$ [equation (7)], and the terms Q_c and Q_e , $Q_c + Q_e = Q_r$ [equations (5) and (6)], turn out as follows (rounded off):

* By far the major part of the reduction is caused by the reflection of solar radiation from cloud tops back to space. Currently, the best estimate (of the world-wide average) of cloud albedo is 0.55 (private communication from Dr. S. Fritz, U.S. Weather Bureau, Washington, D.C.; see also Fritz (1949), Houghton (1954) and Neumann (1954b)). That is to say, 55% of the insolation incident on cloud tops is reflected from there. We may add here that the fictive quantity "insolation from a clear sky" which enters the radiation calculations is ca. $225,000 \text{ gcal cm}^{-2} \text{ yr}^{-1}$ for the Dead Sea area.

	Northern basin	Southern basin	
R	+ 0.07	− 0.01	
Q_c , gcal cm ^{−2} yr ^{−1}	+ 7,000	− 1,000	(10)
Q_e gcal cm ^{−2} yr ^{−1}	+ 103,000	+ 128,000	

A negative Bowen's ratio means that the *net* transfer of sensible heat is from the warmer air to the lake. This heat adds to the net radiation surplus and increases the rate of evaporation.

We have in (10) estimates of the quantity of heat expended by each of the two basins of the Dead Sea on evaporation. To express the rate of evaporation in terms of depth of water layer we have to remember that in getting 1 g of water vapour by evaporation from a brine, we have to supply the brine, as was pointed out before, with the so-called "differential heat of solution," in addition to the latent heat of vaporisation. Also, there is a minor correction to be made for the heat advected out by the evaporated water (for particulars, see Anderson 1952). The latter term we estimate at ca. 10 gcal per g of evaporated water (see Neumann 1953a). In brief, the evaporation rate E , in cm, is (Anderson 1952, Neumann 1953a)

$$E = \frac{Q_e}{\rho(L + 10)} \quad (11)$$

where ρ is the density of brine in g cm^{−3} and L is the latent heat of vaporisation, in gcal g^{−1}, for distilled water at the same temperature. For specific gravities of 1.17 and 1.185 g*cm^{−3}, the densities respectively are 1.195 and 1.21 g cm^{−3}. For a water temperature of 25°C, such as is the case for the Dead Sea, $L = 583$ gcal g^{−1}. Inserting the appropriate data into equation (11), we arrive at the following evaporation rates (N = northern basin, S = southern basin):

$$E_N = 147 \text{ cm yr}^{-1}, \quad E_S = 180 \text{ cm yr}^{-1}. \quad (12)$$

To obtain the evaporation rate from the lake as a whole, we have to give a weight of 3 to the figure for the northern basin, since its surface area is three times greater than the surface area of the southern basin, or

$$E_{\text{Dead Sea}} = 155 \text{ cm yr}^{-1}. \quad (13)$$

This figure will be used throughout the subsequent sections.

3. AVERAGE MONTHLY RATES OF EVAPORATION

The heat of the *net* radiation surplus at a water surface is disposed in two principal ways: part of it is conducted to the atmosphere and the remaining part is conducted into the subsurface layers of water where it enters into *transitory* storage. Unless depth-temperature data are available for the water body, it is not generally possible

to say how much of the radiation surplus was diverted to evaporation and sensible heat transfer to the atmosphere. The heat entering into storage, say Q_8 , may, be represented by the equation

$$Q_8 = c\rho \frac{\partial \bar{T}_w}{\partial t} \quad (14)$$

where c is specific heat, ρ = density, \bar{T}_w = average temperature of a water column and t = time. Clearly, when \bar{T}_w is a minimum or a maximum, $Q_8 = 0$. This occurs twice in the course of a smoothed annual cycle. Once, when the lake reaches its lowest temperature about the end of winter, and again, when the lake attains its highest temperature about the end of summer.

We assume for the Dead Sea that the two months when $Q_8 = 0$, are February and August, respectively. In adopting these months we are guided by Ashbel's (1945, see also Neumann 1953a) data for Lake Tiberias, which indicate that during February and August Q_8 is practically zero, and by the view that lakes situated in one and the same type of climate (and this is approximately true for Lake Tiberias and the Dead Sea), tend to have the same thermal behaviour.

By computing the evaporation rates for February and August, we shall be able to compute the rates for the remaining months. In this, we shall utilise the figure for the annual rate and some recent results concerning heat-balance theory of water bodies. The computation of monthly rates will be completed in five steps.

3.1 Step No. 1: February and August

Assuming $Q_8 = 0$, then taking values of Q_r from Table II and computing the Bowen ratios (equation (8)) for February and August, we arrive at the following figures:

	Northern basin (cm)	Southern basin (cm)	Weighted average (cm) (rounded off)
February	5.4	6.6	6.0
August	20.0	22.0	20.0

(15)

3.2 Step No. 2: June, July, September and October

The Dead Sea and its catchment are situated in a region where no noteworthy widespread precipitation falls between May and November. A few weeks after the last early spring storms, there is no storm-water inflow into the sea. The streams and springs settle down to a flow rate which remains practically constant throughout summer and early autumn. In hydrology, this flow rate is sometimes designated "dry-weather flow" or "base flow". As examples, we cite figures for the Yarmuk stream near its confluence with the Jordan and for the Jordan at Allenby Bridge

(see Figure 1). The data for the Yarmuk are from Ionides (1939, p. 139)*, those for the Jordan were obtained through the courtesy of the Hydrological Service, Israel Ministry of Agriculture.

TABLE III

Monthly discharge rates, in m³, of the Yarmuk near its confluence with the Jordan, and the Jordan at Allenby Bridge

	Yarmuk May 1926 — Sep. 1938 (m ³ × 10 ⁶)	Jordan at Allenby Bridge Oct. 1935 — Sep. 1947 (m ³ × 10 ⁶)
January	52	131
February	151	143
March	48	116
April	34	88
May	29	84
June	22	77
July	21	79
August	20	83
September	20	80
October	21	87
November	23	87
December	29	80
Annual	470	1,135

It may be objected that the constancy of flow in the Jordan in summer, as indicated by the data in Table III, was a result of regulation of this river at Degania by the Palestine Electric Corporation. This objection is not quite valid because the main season of flow control was in winter (Ionides 1939, p. 137).

We shall assume that from June to October inclusive the total inflow of water, surface and underground, into the Dead Sea takes place at a constant monthly rate I . But, for a lake without an outlet

$$I = E + \Delta L, \quad (16)$$

E being the evaporation rate and ΔL the amount of change in lake level, both for the same monthly period to which I refers. Writing a subscript to indicate the serial of the month, our assumption is that $I_6 = I_7 = I_8 = I_9 = I_{10}$, and from (16):

$$E_6 + \Delta L_6 = E_7 + \Delta L_7 = E_8 + \Delta L_8 = E_9 + \Delta L_9 = E_{10} + \Delta L_{10} \quad (17)$$

Given data for lake level change and the evaporation rate for *one* of the five months in question, we can at once obtain the evaporation rate for each of the remaining four months.

* In his report on the water resources of Transjordan, Ionides (1939, p. 189) uses the term "ground-water flow" for what we call "dry-weather flow", or "base flow".

An estimate of the evaporation rate in August was deduced from heat balance considerations and is stated under (15). Data of lake level are also available. Ashbel (1951) published monthly data for the years 1929 to 1946 (p. 181 in his book) and a diagram (p. 168) showing the average annual variation. The relevant observations were taken near the "Camp" of Dead Sea Works, South (Factory).

For the northern basin, the Hydrological Service (1950, p. 230) published monthly data for the years 1939 to 1947. The relevant observations were conducted by the Palestine Potash Ltd. in the neighbourhood of their former works in the north (Palestine Grid E 199.00, N 131.30). At this location, the gauge was protected from waves.

There are also two series of unpublished data, copies of records of which are deposited in the archives of the Meteorological Service. The first series is by the Palestine Potash Ltd., taken near their works in the north. Records of the observations go back to 1930. The second series is due to the Public Works Department of the former Palestine Government. Records of the data cover the years 1935 to 1947. The place of observations was the former Palestine Police Station situated near the Dead Sea Works, North.

The four sets of data are in *qualitative* agreement. All four give the highest lake level as occurring about the end of April or beginning of May, and the lowest level about the middle of November or beginning of December. From the four sets we "synthesised" an annual curve of lake level (Figure 2), according greater weight to the data for the north. Special attention was paid to data for the years 1937 to 1944, during which the level of the Dead Sea remained constant (see, e.g. Ashbel 1950, p. 78, Figure 141), apart from seasonal oscillations. The resulting monthly *changes* in lake level are listed in Table IV.

TABLE IV
Monthly changes of lake level, Dead Sea

(Based on data by Ashbel, the Palestine Potash Ltd. and the Public Works Department of the former Palestine Government)

Month	Level change (cm)
January	+12.5
February	+16
March	+11
April	+ 3.5
May	- 0.5
June	- 5
July	- 9
August	-10.5
September	- 9.5
October	- 7.5
November	- 3.5
December	+ 2.5
Annual	0.0

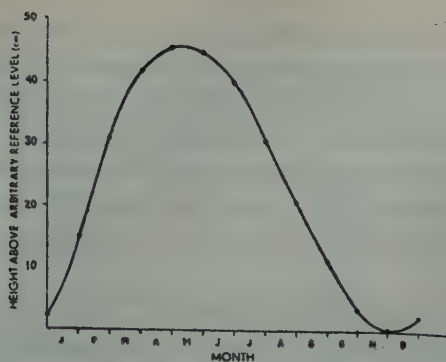


Figure 2
Annual curve of lake level of Dead Sea

By utilising the figure for the evaporation rate in August given under (15) (20 cm , $E_8 = 20$) and the data in Table IV, equation (16) results in the following evaporation rates for the months June, July, September and October:

$$\begin{aligned} E_6 &= 14.5 \text{ cm} \\ E_7 &= 18.5 \\ E_9 &= 19 \\ E_{10} &= 17 \end{aligned} \quad (18)$$

3.3 Step No. 3: November

Consider the idealised case where the annual variations of all three terms of the water-balance equation (16) are perfect sine curves. In this case, in the month when $\Delta L = 0$, $I = E$, with I and E being respectively the *average monthly inflow and evaporation*, i.e. *one-twelfth part of the average annual figures*.

It may be inferred from an energy-balance investigation (Neumann 1954a) of the problem of annual variation of evaporation from lakes that this variation comes nearest to a sine curve in the autumn and winter seasons. Now, during the autumn-winter semester of the year, for the Dead Sea, $\Delta L = 0$ about the end of November. Hence, following what was said in the foregoing paragraph, a good estimate of the evaporation rate for the monthly period centred about the end of November would be one-twelfth part of the estimated annual evaporation rate, i.e. $(155/12) = \sim 13 \text{ cm}$. But since we are interested in the evaporation rate for November proper, we have to increase slightly the above figure. By considering the rate deduced for October, we suggest to adopt for November the figure of 13.5 cm , or

$$E_{11} = 13.5 \text{ cm}. \quad (19)$$

3.4 Step No. 4: December and January

Let us here introduce the term "annual heat budget" Q_H of a water body such as a lake. The annual heat budget is the amount of heat required to raise the temperature

of a column of unit cross-section of the lake from its minimum temperature (late) in winter to its maximum temperature (late) in summer. This heat amount, which enters into storage in the lake during the spring and summer seasons, leaves the lake during the autumn-winter semester of an annual cycle. It will be seen from Figure 4 that deep lakes possess an annual heat budget of between 20,000 and 40,000 gcal cm^{-2} . Thus the heat released from storage in lakes of some depth during the cool season is an important source of heat for the lake surface to transfer to the atmosphere.

The writer has shown elsewhere (1953b) that Q_H may be computed *from surface data alone*, without soundings of depth temperatures, provided that an assumption is made in regard to the dates when the sea or lake reaches its minimum temperature and maximum temperature, respectively. Earlier, in "Step No. 1", we have assumed that in the case of the Dead Sea, these dates occur in February and August. We shall now make the more exacting assumption that the dates occur at mid-February and mid-August, respectively.

As before, we shall denote by Q_r the net radiation surplus at the lake surface, R = Bowen's ratio ($R = Q_c/Q_e$), L = latent heat of vaporisation, ρ = density of surface waters, α = a correction term accounting for the heat advected out by the evaporated water (earlier we have assumed for the Dead Sea $\alpha = 10$ gcal g^{-1}) and E = evaporation rate.

The above symbols marked by a prime will represent the values of these quantities for the period between mid-February and mid-August; a double prime will refer to the period between mid-August and mid-February. Without primes, the symbols relate to a complete annual cycle.

It is shown in the paper referred to above, that

$$Q_H = \frac{(1 + R'')(R - R') Q' - (1 + R')(R'' - R) Q''}{(1 + R)(R'' - R')}, \quad (20)$$

and

$$E' = \frac{Q_r' - Q_H}{\rho' [L' (1 + R') + \alpha']}, \quad E'' = \frac{Q_r'' + Q_H}{\rho'' [L'' (1 + R'') + \alpha'']}. \quad (21)$$

Naturally,

$$E' + E'' = E. \quad (22)$$

We shall now apply these equations to the problem of the Dead Sea. Table V lists for the northern basin, on the basis of Table I, half-yearly averages of the meteorological and limnological data which are required for obtaining the half-yearly Bowen's ratios R' and R'' . Also added are the half-yearly net radiation balances Q_r' and Q_r'' . The latter were compiled from Table IIA.

TABLE V
Half-yearly (15 February to 15 August and 16 August to 14 February) averages of meteorological and limnological data for the northern basin of the Dead Sea

T_w'	= 25.2°C	T_w''	= 24.2°C
T_a'	= 24.9°C	T_a''	= 22.3 °C
e_w'	= 28.7 mb	e_w''	= 27.1 mb
e_a'	= 16.2 mb	e_a''	= 15.6 mb
P'	= 1,057 mb	P''	= 1,063 mb
Q_r'	= 76,000 gcal cm ⁻²	Q_r''	= 34,00 gcal cm ⁻²
R'	= 0.02	R''	= 0.11
ρ'	= 1.19 g cm ⁻³	ρ''	= 1.19 g cm ⁻³
L'	= 583 gcal g ⁻¹	L''	= 583 gcal g ⁻¹

$$R = 0.07$$

Introducing the data of Table V into equations (20) and (21), it is found that

$$\begin{aligned} Q_H &= 30,000 \text{ gcal cm}^{-2} \\ E_N' &= 65 \text{ cm} \\ E_N'' &= 82 \text{ cm,} \end{aligned} \quad (23)$$

N being the symbol for the northern basin. $E_N' + E_N'' = E_N = 147$ cm, as expected. We note in passing that according to the above results, for the northern basin, *the evaporation rate in the autumn-winter semester exceeds the evaporation rate in the spring-summer semester*. This is reasonable in the light of what we know about the annual course of evaporation from deep water bodies and in view of the great depth of the northern basin (average depth ca. 185 m, de Leeuw 1946). We shall see further on that *the reverse relationship is obtained for the shallow southern basin*.

Before being able to utilise the figures under (23), we have to find the corresponding figures for the southern basin. It is, however, not possible to follow the procedure just described, for in the case of the southern basin, the Bowen's ratios R' , R'' and R are all small and nearly equal. Their use in conjunction with equations (20) and (21) might lead to serious errors. We therefore have to proceed in a different manner.

Let T_x be the annual maximum temperature, T_n the annual minimum temperature, both in °C, ρ the density in g cm⁻³ and c the specific heat, in gcal g⁻¹ deg⁻¹, of the water column whose annual heat budget is Q_H . Then, we may define an *equivalent lake-depth* D , in cm, such that

$$Q_H = \frac{D(T_x - T_n)\rho \cdot c}{2} \quad (24)$$

The factor $\rho \cdot c$ may be taken as unity, which is a fair approximation to truth, so that, numerically,

$$Q_H = \frac{D(T_x - T_n)}{2} \quad (25)$$

In a deep lake, there will be an epilimnion. Most of the heat represented by Q_H entering into storage in the lake will be confined to the epilimnion. If the lake is very deep, as is the case with the northern basin of the Dead Sea, the equivalent depth D will be less than lake depth. Nor will it be equal to the depth of the epilimnion. In equation (25) the term Q_H may be represented (see Figure 3) as the area of a triangle whose base is $(T_x - T_n)$ and its height D .

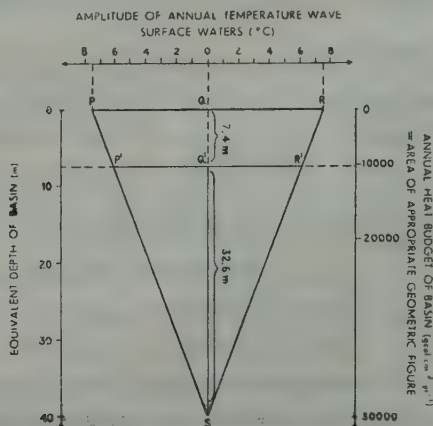


Figure 3

Calculation of the annual heat budget of the southern basin from the annual heat budget of the northern basin. Triangle PSR = northern basin, trapezoid PP'R'R = southern basin

Now, if in lakes the temperature range varied with depth linearly, D would be equal to epilimnion depth (assuming that heat-content variation is confined to the epilimnion). In reality, below an upper homothermal layer, this variation is something like an exponential reduction with depth, so that the reduction with depth takes place at a rate faster than linear. As a consequence, D should be less, probably much less, than epilimnion depth. We have deduced earlier for the northern basin of the Dead Sea an annual heat budget $Q_H = 30,000$ gal cm⁻²; the term $(T_x - T_n)$ may be obtained, to an approximation, from Table I(A). Taking $T_x = 31.5^\circ\text{C}$, $T_n = 16.5^\circ\text{C}$, $(T_x - T_n) = 15^\circ\text{C}$.

Inserting these data* into equation (25), we get $D = 4,000$ cm or 40 m, whereas the depth of epilimnion in the northern basin appears to be ca. 75 m. The latter we infer from salinity data due to Blake (1930, p. 7) and information due to Novomeisky cited by Braslavsky (1950, p. 15). Salinity data show little variation below about 75 m.

To estimate Q_H for the southern basin, we return to Figure 3 and equation (25). For the southern basin, from Table I(B), $T_x = 32.2^\circ\text{C}$, $T_n = 17.5^\circ\text{C}$, $(T_x - T_n) =$

* Strictly speaking $T_x = 31.5^\circ\text{C}$ is not the maximum temperature and $T_n = 16.5^\circ\text{C}$ is not the minimum temperature required. Rather they are average temperatures of the warmest and coldest months, respectively. We use them as the proper maximum and minimum temperatures are not available. The error incurred is compensated for by the value of D calculated from equation (25).

14.7°C. Since this temperature range is nearly the same as that for the northern basin, i.e. 15°C, we shall adopt the latter figure. This means that in Figure 3 we can use the same "base" PR both for the northern and southern basins. But since the southern basin is shallow, its average depth being 6.4 m (de Leeuw 1946), the temperature range at its bottom will not reduce to zero. Hence, it will be more appropriate to represent in Figure 3 the annual heat budget of the southern basin by a trapezoid whose base is PR.

Coming to the question of height (or, rather, depth) of the trapezoid we note that in the case of a *shallow* lake, allowance must be made for the seasonal variation of heat content in the lake bed. Heat enters the bed in spring and summer and, under average conditions, the same amount of heat should leave the bed in the remaining seasons of a full annual cycle. The alternating part of the lake bed heat content may be written

$$\int_0^{\infty} c\rho T_z dz, \quad (26)$$

where c = specific heat, ρ = density, T_z = alternating part of the temperature wave at depth z in the lake bed. By following Bowden's (1948) evaluation of that term for the Irish Sea, or by repeating the more detailed considerations by the present writer (1953a) concerning Lake Hula, we find that the heat budget of the lake bed is equivalent to the heat budget of a layer of water ca. 1 m thick at the bottom of the lake. Hence, in order to allow for the effect of lake bed, we should increase the figure for lake depth by 1 m. We thus assume, for the purposes of evaluation of Q_H by means of Figure 3, that $D = 740$ cm ($= 640 + 100$).

It is readily confirmed that for $D = 740$, the trapezoid PP'R'R in Figure 3 has an "area", that is to say, an annual heat budget, of ca. 10,500 gcal cm⁻², or about one-third of the annual heat budget computed for the northern basin.

A confirmation of the approximate correctness of the above result is offered by Figure 4, which plots data of annual heat budgets of over 100 lakes vs. average lake depth. Most of the data were obtained through the courtesy of G. E. Hutchinson, Osborn Zoological Laboratory, Yale University, New Haven, Conn. The remaining data were collected by the writer from limnological literature on hand. The free-hand curve drawn in Figure 4 represents a "best" estimate of annual heat budget from data of average depth for lakes. It will be seen that for an average depth of 6.4 m, the diagram gives an annual heat budget $Q_H = 10,000$ gcal cm⁻².

We adopt for the annual heat budget of the southern basin of the Dead Sea the round figure of 10,000 gcal cm⁻² and use it in computing E_S'' , where the subscript symbolises the southern basin. By having estimates of E'' both for the northern and southern basins, we shall be able to compute E'' for the lake as a whole and arrive at estimates of the evaporation rates in December and January (and in spring — see Sub-section 3.5).

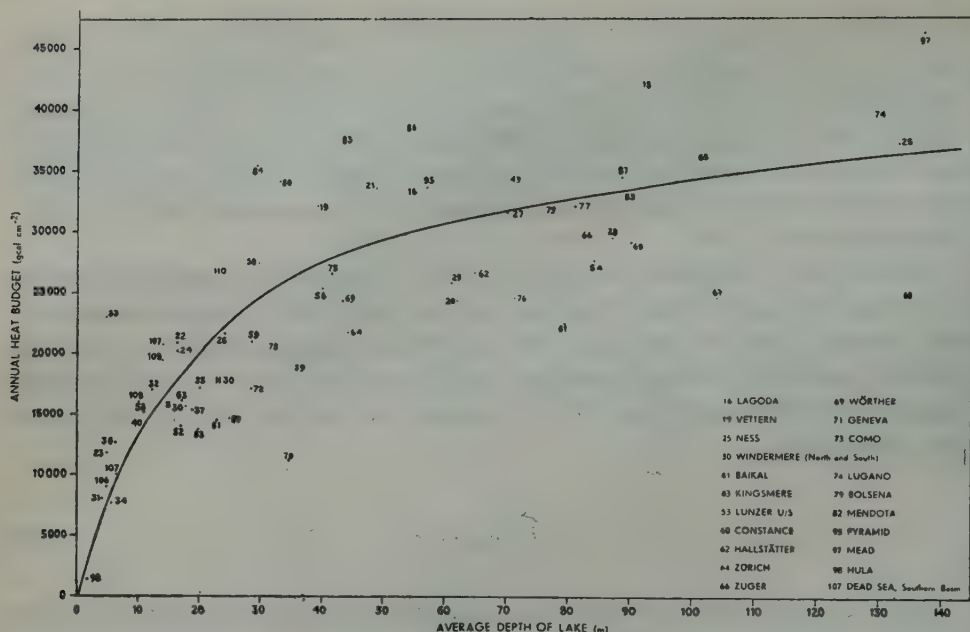


Figure 4

The annual heat budget of lakes as a function of average depth of the lake. (Most of the data was obtained through the courtesy of G.E. Hutchinson, Osborn Zoological Laboratory, Yale University, New Haven, Conn.) The names of some of the better-known lakes are stated in the lower right-hand corner

The data needed for computing E_s'' are listed in Table VI. They were obtained from Table I(B).

With the data on the right hand side of Table VI, equation (21) gives

$$E_s'' = 73 \text{ cm}, \quad (27)$$

and since for the southern basin, $E = 180 \text{ cm}$,

$$E_s' = 107 \text{ cm}. \quad (28)$$

Thus in the southern basin in spring and summer, the evaporation rate considerably exceeds the rate for the autumn-winter semester. This is the opposite of what we

TABLE VI

Meteorological and limnological data for the southern basin of the Dead Sea for the period from mid-August to mid-February

$T_w'' = 23.4^\circ\text{C}$	$Q_r'' = 42,000 \text{ gcal cm}^{-2}$
$T_a'' = 26.6^\circ\text{C}$	$R'' = -0.01$
$e_w'' = 26.3 \text{ mb}$	$L'' = 585 \text{ gcal g}^{-1}$
$e_a'' = 14.4 \text{ mb}$	$q'' = 1.21 \text{ g cm}^{-3}$
$p = 1063 \text{ mb}$	$\alpha = 10 \text{ gcal g}^{-1}$

found for the northern basin. Far from being at variance, the two results are in accord with what we know about the annual variation of evaporation from shallow and deep water bodies, respectively. Once more denoting by subscript N and S the northern and southern basins, in that order, we have

$$\begin{array}{lll} E_N = 147 \text{ cm} & E_N' = 65 \text{ cm} & E_N'' = 82 \text{ cm} \\ E_S = 180 \text{ cm} & E_S' = 107 \text{ cm} & E_S'' = 73 \text{ cm} \end{array} \quad (29)$$

Taking the weighted averages of the E_S'' , we get for the Dead Sea as whole,

$$E'' = 80 \text{ cm.} \quad (30)$$

So far, we have the evaporation rates for August, September, October, November and February. Remembering that E'' refers to the period from mid-August to mid-February, we shall have to divide the rates for August and February in two parts. Of the 20 cm evaporation rate for August (see equation (15)), we tentatively assign 10.5 cm to the second half of August and of the 6 cm rate for February, we assign 2.5 cm to the first half of February. Then, in view of equations (18) and (19) we have

1/2 August	10.5 cm	
September	19 cm	
October	17 cm	
November	13.5 cm	
1/2 February	2.5 cm	
	Total 62.5 cm	(31)

For the period as a whole we have, from equation (30), a total evaporation of 80 cm. Therefore, the combined amounts of evaporation for December and January should come to 17.5 cm. On the basis of graphical interpolation, we suggest to divide that quantity as follows:

$$\begin{array}{ll} E_{12} = 10 \text{ cm} \\ E_1 = 7.5 \text{ cm} \end{array} \quad (32)$$

3.5 Step No. 5: March, April and May

It follows from (29) that for the Dead Sea as a whole,

$$E' = 75 \text{ cm} \quad (33)$$

Remembering that E' refers to the period from mid-February to mid-August, we have, so far, the following estimates [see (15) and (18)]:

1/2 February	3.5 cm
June	14.5 cm
July	18.5 cm
1/2 August	9.5 cm
	Total 46.0 cm

leaving, in view of (33), a total amount of 29 cm to be divided up among March, April and May.

One should not attempt to partition the 29 cm amount by straightforward interpolation. It has been shown elsewhere (Neumann 1954) that evaporation from lakes in spring possesses a peculiar feature. Instead of the evaporation rate increasing, so to speak, monotonically from winter to summer, the initial increase early in spring is followed by a decline in the evaporation rate about the middle of spring or so, to be, in turn, succeeded by a renewed increase.

The spring minimum of evaporation appears to be a fact for the Dead Sea. All the available level data indicate that the Dead Sea is at its highest level about the end of April or early in May (see Ashbel 1951, p. 181 and diagram on p. 168; Hydrological Service 1950, p. 230; Figure 2 in the present paper). Since the inflow of the surface waters reaches its maximum in February (see data for the Jordan in Table III) and this maximum is followed by a rapid drop in surface inflow, it is hard to explain the high water in spring by a factor other than a relatively low rate of evaporation and, perhaps, by a high rate of underground water inflow. However, the results of the present paper do not support conjectures as to the existence of an underground inflow in significant amounts (see below), an inference which is in agreement with recent work done by C.E. Jacob. We shall return to this point subsequently.

We shall tentatively partition the evaporation amount of 29 cm as follows:

March	8.5 cm	(35)
April	9.0 cm	
May	11.5 cm	

but emphasise the uncertainty of these figures.

3.6 Summary of results

Collecting results, including the estimates under (35), we arrive at Table VII and Figure 5.

TABLE VII
Monthly rates of evaporation from the Dead Sea

Month	Cm
January	7.5
February	6.0
March	8.5
April	9.0
May	11.5
June	14.5
July	18.5
August	20.0
September	19.0
October	17.0
November	13.5
December	10.0
Annual	155

4. TENTATIVE WATER BALANCE FOR THE DEAD SEA

The results of the foregoing section make it possible to set up a *tentative* water balance for the Dead Sea for an average yearly cycle, assuming no net change in the volume of water stored in the lake. The *highly tentative character* of the attempt undertaken in this section is emphasised.

In Table VIII, column B reproduces figures for monthly changes of lake level given in Table IV. It was pointed out earlier that these figures were obtained by preparing from all available level data a smoothed, idealised curve. In column A, we re-list the monthly rates of evaporation deduced in the present study as summarised in Table VII. In view of equation (16), the fundamental water-balance equation for a lake without an outlet, the sum of columns A and B represents the total inflow. In columns D, E, F and G, we partition column C into the following four "components": discharge of the Jordan at Allenby Bridge (see Figure 1), rainfall in the Dead Sea, dry weather flow + underground inflow, and, finally, storm-water inflow.

The figures in column D for the Jordan were prepared on the basis of discharge data for this river at Allenby Bridge, kindly made available by the Hydrological Service, Israel Ministry of Agriculture. We assume a yearly discharge of $1.25 \times 10^9 \text{ m}^3$, which for a lake area of 1020 km^2 (such as is fairly representative for the last decades) reduces, in round figures, to 122.5 cm. Since this figure might appear slightly

TABLE VIII
Tentative monthly water balances for the Dead Sea
(all terms in cm)

Month	A Evapora- tion	B Change of level	C Total inflow	D Jordan at Allenby Bridge	E Rain- fall	F Dry-weather surface inflow south of Allenby Bridge and under- ground inflow	G Storm-water inflow
January	7.5	+12.5	20	14.5	2.5	1.25	1.75
February	6	+16	22	16	1.5	1.25	3.25
March	8.5	+11	19.5	14	1	1.25	3.25
April	9	+ 3.5	12.5	10	0.5	1.25	0.75
May	11.5	- 0.5	11	9.25	—	1.25	0.5
June	14.5	- 5	9.5	8.25	—	1.25	—
July	18.5	- 9	9.5	8.25	—	1.25	—
August	20	-10.5	9.5	8.25	—	1.25	—
September	19	- 9.5	9.5	8.25	—	1.25	—
October	17	- 7.5	9.5	8.25	—	1.25	—
November	13.5	- 3.5	10	8.25	0.5	1.25	—
December	10	+ 2.5	12.5	9.25	1.5	1.25	0.5
Annual	155	0	155	122.5	7.5	15	10

high, it is well to point out that the Jordan's average yearly discharge in the years 1937/38 to 1943/44, during which the level of the Dead Sea remained stable, came very close to $1.25 \times 10^9 \text{ m}^3$. The precipitation estimates in column E are due to N. Rosenan.

The figures in column F are to represent dry-weather surface inflow (or base flow at the surface) *and* underground inflow. We assume that these terms are constant throughout the year. It will be remembered that the assumption of constancy of these terms enabled us to compute monthly evaporation rates for June, July, September and October and that in support of the assumption we introduced the data in Table III.

Figures in column G for storm-water inflow are, of course, the balance left over from total inflow after subtracting the terms for the Jordan, rainfall and dry weather surface flow plus underground inflow.

Summarising the table, we get, for a lake area of 1020 km^2 , the following annual water balance, in units of 10^6 m^3 :

Gains		Losses
Jordan at Allenby Bridge	1250	Evaporation 1580
Rainfall	80	
Dry-weather surface inflow south of Allenby Bridge and underground inflow to Dead Sea	150	
Storm-water inflow	100	
	<hr/> 1580	<hr/> 1580

It is worth adding a remark on the term representing dry-weather surface inflow and underground inflow.

The total surface inflow from the west scarp of the Dead Sea is estimated by Blake and Goldschmidt (1947, p. 399; see figures for the Ein Gedi and Ein Fashkha groups of springs) at ca. $75 \times 10^6 \text{ m}^3 \text{ yr}^{-1}$. Of this, about $60 \times 10^6 \text{ m}^3 \text{ yr}^{-1}$ constitutes dry-weather flow, according to an estimate given by M. Goldschmidt at a meeting in summer 1954 to which we will refer once more in Section 5. For the eastern coast of the lake, a map and a table by Ionides (1939, map preceding p. 147; and his table 21, p. 190) give a dry-weather flow ("ground water flow") of nearly $100 \times 10^6 \text{ m}^3 \text{ yr}^{-1}$. Thus, if we accept the foregoing two figures, we should have a total dry-weather *surface* flow of about $150 \times 10^6 \text{ m}^3 \text{ yr}^{-1}$, leaving very little for an underground inflow.

Assuming that Ionides' figures are high, underground inflow should hardly amount to more than $50 \times 10^6 \text{ m}^3 \text{ yr}^{-1}$. All these figures are, of course, uncertain to some extent, but the conclusion that underground inflow is relatively small seems to be inescapable.

5. RELATION OF PRESENT RESULTS TO RECENT RESULTS BY OTHER INVESTIGATORS

Ionides (1939, p. 143) states: "It is calculated that the depth evaporated from the surface (of the Dead Sea) annually is an amount approaching two metres." However, no details of the calculation are published. A similar evaporation rate is suggested by de Leeuw (1946). It is probably correct to say that Ionides, just as de Leeuw, was influenced by the assumed existence of a large underground inflow to the Dead Sea and if this assumption is relinquished, the estimates both by Ionides and de Leeuw would come close to the result reached in the present paper.

Ashbel (1951, p. 180) estimates that during recent years the total water supply to the Dead Sea amounted to between 1.25 and $1.40 \times 10^6 \text{ m}^3 \text{ yr}^{-1}$, or from 125 to 140 cm yr^{-1} . But since during the very same years, the level of the Dead Sea fell, it is clear that the evaporation rate must have exceeded the supply rate.

The results of the present study bear a close relationship to the results of recent work done by C.E. Jacob (Brigham Young University, Provo, Utah) and by M. Goldschmidt (Hydrological Service, Israel Ministry of Agriculture).

The work concerning the annual rates of evaporation from the northern and southern basins of the Dead Sea, as summarised in Section 2 above, was completed in spring 1954, and reported in June 1954 at a symposium of the Hydrology Section, Israel Society of Geodesy and Geophysics. About the same time, C.E. Jacob, in his capacity as consultant to Water Planning for Israel Ltd., began his work on the Dead Sea. Jacob undertook a study of fluctuations in meteorological (air temperature, Piche evaporation, rainfall) and hydrometric (Jordan discharge and lake-level data) variables. His results, which became available in summer 1954, and which included evaporation figures for bi-monthly periods, indicated an evaporation rate of 170 cm yr^{-1} .

Stimulated, in part, by conversations with C.E. Jacob, the present writer extended his study to monthly periods. That phase of the study, which is summarised in Section 3 above, was completed in August 1954.

In the course of discussions, Jacob agreed that his figures for the spring months should be reduced slightly in order to allow for the phenomenon of "spring minimum of evaporation" referred to earlier in Sub-section 3.5. This correction is desirable, as the phenomenon of low evaporation rates from lakes in the spring is not reflected in air temperature and Piche evaporation data on which his study is based. Jacob's corrected result amounts to ca. 160 cm yr^{-1} .

The result of Jacob's work as well as the monthly evaporation rates derived by the present writer were reported by Jacob at a meeting held in the offices of Water Planning for Israel Ltd. at Hakiryia in August 1954. At the same meeting, M. Goldschmidt presented his estimates based on hydrometric data and estimates for the

ungauged surface inflow. Assuming no underground inflow, he arrives at an evaporation rate of 153 cm yr⁻¹.

Thus the results of Jacob, Goldschmidt and the present writer, developed along different lines of approach, are close. It would appear that the average evaporation rate is between 150 and 170 cm yr⁻¹. It is quite possible that the rate lies in the narrower range of 155 to 160 or 155 to 165 cm yr⁻¹.

ACKNOWLEDGEMENTS

The writer is indebted to the following for stimulating conversations, for data and for information on specific points: D. H. K. Amiran, Department of Geography, The Hebrew University of Jerusalem; R. M. Bloch, Research Laboratory, Dead Sea Works Ltd; M. J. Goldschmidt, Hydrological Service, Ministry of Agriculture; C. E. Jacob, Brigham Young University, Provo, Utah, Consultant, Water Planning for Israel Ltd.; N. Rosenan, Meteorological Service, Ministry of Transport and Communications; and F. Yaron, Research Council of Israel.

This study could hardly have materialised without the series of meteorological and limnological observations initiated and conducted by D. Ashbel, Department of Meteorology and Climatology, The Hebrew University, and the hydrographic data due to A. de Leeuw, Water Planning for Israel Ltd. Also, the private file of data collected by N. Rosenan was invaluable, as was the file of data collected over many years by the senior staff of the Meteorological Service.

Finally, an expression of appreciation is due to G. E. Hutchinson, Osborn Zoological Laboratory, Yale University, New Haven, Conn., and to A. H. Woodcock, Woods Hole Oceanographic Institution, Woods Hole, Mass., for data made available in advance of publication.

REFERENCES

1. ANDERSON, E. R., 1952, Energy budget studies, *Water-loss investigations, Lake Hefner Studies, Technical Report*, Vol. I, 71-119, Geological Survey, Washington, 151 pp.
2. ARONS, A. B. AND KIENZLER, C. F., 1954, Vapor pressure of sea salt solutions, *Trans. Am. geophys. Un.*, **35**, 722-726.
3. ASHBEL, D., 1944, *Fifteen Years' Observations on the Climatology and Hydrography of the Dead Sea*, The Hebrew University of Jerusalem, xiv + 114 pp.
4. ASHBEL, D., 1945, Temperature conditions of the sweet-water lakes in Palestine (in Hebrew), *Hateva*, **2**, 72-79.
5. ASHBEL, D., 1950, *Bio-climatic Atlas of Israel*, Department of Meteorology, The Hebrew University of Jerusalem, 151 pp.
6. ASHBEL, D., 1951, *Regional Climatology of Israel* (in Hebrew), Department of Meteorology, The Hebrew University of Jerusalem, 244 pp. Incorporating as supplement: *Meteorological Normals of Israel*, 17 pp.
7. BLAKE, G. S., 1930, *The Mineral Resources of Palestine and Transjordan*, Jerusalem, 41 pp.
8. BLAKE, G. S. AND Goldschmidt, M. J., 1947, *Geology and Water Resources of Palestine*, Government Printer, Jerusalem, 413 pp.
9. BOLZ, H. M., 1949, Die Abhängigkeit der infraroten Gegenstrahlung von der Bewölkung, *Ztsch. Meteor.*, **3**, 201-204.

10. BOWDEN, K. F., 1948, The processes of heating and cooling in a section of the Irish Sea, *M. N. roy. astr. Soc., Geophys. Suppl.*, **5**, 270–281.
11. BOWEN, I. S., 1926, The ratio of heat losses by conduction and by evaporation from any water surface, *Phys. Rev., Ser. 2*, **27**, 779–787.
12. BRASLAVSKY, Y., 1950, *Around the Dead Sea, Hayada'ta et Ha'aretz* (in Hebrew), Vol. 3, Hakibutz Hameuhad, Tel Aviv, 476 pp.
13. DE LEEUW, A., 1946, Some data concerning the Dead Sea, *J. Assn. Eng. Arch. Pal.*, **7**, 23–25.
14. FRITZ, S., 1949, The albedo of the planet earth and clouds, *J. Meteor.*, **6**, 277–282.
15. GLASSTONE, S., 1951, *Textbook of Physical Chemistry* (2nd ed.), Macmillan, London, 1320 pp.
16. GOLDSTEIN, S. (ed.), 1938, *Modern Developments in Fluid Dynamics*, Vol. 2, Clarendon Press, Oxford, 702 pp.
17. HARBECK, G. E., JR., 1955, *The effect of salinity on evaporation (Professional Paper 272-A)*, U. S. Geol. Survey, Washington, 6 pp.
18. HOUGHTON, H. G., 1954, On the annual heat balance of the northern hemisphere, *J. Meteor.*, **11**, 1–9.
19. IONIDES, M. G., 1939, *Report on the Water Resources of Transjordan and their Development*, Crown Agents for the Colonies, London, 372 pp.
20. Israel Hydrological Service, 1950, *Hydrological Year-book of Israel, 1946/47*, Government Printer, Jerusalem, xxxii + 288 pp.
21. NEUMANN, J., 1953a, Energy balance of and evaporation from sweet-water lakes of the Jordan rift, *Bull. Res. Council of Israel*, **2**, 337–357.
22. NEUMANN, J., 1953b, On a relation between the annual heat budgets of seas and lakes and other terms of the energy equation, *Quart. J. roy. meteor. Soc.*, **79**, 532–534.
23. NEUMANN, J., 1954a, On the annual variation of evaporation from lakes in the middle latitudes, *Arch. Meteor. Geophys. Biokl., Ser. B*, **5**, 297–306. (See also, *Proc. Internat. Assn. theor. appl. Limn.*, **12**, 106–110, 1955).
24. NEUMANN, J., 1954b, Insolation in relation to cloud amount, *Mo. Wea. Rev.*, **82**, 317–319.

LETTER TO THE EDITOR

A note on the revision of the stratigraphy of the Southern Carmel. E. KASHAI, *Department of Geology, The Hebrew University of Jerusalem.*

Since the publication of our paper "On the Lithostratigraphy and tectonics of the Carmel"¹, paleontological investigations have led us to certain stratigraphic revisions discussed briefly in this note and illustrated in the attached geological map and section (Figures 1 and 2).

1. The reef limestone and dolomite beds between the volcanic tuffs appearing on the western flank of Wadi Natif east of Umm es Zeinat are covered with chalk referred formerly to the Daliya series. The fossils of this chalk determined now, however, indicate an age identical with the Upper Cenomanian, so-called Juneidiye, series.

2. The thin marls around Umm es Zeinat are now considered stratigraphically equal to the thicker Turonian Daliya marl. They are no longer referred to the Zikhron Zone. Therefore, the layers underneath the Daliya marls belong to the Muhraqa series considered to be the base of the Turonian. The Qumbaze limestone remains the top of the Turonian. Both Turonian horizons, Daliya marl and Muhraqa limestone, are thinning out towards the south so that Daliya marl disappears completely towards Ijzim. Muhraqa limestone series is represented from Ijzim to Shune by the reef limestone of the lower Shune series.

3. Therefore the formations underlying the Shune series, as found in most of the Lower and Western Carmel up to Wadi Mughrara, are of Cenomanian age and are stratigraphically identical with the Main Chalk complex developed principally in the Upper Carmel. Many difficulties arose in the comparison of these formations because of the abundant reef facies occurring in the Lower Carmel, contrasting with the rather uniform chalky lithology of the Upper Carmel.

4. These stratigraphic changes naturally lead us also to an age revision of the various volcanic intercalations as expressed in the following table.

2 km north of Bat Shlomo	Senonian
Around Shefeya	Shuna series
Around Ofer	Shuna series
South of Ein Ghazal	Shuna series
1 km south of Ijzim	Shuna series
Around the valley of Maqura	Juneidiye series
The valley east of Ijzim	Juneidiye series
East of Zikhron Ya'akov	Juneidiye series
Umm et Tos (1 km NE of Fureidis)	Juneidiye series
North of Ein Ghazal	Juneidiye series
Along the road E of Ijzim	Juneidiye series
W and E of Muhraqa	Khureibe-Juneidiye series
1 km south of Ein Ghazal	Khureibe series
The valley W of Ijzim	Khureibe series
The valley E of Umm ez Zinat	Khureibe series
Wadi Zarra'a (1 km S of Damun)	Isfiya series

REFERENCE

1. PICARD, L. AND KASHAI, E., 1958, *Bull. Res. Council of Israel*, 7G, 1.

Received August 26, 1958.

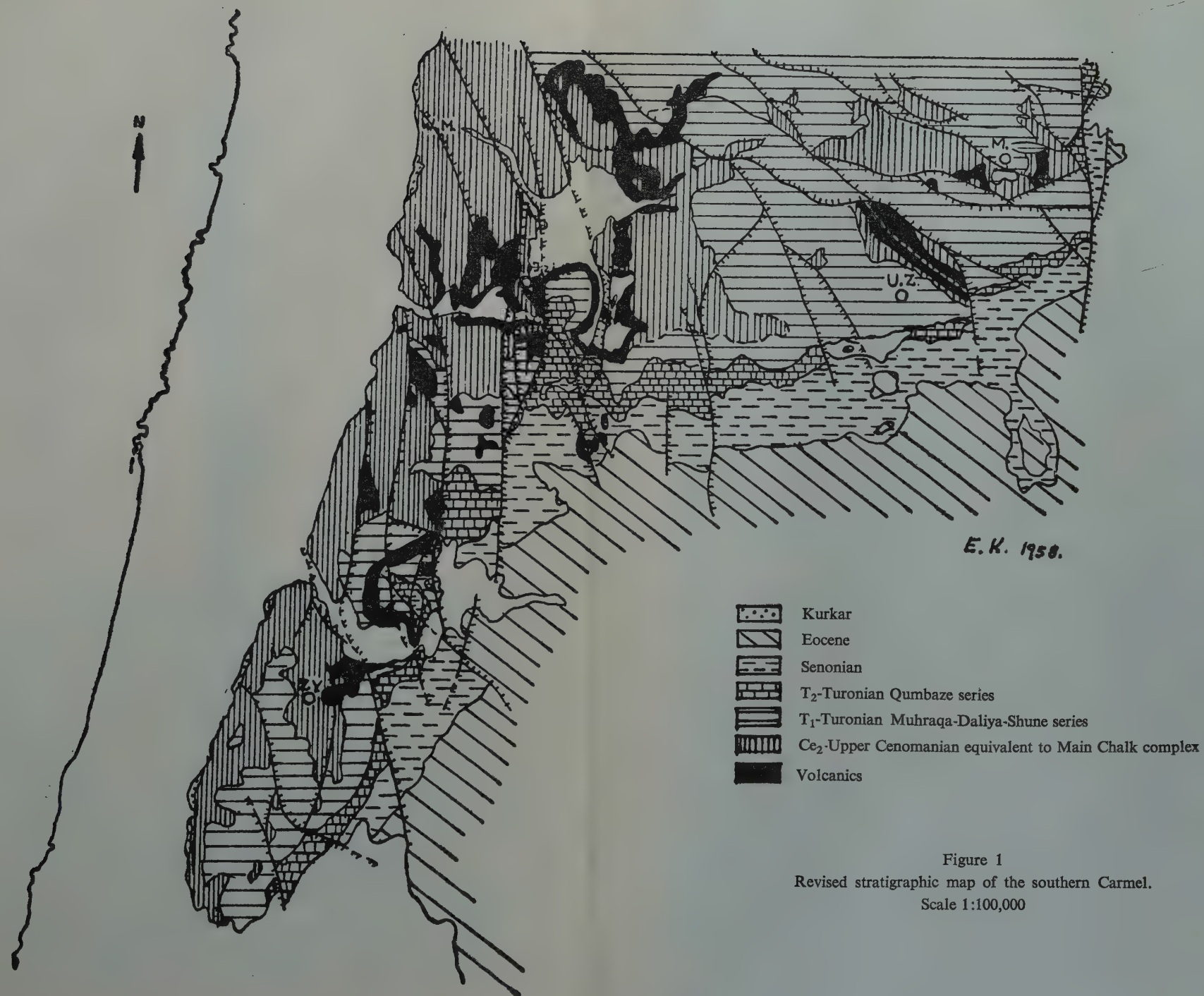


Figure 1
 Revised stratigraphic map of the southern Carmel.
 Scale 1:100,000

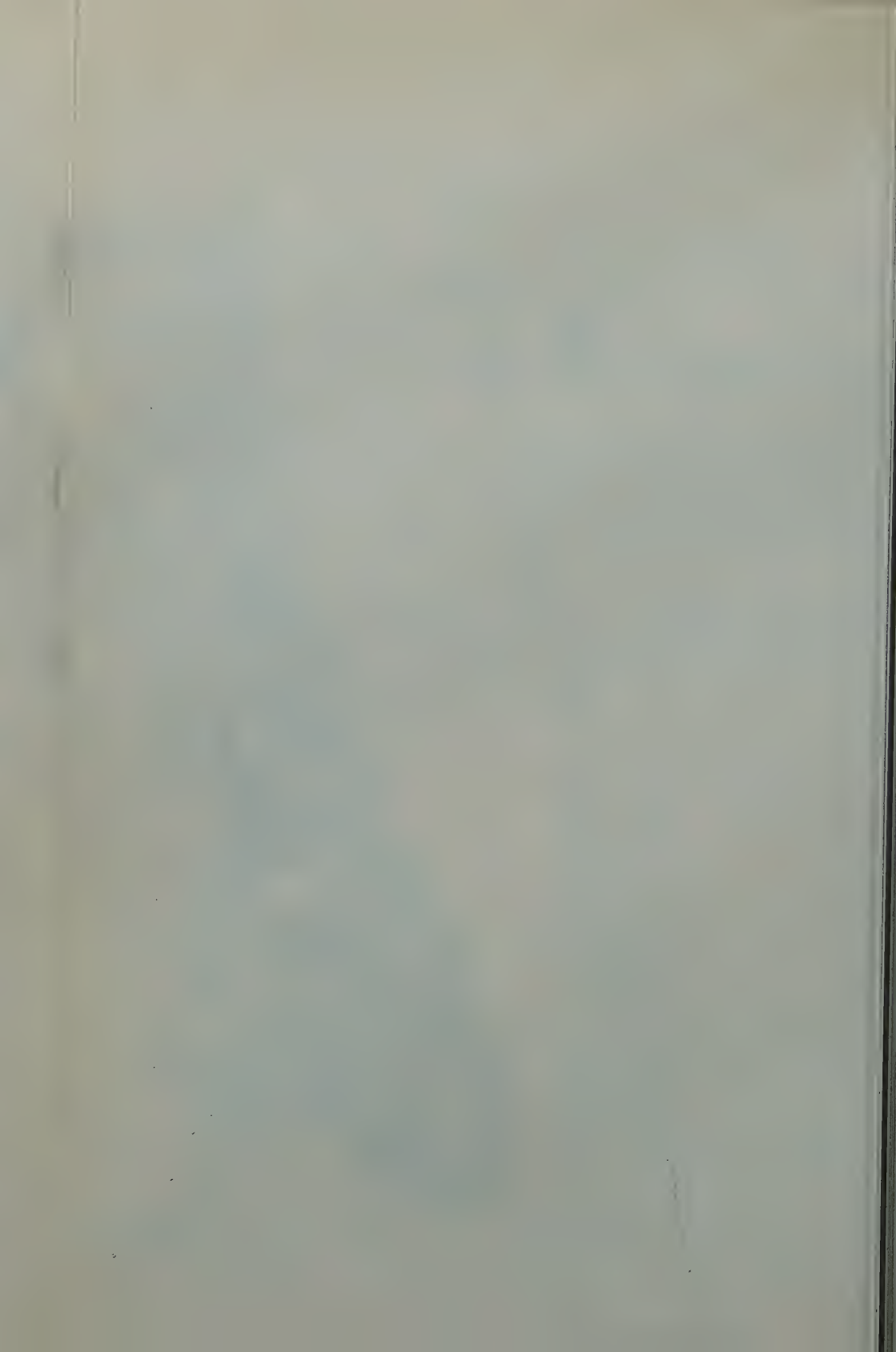
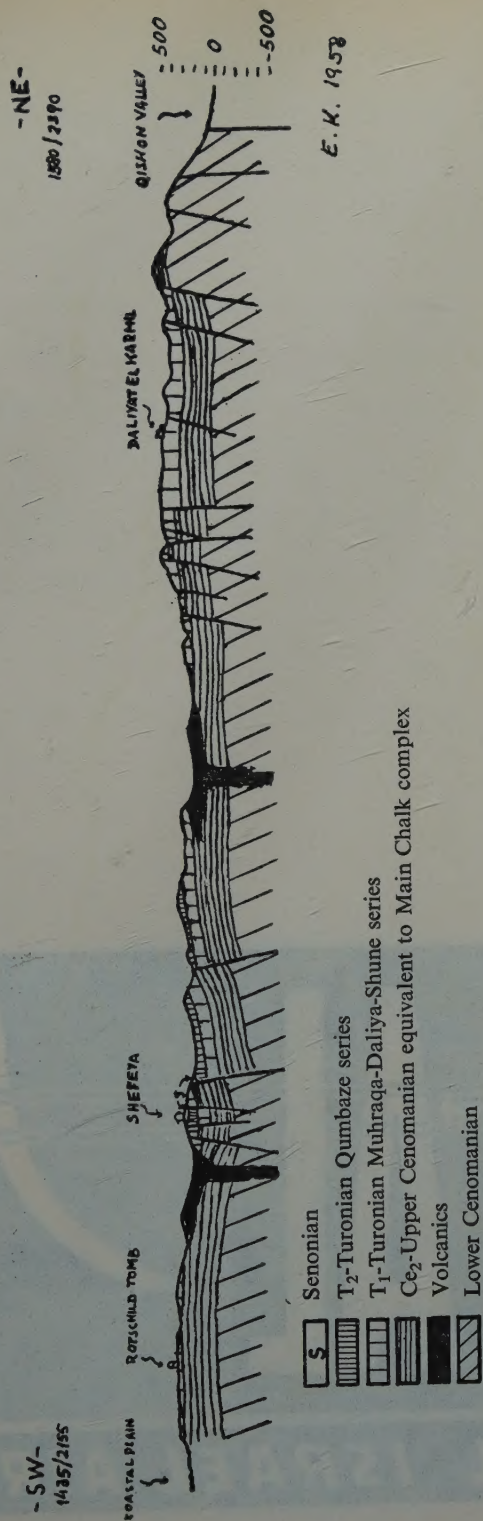
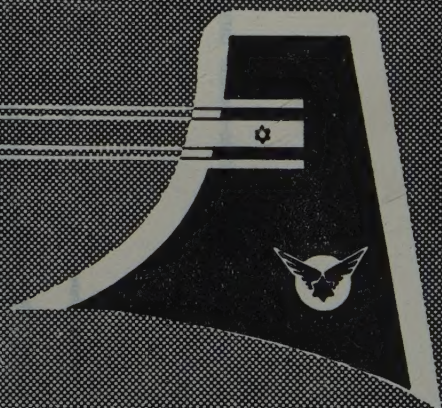


Figure 2
Revised cross-section through the Carmel. Horizontal scale 1:100,000, vertical scale 1:50,000



ELAL



EL AL ISRAEL AIRLINES

ISRAEL FOR YOUR NEXT CONVENTION

A pleasant, sunny climate all year round



For further information, please contact :
ISRAEL GOVERNMENT TOURIST CORPORATION,
JERUSALEM

or

ISRAEL GOVERNMENT TOURIST INFORMATION OFFICES
New York, London, Paris, Rome and Zurich.

ABC BOOKSTORE

SPECIALIST IN SCIENTIFIC AND TECHNICAL BOOKS

Orders from all countries accepted
Israel Distributor for The Weizmann Science Press Jerusalem

TEL-AVIV, 71 ALLENBY ROAD • PHONE 64058

יוצא לאור ע"י

מוסד ויצמן לפרסומים במדעי הטבע ובטכנולוגיה בישראל
המועצה המדעית לישראל - משרד החינוך והתרבות - האוניברסיטה העברית בירושלים
הטכניון - מכון טכנולוגי לישראל - מכון ויצמן למדע - מוסד ביאליק

Published by

THE WEIZMANN SCIENCE PRESS OF ISRAEL
Research Council of Israel, Ministry of Education and Culture
The Hebrew University of Jerusalem, Technion-Israel Institute of Technology
The Weizmann Institute of Science, Bialik Institute

Printed in Israel

Raphael Haim Hacohen Press, Ltd., Jerusalem

WSP/1000/12.58